TOPOLOGY DEPENDENT ENERGY

STORAGE MECHANISMS

by

Connor James Welty

A dissertation submitted in partial fulfillment
of the requirements for the degree

of

Doctor of Philosophy

in

Chemistry

MONTANA STATE UNIVERSITY
Bozeman, Montana

July 2024

ACKNOWLEDGEMENTS

First and foremost, I would like to thank my advisor Nick Stadie for the unwavering support in pursuing my PhD. Your dedication and relentless pursuit towards high quality science has given me an exceptional perspective on how to go about solving problems. Thank you for taking a chance on me as a naïve first year student and encouraging me to work on projects that felt impossibly complex at the time.

I would like to thank my committee, Dr. Erik Grumstrup, Dr. Rob Walker, and Dr. Patrick Callis for your willingness to support me on this path. The courses that I took from you and the conversations we have had expanded my understanding of chemistry.

Thank you to Wei Xu who taught me everything I know about battery fabrication and the attention to detail required to succeed. Your work ethic and jovial energy had a huge impact on the atmosphere of the lab.

Thank you to my family for the sacrifices that you have made to provide me with endless opportunities. You have taught me to be curious, to ask more questions, and to pursue what makes me happy.

TABLE OF CONTENTS

TABLE OF CONTENTS CONTINUED

TABLE OF CONTENTS CONTINUED

TABLE OF CONTENTS CONTINUED

LIST OF TABLES

Table Page

Chapter Three

Chapter Three Supplementary Information

Chapter Four Supplementary Information

LIST OF TABLES CONTINUED

Table Page

LIST OF FIGURES

Figure Page

Chapter One

Chapter Two

LIST OF FIGURES CONTINUED

Figure Page

Chapter Three

LIST OF FIGURES CONTINUED

Figure Page

Chapter Three Supporting Information

LIST OF FIGURES CONTINUED

Figure Page

Chapter Four

LIST OF FIGURES CONTINUED

Figure Page

Chapter Four Supplementary Information

Chapter Five

LIST OF FIGURES CONTINUED

Figure Page

LIST OF FIGURES CONTINUED

Figure Page

GLOSSARY

CV	Cyclic voltammetry
DIB	Dual-ion battery
DIHC	Dual-ion hybrid capacitor
DMC	Dimethyl carbonate
EC	Ethylene carbonate
EDLC	Electric double layer capacitor
EIS	Electrochemical impedance spectroscopy
EPR	Electron paramagnetic resonance
ET	Electron transfer
GCD	Galvanostatic charge-discharge
HT	Hole transfer
KIB	Potassium-ion battery
LIB	Lithium-ion battery
MOF	Metal-organic framework
NIB	Sodium-ion battery
NMR	Nuclear magnetic resonance
PC	Propylene carbonate
SEI	Solid electrolyte interphase
XPS	X-ray photoelectron spectroscopy
XRD	X-ray diffraction
ZTC	Zeolite-templated carbon

ABSTRACT

Electrically and ionically conducting porous frameworks present an alternative to the kinetically hindered active materials currently used in electrochemical energy storage systems. The materials used in electrodes greatly influence the energy density, rate capability, and environmental footprint of batteries. Low cost and green materials are needed to electrify grid storage and fast charging materials are needed to electrify vehicles. Materials with high porosity and conductivity are rare but ideal for the storage of more abundant metals than lithium, such as sodium and potassium. When porosity and conductivity coexist, electrons and ions can diffuse through the material with the efficiency necessary for electrochemical storage. However, converting chemical energy to electrical energy is a complicated process and it is difficult to characterize directly. It largely takes place at the interface between the solid electrode and liquid electrolyte which is inherently variable. This interaction can be simplified and understood by employing highly ordered materials. In this work, novel materials including zeolite-templated carbons (ZTCs) and metal-organic frameworks (MOFs) were synthesized and characterized to elucidate their topologies and compositions. Compositionally similar MOFs with different topologies (crystalline arrangements of their building blocks) showed the role of pore dimensionality on conductive pathways. ZTCs were fabricated into anodes and cathodes and electrochemically cycled with methodologically varied electrolytes. In one study, the framework was held constant and the ion properties (size, shape, oxidative stability, and desolvation kinetics) were changed. In the next study, the topology of layered 2D and cubic 3D ZTCs were compared. These studies show that ion composition matters more than size or shape and that layered materials are poor ionic conductors but superior electron conductors. The materials used in these studies provide insight into the nature of ionic and electronic pathways that electrochemical energy storage systems depend on.

CHAPTER ONE

INTRODUCTION

Overview

This dissertation presents a methodological and systematic approach toward understanding ionic and electronic transport mechanisms within 2D and 3D structured materials. The motivation for this research is application-based, the properties of these materials are highly relevant for energy storage in battery and battery-like systems. Specifically, model materials that support more sustainable storage chemistries than the state-of-the-art Li-ion "rocking chair" battery were investigated. The rapid development of renewable energy generation (wind, solar, etc.) has exceeded our ability to store said energy. Low cost, abundant, environmentally friendly materials will enable full utilization of this harvested energy. The solutions currently being researched are widespread, ranging from electrolyzers and hydrogen storage to solid-state batteries, but the underlying research almost always circles back to the interaction of molecules at an interface. While the end goal of these studies is to inform research for next generation battery systems, fundamental curiosity about the movement of ions and electrons through channeled, layered, and three-dimensionally porous structures also propels research. The current understanding of the molecular level mechanisms at play in electrochemical cells remains relatively abstract because of the limitations of in-situ techniques and computational processing power. By choosing structurally ordered materials and a suite of electrochemical techniques, on the other hand, we can begin to paint a picture of what's going on under the hood of a battery. Beginning with a summary of the main objectives, in the subsequent chapters we present 3

unique investigations into ionic and electronic movement within 2D- and 3D-connected porous carbon materials and metal-organic frameworks (MOFs).

Chapter 2 begins with detailed methods that were not included in the following manuscripts. There were many techniques that required the development of intuition through repeated practice. Those techniques are described as accurately as possible in the hopes that they can be replicated.

Chapter 3 introduces a methodological study of anion insertion into a 3D-connected, cubic zeolite-templated carbon (ZTC) toward applications in dual-ion hybrid capacitors (DIHCs). DIHCs are a promising alternative to the commercially adopted Li-ion shuttle battery because of their fast kinetics that allow for rapid charging. When templated from the cubic **FAU** zeolite, a microporous, conductive, cubic-ordered porous carbon framework with an ultrahigh surface area known as **FAU**-ZTC (also referred to as 3D ZTC) is left behind. We propose **FAU**-ZTC as a model material for ion storage because it has highly ordered, three-dimensionally connected pores and no layered or stacking structure. Graphite, hard carbon, and activated carbon are standard materials for battery and capacitor electrodes but their charge storage character makes it difficult to unravel the effect of ion size, diffusion, and solvation effects from the variety of ion storage mechanisms intrinsic to those materials.[1] ZTC exhibits exclusively a classic electric double layer charge storage mechanism which allows us to remove extra variables and focus on how the anions interact with each other, the solvent, and the surface of the material.

Chapter 4 digresses slightly into the inorganic synthesis of metal-organic frameworks (MOFs) to gain insight into the unique electron transport between organic and inorganic substituents. Fundamental interest in the conductivity mechanisms of MOFs has inspired their

development as active materials in electrocatalysts[2], supercapacitors[3], and batteries[4]. Historically, porous MOFs have been electrically insulating because of the poor electronic overlap between the metal clusters and organic ligands, resulting in highly localized electronic bands.[5] In order to reveal the dependency of conductivity on dimensionality of the metal cluster-linker bonding, we synthesized a novel 2D yttrium-based MOF (YHOTP) for comparison to a known 3D analogue (Y_6HOTP_2). YHOTP is a hexagonal MOF with stacked layers of the triphenylene HHTP (also called HOTP when oxidized) linker that are bridged by metal centers in between the linker layers. Y_6HOTP_2 is a cubic MOF that crystallizes in 3 dimensions because of the high temperature and molar ratio of Y to HHTP used in the synthesis. The electrical conductivities of these materials are explored experimentally using a 2-point probe device and reconciled according to their computationally-derived band structures. The electronic conductivity pathways are significantly different because of the shift in dimensionality, even though the primary constituents of the MOFs are the same.

Chapter 5 returns back to ZTC as an electrode material but with a topology adjustment to accommodate next generation ion storage (with a focus on Na^+ and K^+). In this study, we compare 2D and 3D topologies again but instead of focusing on electronic conductivities (which in this case are similar in the two materials) we seek to elucidate the ionic conductivity mechanisms. As the demand for sustainable energy storage systems grows, so does the need for abundant, environmentally benign, and rate capable devices.[6] The search for ions beyond Li^+ such as Na^+, K^+, Mg^{2+}, and Ca^{2+} has intensified and therefore more accommodating materials are also needed. We compare the state-of-the-art materials for Li^+, Na^+, and K^+ ion storage (graphite

and hard carbon) with 2D and 3D ZTCs to reveal mechanistic signatures across the entire spectrum from intercalation/faradaic to capacitive charge storage mechanisms.

Chapter 6 summarizes these 3 studies into one body of work drawing ties between the motivations of each unique hypothesis. We suggest where this work could be further developed and how it can be used to guide the design of next-generation energy storage materials.

Objectives

Our objectives of this work are:

1. To methodologically explore anions of different size and shape, to show how these properties influence the capacity and electrochemical signature of anion storage in 3D ZTC.
2. To elucidate the electronic conductivity pathways in 2 structurally unique but compositionally similar MOFs, and
3. To show how topology of the host framework (2D layered vs. 3D open scaffold) affects ion transport in 3 different battery systems.

These objectives are addressed by synthesizing frameworks with varying topology and composition from the ground up and performing extensive electrochemical characterization on them. The intention was to design materials for applications in energy storage systems but the fundamental curiosity to map out the mechanisms of ionic and electronic pathways drove the research. Tens of variables were considered in the synthesis processes and hundreds of electrochemical cells were fabricated to guide us through the many doors that these hypotheses opened. X-ray diffraction (XRD) is the primary characterization technique for the materials we synthesized because it reveals the underlying crystal structure, unit cell size, and crystallite size

as well as being used as a quality control. Nuclear magnetic resonance (NMR) spectroscopy, specifically pulsed field gradient spin echo (PFGSE) NMR spectroscopy, helped us characterize the electrolytes by probing the various constituents' diffusion coefficient and ionic conductivity properties. 2-point probe conductivity measurements were imperative for predicting how electron transport might limit performance when incorporated into a battery. Extensive engineering is necessary for electrode fabrication, from tuning binder and conductive additive ratios to varying thicknesses, to mixing and drying techniques. Electrochemical characterization consists of galvanostatic charge discharge (GCD), cyclic voltammetry (CV), and electrochemical impedance spectroscopy (EIS) which provided us with a vast amount of data that were used to derive trends and properties. Finally, these data were treated by conversion into energy and power density (i.e., to produce a Ragone plot) which compares the materials we synthesized to other state-of-the-art and emerging energy storage materials. The information gleaned from all of these characterization techniques provides the scientific community with a unique assessment of energy storage systems through a lens of porous materials topological structure.

Perspective

Climate Crisis

There are a variety of ways to generate energy, from nuclear to hydro to thermal to solar and wind. This diversity provides ample opportunity to solve the current climate crisis without being dependent on one solution, but rather a portfolio of solutions. However, the inability to store the energy that is generated creates issues when the sources are either not producing or have been overwhelmed. Batteries, hydrogen fuel cells, and pumped hydro are all viable and relatively clean options for storing the energy that is renewably generated. As of 2023, the world

depended on fossil fuels for ~80% of its energy, with 32%, 27%, and 24% coming from oil, coal, and natural gas, respectively.[7] The reliance on a singular source for the majority of the world's energy consumption has caused 4 major overuse issues: emissions, land degradation, water pollution and diminishing resources. Emissions from the burning of fossil fuels mostly consist of carbon dioxide but also methane, nitrous oxide, and sulfur dioxide, all of which contribute to trapping heat in the atmosphere and increasing the global temperature. Land degradation stems from the extraction of fossil fuels but also from the facilities used for processing and waste disposal. Waterways are polluted from the toxic runoff that leaks from the mining and transportation of fossil fuels. Dependence on the extraction and burning of fossil fuels for energy in almost every sector of the economy has pushed us into an environmental disaster that can only be explained by anthropogenic activity. By broadening the myriad of energy resources that the agriculture, transportation, residential and commercial sectors rely on, we can prevent abuse of a singular resource that results in over concentration of emissions. One overarching solution will not work for every sector but electrochemical energy storage consists of many different chemistries that can be tailored toward a given application. Li-ion batteries provide a relatively green solution to the transportation sector's impact, which accounts for 29% of the greenhouse gas emissions in the US.[8]

From Gasoline to Electric

A direct comparison between the performance and environmental footprint of internal combustion engine vehicles and electric vehicles (EVs) is necessary in order to justify the application of electrochemical energy storage for transportation. Currently, lithium ion batteries (LIB) are the state of the art battery type because of their high energy density (e.g., 280 Wh kg^{-1})

and reusability (e.g., 6,000 charge/discharge cycles), but there are disadvantages that must be addressed before full adoption.[9] Gasoline has a gravimetric energy density, almost 50 times greater than LIBs at 12,200 Wh kg^{-1} which means the driving range of EVs is severely limited and only partially recouped by an efficiency that is 5 times higher than gas vehicles.[10] The environmental footprint of EVs can be broken up into three categories; production of the vehicle/battery, greenhouse gasses emitted while driving, and the impact of battery disposal at end of life (see Figure 1).

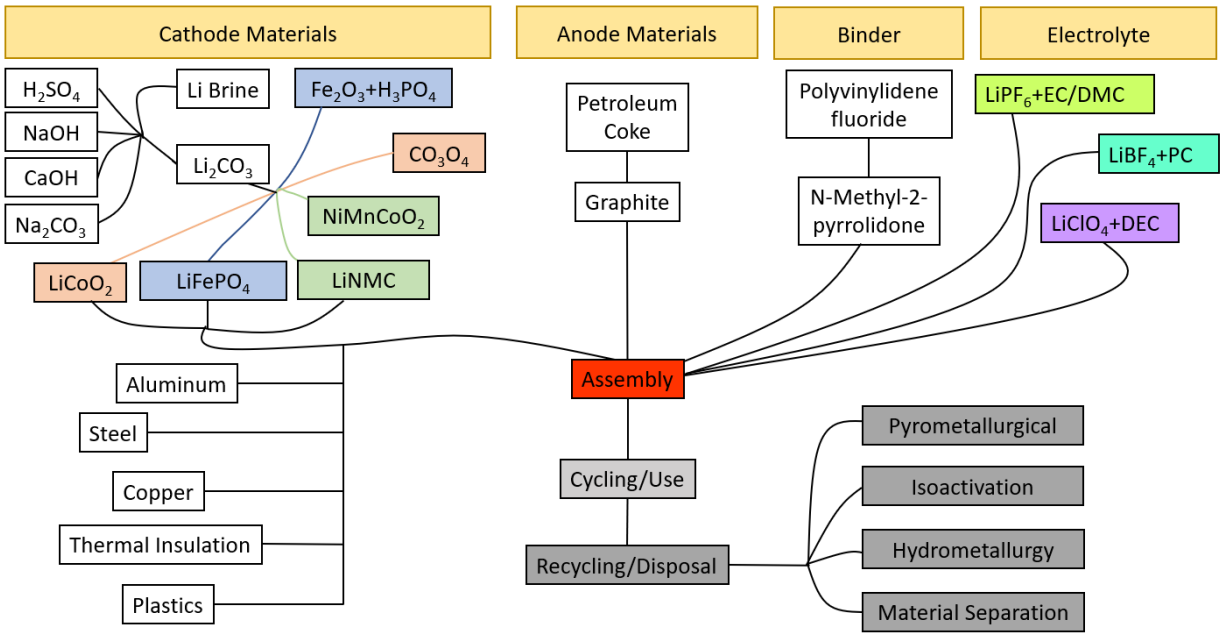

Figure 1. Steps in materials production for LIBs.

Building an 80 kWh LIB (the size needed for 300 miles range) can emit up to 16 metric tons of CO_2, about 80% more than building a gas vehicle.[11] EVs produce zero direct emissions when being driven, but the emissions attributed to charging the battery can vary greatly depending on the source. Gas vehicles emit 347 g of CO_2 per mile while being driven, which is

where the majority of their pollution originates.[12] The large majority of LIBs from EVs are not recycled because it is not economically viable and are therefore thrown into a landfill where 5% of the metals can leach into the soil and water.[13] In comparison, 99% of lead acid batteries are recycled in the US and 80% of new lead acid batteries are made from recycled materials.[14] In a cradle to grave assessment, which includes all three of the factors mentioned above, internal combustion engine vehicles emit 382 grams of CO_2 per mile and full electric vehicles with a range of 400 miles emit 209 g of CO_2 per mile.[15] In conclusion, gas vehicles emit almost 50% more greenhouse gasses than EVs, and as the energy density of LIBS is enhanced and the electric grid is decarbonized, this gap will only widen. There are other environmental impacts that were not mentioned that arise from the extraction of metals for LIBs such as water consumption and soil contamination. Future chemistries such as Na-ion batteries (NIBs) aim to address these by relying on more accessible and abundant metals.

Lithium and Post-Lithium

Fundamentals

Lithium-ion batteries were introduced to the commercial world in 1990 by Sony to meet the handheld electronics demand, but the concept was developed over the previous several decades by scientists including Stanley Whittingham, John Goodenough, and Akira Yoshino.[16-18] The use of $LiCoO_2$ as a cathode material was discovered by Goodenough in 1979 and the first successful electrochemical intercalation of lithium into graphite was demonstrated by Yazami and Touzain in 1982.[19] LIB chemistry has evolved greatly in the last 45 years but the basic principles of operation remain the same, namely by shuttling Li-ions from a lithium rich cathode into a carbonaceous anode upon charging and back into the cathode upon discharge. Currently

there are thousands of papers being published each year on new materials, salts, solvents, separators, and cell casings to make the LIB greener, more efficient, more stable, and safer. Every component has room for improvement but a large amount of research is being conducted on the materials used for the electrodes. There are multiple different cell configurations based on the desired device application but the majority of fundamental research uses 2032 coin cells (see Figure 2) to run electrochemical tests from which energy and power density can be estimated for real world applications.

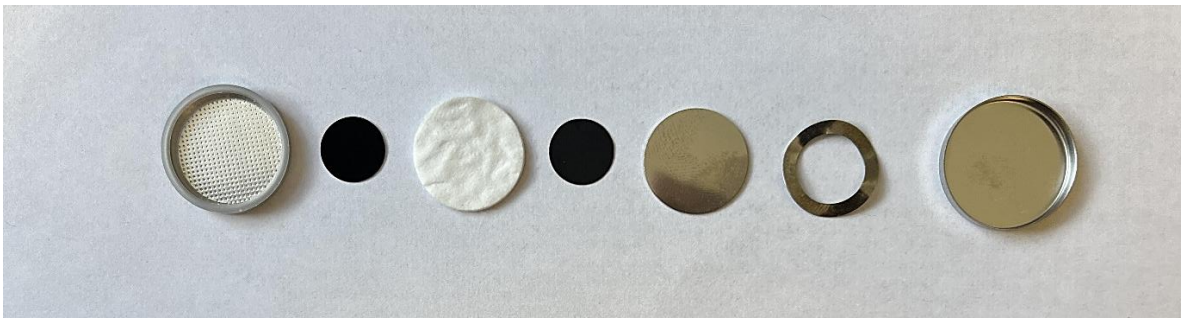

Figure 2. LIB coin cell configuration, from left to right; negative cell case, anode on Cu foil, glass fiber separator, cathode on Al foil, spacer, spring, positive cell case

The electrodes are crimped between two cases and partitioned by a glass fiber separator that allows ions through but not electrons, which forces them to go through an external circuit and generate electricity (see Figure 3).[20] The separator is soaked with electrolyte (a lithium salt dissolved in an organic solvent) to provide a medium in which the Li-ions can diffuse into from the cathode upon polarization of the cell. Figure 3 shows a view inside of a cell where upon charging, the cathode is oxidized and the electrons flow through the external circuit, simultaneously the Li^+ ions flow through the separator to intercalate into the graphite and meet the electrons. At the congregation of ions and electrons, the anode is reduced and changes symmetry to form a new phase, moving from a low to a high energy state. The balanced redox

reaction for a cell comprising graphite and $LiCoO_2$ is based on the following half-reactions (during charging):

$$\text{Anode (graphite):} \qquad 6C + Li^+ + e^- \rightarrow LiC_6 \qquad (1)$$

$$\text{Cathode } (LiCoO_2): \qquad LiCoO_2 \rightarrow CoO_2 + Li^+ + e^- \qquad (2)$$

The same reactions occur in reverse upon discharging. A spring and spacer are also added to compress the electrodes into each other and minimize the diffusion path length for the active ions. Using coin cells, while far from commercial scale, can protect against extraneous variables which might otherwise inhibit data comparisons between research groups. For chemists, this means engineering problems can be mitigated and the focus remains on the chemistry happening at the interface between the electrode active material and the electrolyte.

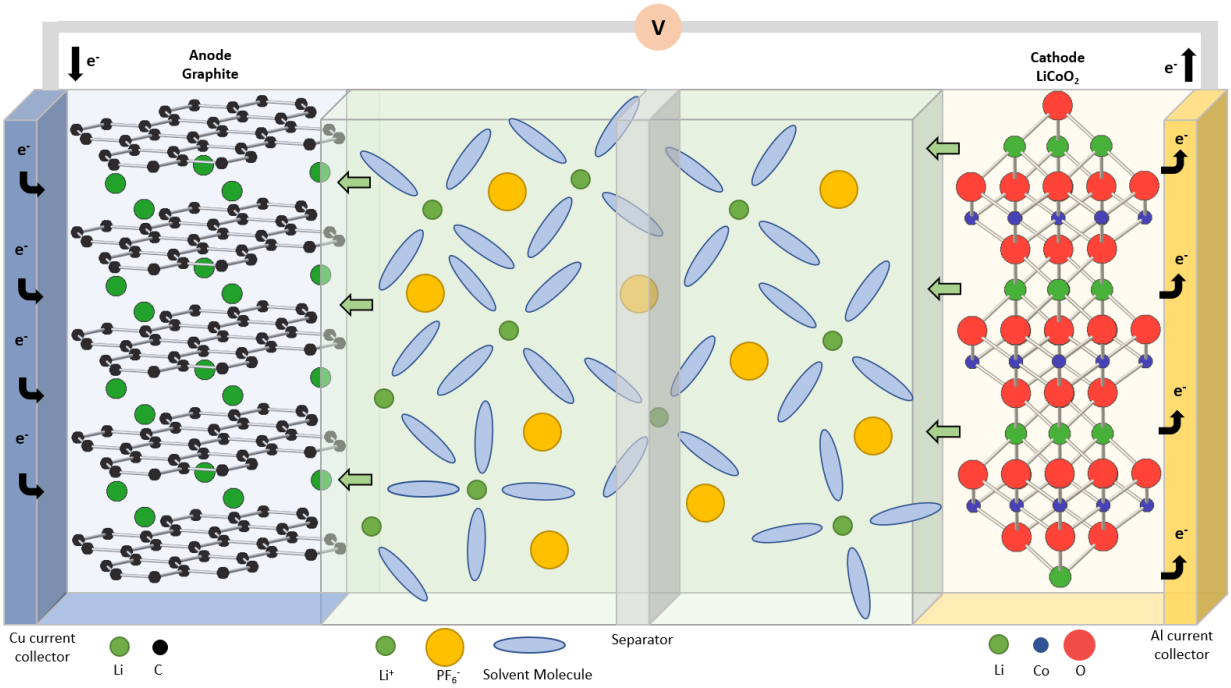

Figure 3. Schematic of the classic Li-ion battery during charge.

Generally, the cathode of a full cell is made up of a metal oxide (e.g., $LiCoO_2$ or $LiNi_{0.8}Mn_{0.1}Co_{0.1}O_2$) or phosphate (e.g., $LiFePO_4$) which have a high potential of lithiation while the anode contains graphite because it can safely and reversibly intercalate Li ions up to a high capacity of LiC_6 (see Figure 4).[21] Ideally, lithium metal would be used as the anode because it is the lightest metal and has one of the lowest reduction potentials (-3.04 V vs. the standard hydrogen electrode). However the electrochemical potential of Li/Li^+ lies above the lowest unoccupied molecular orbital (LUMO) of all known non-aqueous electrolytes which causes decomposition and therefore dendrite formation which is a major short circuit safety issue.[22] Touzain et al. found that lithium ions intercalate into graphite at potentials very close to that of lithium metal, maintaining a high energy density but eliminating the dendrite problem by forming a stable solid electrolyte interphase (SEI) at the surface.[23]

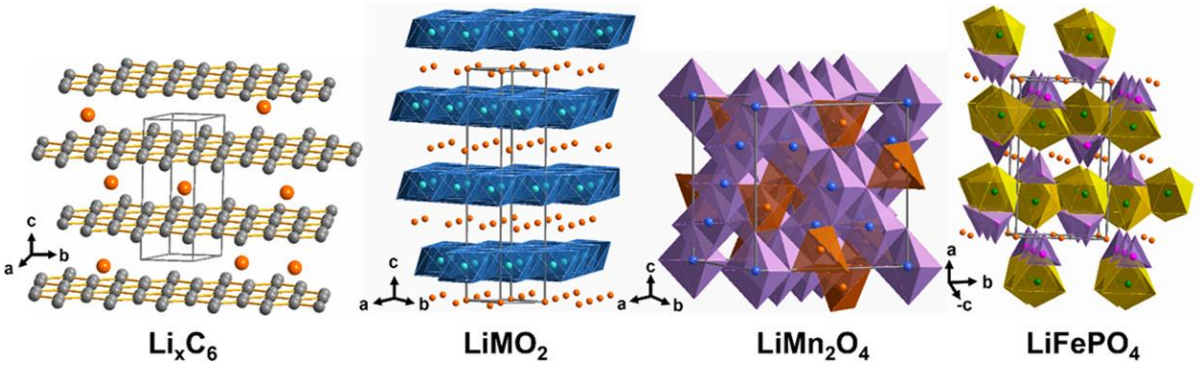

Figure 4. Crystal structures of graphite Li_xC_6, layered $LiMO_2$ (M = Mn, Co, and Ni), spinel $LiMn_2O_4$, and olivine $LiFePO_4$ (Adapted from reference 21)

In 1990, Jeff Dahn made a breakthrough by discovering that ethylene carbonate can facilitate the solvation and diffusion of Li^+ into graphite which supported a highly reversible process.[24] The impact of this invention will last for decades as society attempts to meet the ever-growing demand for electrified transportation and large-scale grid storage. The abundance of

characterization and electrochemical data produced from these original model materials has allowed chemists to probe for new materials that take small steps toward meeting key environmental expectations for electrochemical energy systems. Some of the most promising chemistries beyond LIBs include NIBs, K-ion batteries (KIBs), all solid-state batteries (SSBs), and multivalent batteries (MVBs).

Post-Lithium Chemistry

The need for battery chemistries beyond Li-ion is rooted in cost, which is strongly tied to the availability of lithium and the energy required for metal extraction and battery assembly.[25] For every ton of lithium that is mined, 15 tons of CO_2 are emitted into the air, and ~13 kWh of energy is required to manufacture a 32 Ah battery cell (equivalent to 410 Wh).[26] These costs are not sustainable given that the global population produces 2.4 TWh of lithium ion batteries but consumes ~24,000 TWh of energy per year.[27] There will be a variety of electrochemical energy systems used to solve the climate crisis and each one will have its application. For some applications, NIBs show great promise for replacing LIBs, especially for large scale grid storage because their lower energy density (compared to LIBs) is not as imperative as it is for EVs. The cost for a NIB cell is currently between $40-80 per kWh with an energy density of 160 Wh kg^{-1} while LIBs cost ~$120 per kWh with an energy density 250-300 Wh kg^{-1}.[28]

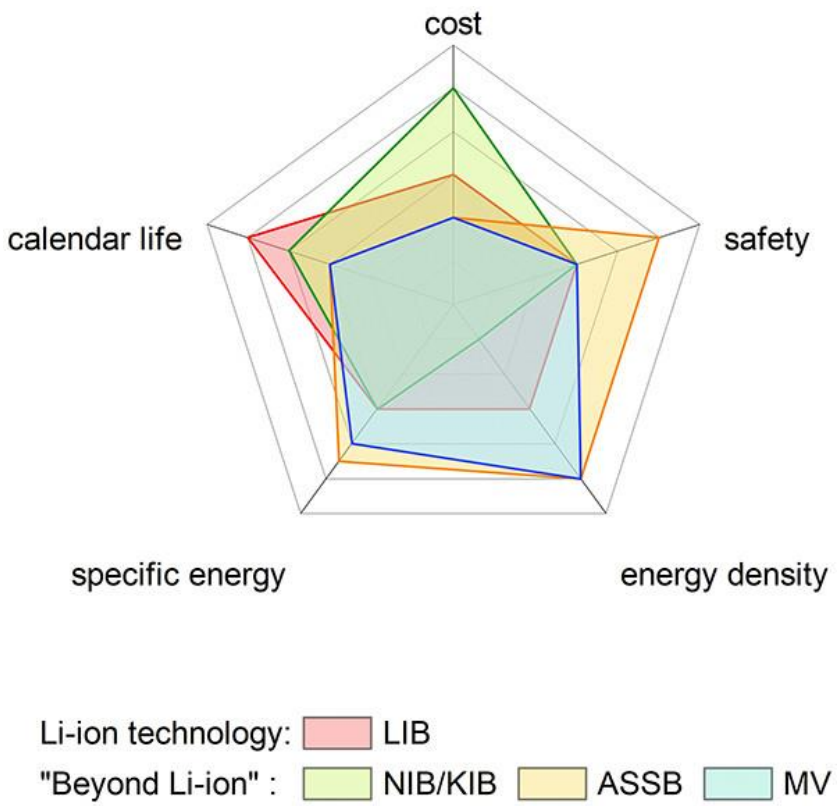

Figure 5. Considerations for next generation energy storage (Adapted from reference 29)

Sodium is a great candidate for replacing lithium because of its comparable electronegativity, molar mass, and reduction potential; what makes sodium more attractive than lithium is its abundance. Sodium is not only widely distributed worldwide but it is 420 times more abundant in earth's crust than lithium (2.74 vs. 0.0065 at %) which can assist in solving the cost crisis of LIBs.[29] The major hurdle that NIB research has to overcome is finding a suitable anode material to reversibly store Na^+ ions at high rates and low potential. Sodium does not form a stable compound with graphite higher than NaC_{48} because it loses the ionicity shown by larger alkali metals (e.g., as in KC_8) and does not achieve the covalency shown by lithium (LiC_6).[30] Figure 6 shows that lithium is in fact the ion that deviates from the trend of formation energies within graphite layers.

New carbonaceous materials are being investigated for Na-ion storage, with hard carbon (a disordered carbon that cannot be graphitized) leading the way commercially, and alloys, oxides, phosphides, etc. following behind.[31] Hard carbon offers a similar capacity, low price, and average working voltage to lithium in graphite but still faces issues concerning rate capability and cycling stability that must be overcome for use in EVs. Furthermore, the heavier weight of sodium (which is attributed to the cathode) and higher redox potential makes the cells lower in energy density.

On the anode side of a NIB, cycling stability and rate capability are important to address. The reason that the capacity of hard carbon decreases while cycling has to do with its structure and topology, which dictate how ions and electrons diffuse toward each other upon insertion. Instead of intercalating between pristine graphene sheets (as in Li^+ ions in graphite), Na^+ ions are stored as clusters inside the nanopores and defects of hard carbon, which eventually leads to exfoliation and decomposition of the electrode as it is charged and discharged over and over. For these reasons, new carbonaceous materials need to be discovered that can provide both high energy and power. An intuition behind ionic and electronic interactions at the solid-liquid interphase needs to be developed in order to conceptualize and design next generation materials.

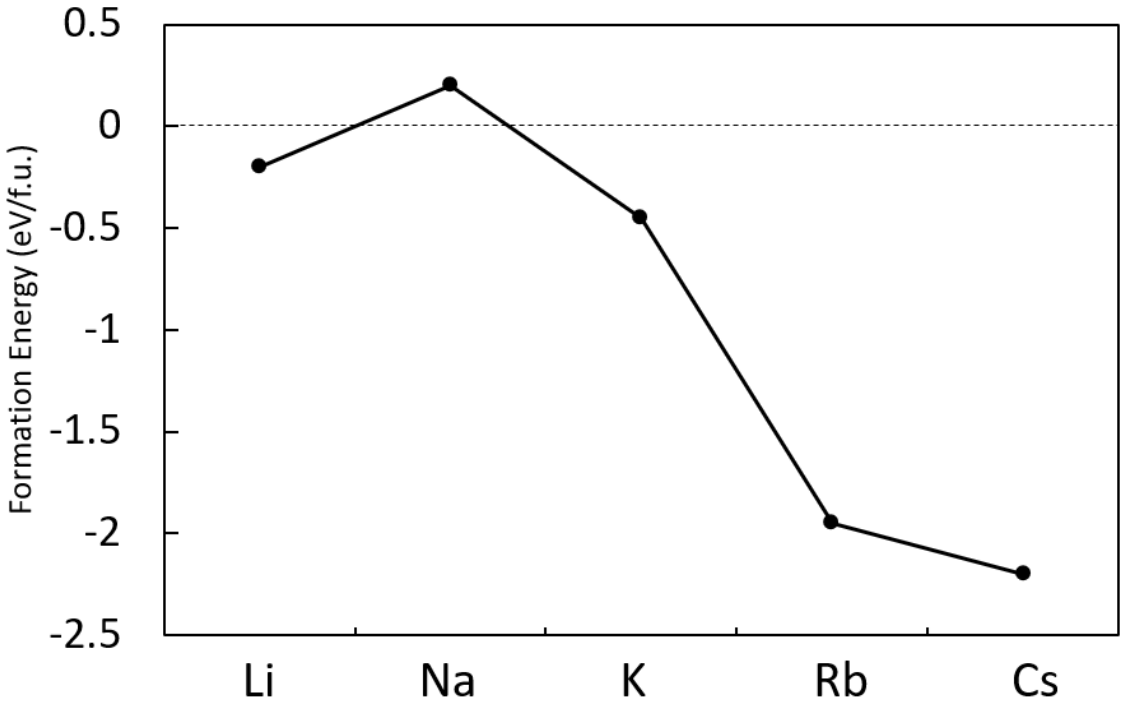

Figure 6. Calculated formation energies of AMC_6 for AM = Li, Na, K, Rb, and Cs in order of increasing atomic number. (Adapted from reference 20)

Charge Storage Mechanisms

There are many charge storage mechanisms relevant to electrochemical energy storage systems: electric double layer capacitance (EDLC), pseudocapacitance, insertion/intercalation, and alloying/conversion reactions. The studies that follow will focus on the former three mechanisms. The energy of an electrochemical cell is equal to its total charge (in Ah or C) multiplied by the potential difference between the electrodes (in V). This charge is determined by the number of electrons (each carrying one elementary charge) passed through the external circuit of the cell.[32] The capacity of a cell is equal to the number of electrons transferred between the electrodes (measured in amps) multiplied by the amount of time it takes to reach a specified voltage cutoff (measured in hours). Typically, the capacity is normalized per gram of active

material in the electrodes, this permits comparison between electrodes with different active materials and varying thickness or area. Normalization also crucially informs the electrochemist as to how close to ideal the capacity is compared to the expected final product of the reaction.

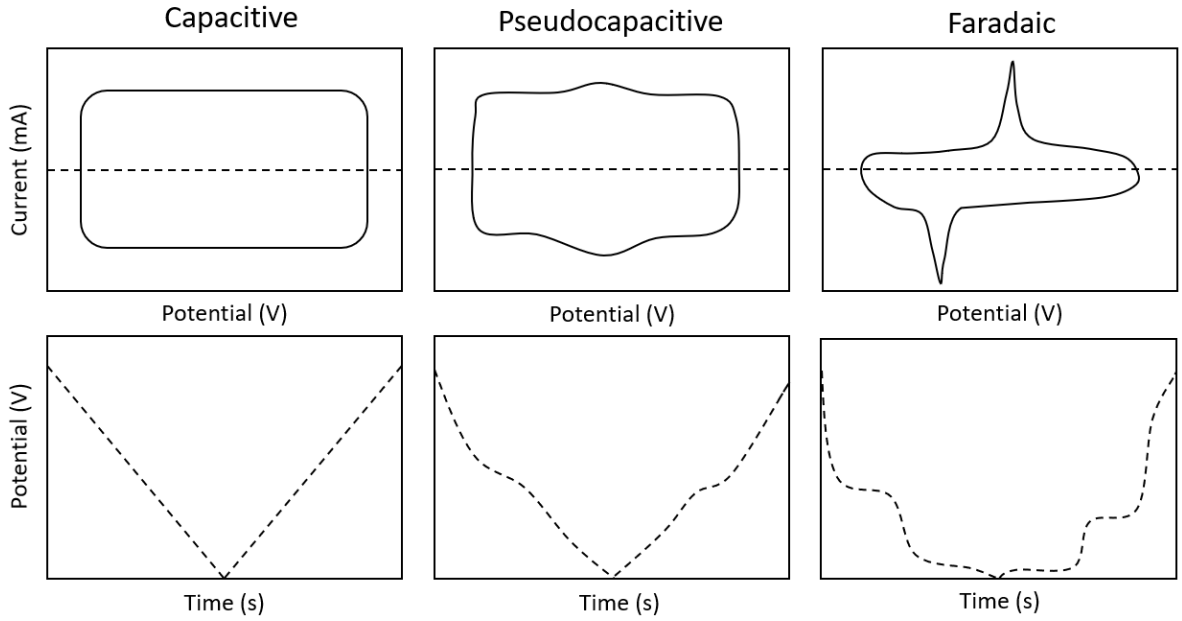

Figure 7. Schematic cyclic voltammograms and galvanostatic charge discharge profiles of characteristic charge storage mechanisms.

Capacitance operates on the adsorption of ions at a surface, forming an electrostatic attraction between the positive ion and the negatively charged host framework. Redox reactions do not take place, therefore ionic diffusion to a capacitive binding site is fast. All materials exhibit some degree of capacitance and it scales linearly with the surface area accessible to the solvent. The number of electrons that are able to be capacitively stored in a material depends on the ability of the material to accept electrons and the size of the ion together with its solvation shell. In cation storage, the positively charged ions repel each other and are separated from the electrons in the anode by a single layer of solvent molecules. Capacitance is characterized by

potential-independent current because there are no phase changes (Figure 7). The interaction is purely electrostatic and orbital overlap is nonexistent.

Intercalation or insertion on the other hand, operates on a faradaic redox reaction that occurs between the ion and the host framework. Orbital overlap and electron transfer are significant. The extent of this overlap can cause structural changes to a material whether it is minimal (e.g., as in graphite intercalated compounds) or more intensive. Highly intensive reactions can occur which completely rearrange the host material and are referred to as alloying or conversion reactions (e.g., as in the lithiation of silicon) – these too are faradaic in nature but come with the additional complexity of a phase transition of the host lattice. When fully lithiated via intercalation, graphite undergoes a phase transition from ABAB stacking to AAAA stacking (where A and B refer to relative orientation of the graphene sheets).[36] When fully lithiated via electrochemical alloying, silicon transitions from diamond-like Si to $Li_{15}Si_4$.[37] These phase transitions are evident by pronounced peaks in CV scans or plateaus in GCD profiles. The peaks and plateaus are often accompanied by hysteresis between charging and discharging because of the high activation barrier inherent to such reactions, an effect that is more pronounced at higher rates.

Capacitive and faradaic mechanisms were thought of as the two primary mechanisms of electrochemical charge storage until examples of intermediate mechanisms were observed, often referred to as pseudocapacitance. The theoretical conceptualization of pseudocapacitance was originally founded on the redox reaction between the positively charged H^+ ions and negatively charged oxide groups on RuO_2.[33] The kinetics of this reaction are rapid compared to the desolvation and intercalation of Li^+ into graphite. The mathematical models used for adsorption

cannot explain the kinetic and thermodynamic behavior of pseudocapacitance. These are neither strictly electrostatic interactions nor covalent bonds. Rather, the electron at the interface is shared enough to induce voltage-dependent current, but not enough to inhibit diffusion.[34] In RuO_2, the charge transfer between H^+ and O^- is faradaic in nature, but its electrochemical signature is capacitive because there is no phase change. Fast electron/ion diffusion can be conflated with partial electron transfer when investigating nanoscale materials. In this case, the ionic diffusion pathway is so short that faradaic charge mechanisms appear capacitive, for example as a result of nanosizing; this is considered "extrinsic" pseudocapacitance[35]. This misconception can be avoided by analyzing a varied scan rate CV experiment. If the peak current response is proportional to the square root of the scan rate, the material is faradaic. If the response is linear, it is capacitive. Rigorous electrochemical characterization must be performed on any new electrode material so that an atomistic description can be assigned. The mechanism of charge storage varies greatly based on the chemical composition of the electrode material and will not necessarily fit into three distinct categories. The mechanism should best be deduced by determining the degree of overlap that occurs between the valence orbitals of the hosted ion (e.g., H^+, Li^+, Na^+, or NH_4^+) and the polarized host material (e.g., graphite, hard carbon, RuO_2,). The strength of the bond between a solvated ion and a solid framework depends on the chemical constituents, the confinement that the host material implicates on the ion, and the local coordination number of the ion within its solvation shell.

An ongoing debate exists in the electrochemistry community regarding the distinct identity of capacitance, pseudocapacitance, and faradaic. Further abstraction and confusion can be induced when labeling a device as a supercapacitor, pseudocapacitor, or battery. In this work,

we use the term “hybrid capacitor” to refer to a cell which has multiple mechanisms contributing to its overall operation. In the end, all electrochemical charge storage chemistries lie on a spectrum and many are not solely capacitive or faradaic. Combining the fast kinetics of adsorption and the energy density of intercalation produces ideal energy storage materials. However, it is insufficient to attribute pseudocapacitance to a material based on only two electrochemical techniques; a more fundamental understanding of the chemical interaction is required.

Solvation and Confinement

Solvation thermodynamics play an important role on the interfacial kinetic dynamics of the active material during electrochemical cycling. The solvent molecules coordinated to the ion must either be stripped from the ion or accompany the ion into the pores of the active material. Desolvation will depend on how polar the solvent is and how rigid the pore walls are.[38] For example, graphite has an interlayer spacing of 3.35 Å that expands to 3.7 Å when Li-ions intercalate between the layers and up to 4.47 Å when PF_6^- ions intercalate.[1] This massive expansion can exfoliate the layers and result in a loss of crystallinity upon extended cycling. In solution, Li^+ coordinates to ~4 solvent molecules in its first solvation shell when solvated by ethylene carbonate (EC).[39] The polarity of the solvent molecule determines how many molecules will acompany the Li^+ ion into the layers of graphite. This desolvation or partial desolvation process is the rate limiting step during the charge transfer process (see Figure 8).[40] Very polar solvents (e.g., ethylene carbonate and propylene carbonate) tend to accompany lithium into graphite which benefits kinetics since it reduces the desolvation activation barrier, but this also tends to greatly expand and then exfoliate the graphite upon cycling which causes capacity

fading.[24] Less polar solvents create low viscosity, high diffusivity electrolyes but the solubility of active ions is typically very low and ions that are in solution must overcome a desolvation energy barrier prior to intercalation. A common strategy is to use a mixture of more polar and less polar solvents which can serve to balance the effects of activation energy and viscosity.

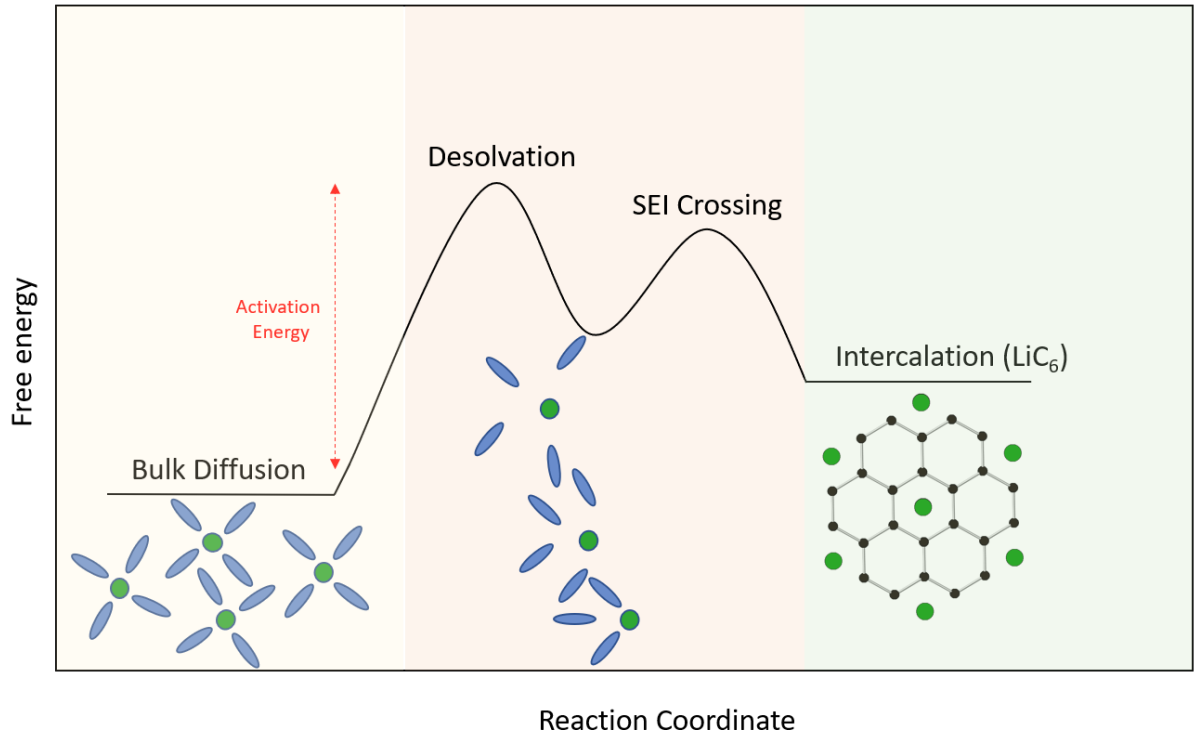

Figure 8. Reaction coordinate diagram of lithium intercalation into graphite.

Solvation affects capacitive materials differently than faradaic materials. In capacitive materials, desolvation is not necessary to form an electric double layer. The solvent molecules can simply rearrange themselves to create one layer between the host ion and the charged framework of the active material. In a faradaic material, desolvation is typically required, though this can be more complicated and depends on the active material. Carbonaceous materials with pores the same size of the Debye length of the first solvation shell around an ion can be

manipulated into being more capacitive by employing polar solvents.[41] The rate capability is enhanced because the desolvation step is not required but the charge transfer (valence orbital overlap) is reduced.

Ion pairing properties also have a significant effect on desolvation kinetics and bulk diffusion. The ionic bond between a cation and anion pair must be broken via solvation in order to dissolve a salt. However, in most cases, and especially in low dielectric constant solvents, the anion remains in the first solvatoin shell of the cation. The ideal chemical environment for cation intercalation consists of anions that disrupt the first solvation shell but do not inihbit the cation from diffusing through the electrolyte. A disrupted solvation shell lowers the desolvation activation energy but closely associated ion pairs diffuse slower than lone ions and therefore a balance should be sought.[42]

Dual Ion Batteries

Dual-ion batteries (DIBs) and capacitors (DICs) are a promising replacement to LIBs and post-LIB chemistries because they do not require the use of transition metals, which can be expensive, toxic, and environmentally damaging to extract.[43] Instead, the electrodes of a DIB can both be composed of carbon, making such a cell a reliably and sustainably resourced energy storage system. McCullough presented the first dual-carbon cell in 1989 that utilized ion intercalation into graphite at both the anode and cathode.[44] In contrast to the rocking chair mechanism of LIBs, DIBs and DICs utilize both the cation and anion as the charge-carrying ion at each electrode. Instead of the cathode, it is the electrolyte that supplies all of the active ions, which are depleted from the electrolyte upon charging: cations moving into the anode and anions moving into the cathode. The electrolyte accounts for a large amount of the cell mass since it

plays the role of storing the active ions in the discharged state. Thereore, high concentration electrolytes (e.g., >3M) are used to maximize energy density in DIBs/DICs.[45] For this reason,DIBs would be especially useful in competition with hydroelectric and other grid storage applications where energy density is not the primary concern. The basic properties of the electrolyte change dramatically as the state of charge of the cell changes. While charging, the viscosity decreases and the ionic conductivity increases, suggesting that the rate capability is voltage dependent. Just like LIBs, the anode and cathode of a DIB must be capacity balanced. For example, dual-graphite batteries store anions and cations in between the layers of graphite (cations at the graphite anode and anions at the graphite cathode), but many more Li^+ ions can be stored in graphite than PF_6^- ions. Therefore, the ratio of the anode mass to the cathode mass must be <1 as a means to maximize the voltage window and therefore energy density of the full-cell. Similar issues are at play in designing a full-cell of any kind. However, for DICs in particular, where both electrodes show voltage independent current, the mass balance must be calculated from the voltage window and capacitance of each electrode:

$$q_+ = q_- \rightarrow m_+ \Delta V_+ C_+ = m_- \Delta V_- C_- \rightarrow \frac{m_-}{m_+} = \frac{\Delta V_+ C_+}{\Delta V_- C_-} \quad (3)$$

where q, m, ΔV, and C are the absolute capacity (in Ah), mass of each electrode (in g), difference in potential between the electrodes (in V), and capacitance (in F) which is calculated as:

$$\mathrm{C} = \frac{\mathrm{i}\Delta\mathrm{t}}{\mathrm{m}\Delta\mathrm{V}} \quad (4)$$

where i, Δt, m, and ΔV are current (in A), time of discharge (in s), total mass of carbon included in both electrodes (in g), and working voltage (in V). Obtaining the maximum utilization of each electrode directly corresponds to maximizing the energy density. However, cycling the cell at high voltage differences is not always optimal if it means the cycling stability will suffer. High

voltages can lead to electrolyte decomposition, corrosion of the aluminum current collector, plating of solid metal to the anode, and/or exfoliation of the active material.

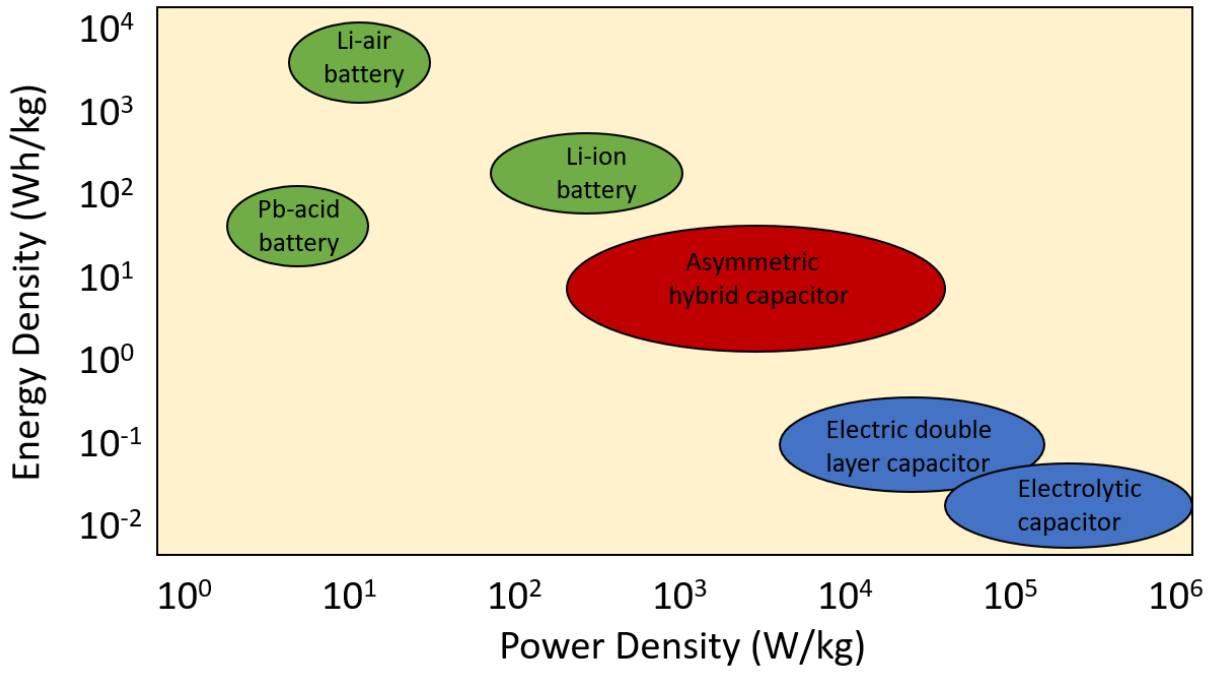

Figure 9. Ragone plot of relevant energy storage systems.

For DIBs to achieve high energy densities, they must operate at high voltages and ion concentrations, which has inspired creative strategies. DIBs are typically operated at voltages above 4.2 V vs Li/Li^+. Many standard LIB electrolytes (typically based on carbonate or ether solvents) begin to decompose at voltages above 3.7 V vs Li/Li^+; therefore, more electrochemically stable electrolytes such as ionic liquids, glymes, and fluorinated solvents are of highest interest. High concentration electrolytes for DIBs can reach up to ~5 M (where molarity is non-trivially related to the original volume of solvent and molality is often preferred), which ineveitably introduces high viscosities. Ions are paired at a closer distance in highly concentrated electrolytes which slows their diffusivity through the solvent. Rate capabilities are therefore a

greater challenge compared to the commercially used LIB electrolytes (typically ~1 M). However, if these problems can be overcome, DIBs may be able to meet a needed balance between energy and power density while remaining cost effective and sustainable for grid storage.

Electrical Conductivity in Porous Frameworks

It is rare for porosity and electrical conductivity to coexist in one material. Conductivity depends on the efficacy of electron transport within a material, which is correlated to the charge carrier concentration and mobility. Generally, conductivity can be split into two different mechanisms, hopping transport and band-like transport.[46] Both mechanisms require overlap between orbitals of correct symmetry. Hopping requires an activation energy to move an electron between one localized site to another, this is more common in insulators and semiconductors. Band transport depends on delocalized charge carriers moving freely between energy bands, this is more common in conductors. The difference in the two mechanisms can be characterized experimentally via temperature dependence conductivity, hopping mechanisms are always thermally activated whereas band-like mecahnisms can be either activated or deactivated. Insulators and semiconductors become more conductive as they are heated because electrons move from the valence band to the conduction band, increasing the concentration of free charge carriers. Metals become less conductive as they are heated because of thermal vibrations and expansion that impede the movement of free charge carriers.

Metallic bonds form between transition metals with low electronegativities which delocalizes their valence electrons into the Fermi level.[47] The most conductive metals (Ag, Cu, Au, Al, etc.) fit into three close packing crystal structures: body-centered cubic (bcc), face-

centered cubic (fcc), and hexagonal close-packed (hcp).[48] The metallic atoms can fit this close together because discrete electron-pair bonds aren't necessary, instead a delocalized "cloud" of electrons is exhibited. The band gap narrows from insulators to semiconductors to metals as the degree of electron delocalization increases (Figure 10). Usually, the band gap of an insulator is greater than 4 eV, a metal has no band gap and a semiconductor is between that of an insulator and a metal. Metals are used to fabricate capacitors since they are rapid conductors of electricity. The problem with using metals for electrochemical energy storage (e.g., in a supercapacitor or EDLC) is that they are non-porous and therefore cannot accommodate a large number of ions per mass. The energy density achieved from plating/stripping reactions at a metal surface is ideal, but often found to be unsafe in an electrochemical cell because of dendrite formation (this is highly dependent on the metal ion and the electrolyte, with some important counter examples such as potassium). However, designing porous materials with the conductivity mechanisms of metals is an ongoing effort in the solid-state chemistry community .

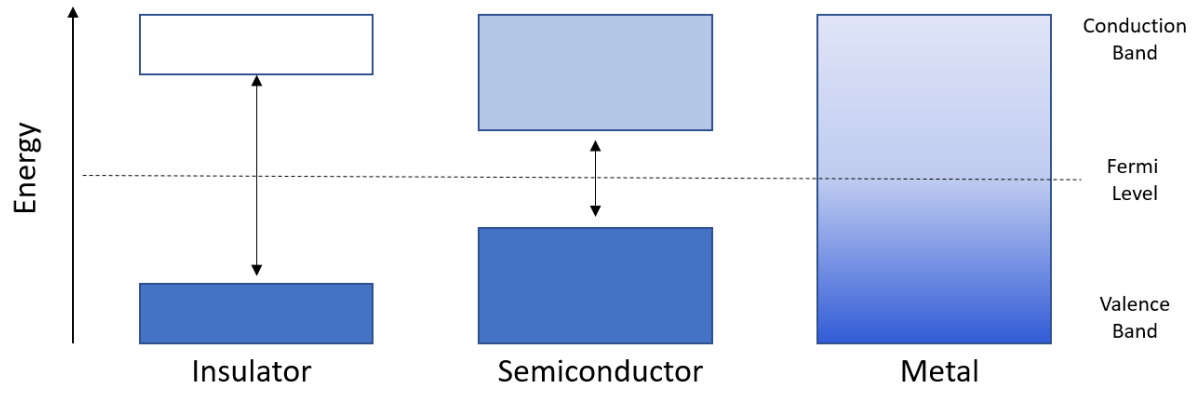

Figure 10. Electronic structure of an insulator, semicoductor, and metal.

Porous materials that retain conductivity are highly sought after. Carbons with high surface area have been extensively investigated for use in LIBs. Activated carbons and other variants of porous carbon consist of sp^2 hybridized carbon atoms, covalently bound in a locally planar hexagonal lattice. These 2D planes tend to stack on top of each other due to π- π orbital interactions, but can be pulled apart to create pores by introducing structural defects (activation) or by bottom-up design. The electron in the unhybridized p_z orbital is perpendicular to the layers and acts as the charge carrier. The conductivity is largely anisotropic; along the bonding plane it is at least 10,000 times more conductive than between planes.[49] Because of this, grain size engineering or additives are used to enhance the connectivity between oriented particles of conductive porous carbon. New porous materials that have inherent conductivity and connectivity in all three dimensions are necessary for post-Li-ion chemistries.

ZTCs also show promise for electrode materials because of the tunability of the silica template. Carbonacous materials are generally desirable as battery electrodes because of their high conductivity, low cost, and low density. Zeolites are a class of over 270 unique framework structures of microporous aluminosilicates. Only ~25 of these are suitable for carbon templating because they have three-dimesnonally connected pores that can host carbon precursors.[53] This work focuses on carbon templates of the FAU and IWV zeolites. ZTCs templated from the faujasite zeolite (FAU) offer up to 3300 $m^2\ g^{-1}$ of surface area and 1.2 nm ordered, porous channels through which ions can travel.[54] FAU crystallizes in the cubic space group, $Fd\bar{3}m$, made up of sodalite cages which are connected by hexagonal prisms (herein referred to as 3D ZTC). ZTCs templated from the orthorhombic IWV zeolite forms large two-dimensional microporous channels (12.3 Å) and a surface area of 156 $m^2\ g^{-1}$ (herein referred to as 2D ZTC). A dense silica

layer constrains carbon templating in the *a* direction which leaves single layer graphene sheets in the *b* and *c* directions. After the silica is etched away these layers stack on top of each other 3.56 Å apart to form sheet-like particles that are 30 nm thick.[55] The electrical conductivity of these two ZTCs are highly comparable given that they are both built out of sp^2-hybridized carbon networks. 2D ZTC band-like conductivity along the basal planes, similar to graphite, with less conductivity along the edge plane due to it wider interlayer spacing. The graphene sheets in 3D ZTC do not experience the same π- π through space conductivity because of distance between pores. Instead they rely on continuous energy bands with delocalized charge carriers that move diffuse electrons via the aromatic network. The continuity of these pathways depends on a high degree of pore order and crystallinity which reduces the number of edge sites that would disrupt carbon-carbon sigma bond conductivity.[56]

Another category of porous materials is metal-organic frameworks (MOFs). MOFs comprise a metal-oxo or metal-nitrido node and an organic linker, coordinated in a structural topology that can be 1D, 2D, or 3D connected, and offer wide tunability in pore size and composition. Hence, MOFs can be readily designed to accomodate ions of any size. However, MOFs lack low-energy charge-transport pathways and therefore suffer from low conductivity. The two most common ways to solve this problem synthetically are by enhancing "through-bond" or "through-space" conductivity pathways.[50] The former targets the covalent overlap of the metal-ligand, d-π orbitals which in turn delocalizes the charge. The latter targets charge transport through non-covalent interactions such as π- π stacking or redox hopping.[51] The dimensionality of the MOF will dictate both the electrical conductivity and the conductivity pathway. The topology of the underlying structure determines the proximity of the ligands which

will either lead to through-bond or through-space being the dominant pathway.[52] Reducing the size of the unit cell by utilizing smaller or more electronegative metal centers can bring the aromatic linkers closer to each other. Tuning the interlayer distance with the metal-organic-moieties is highly relevant to electrochemical ion storage. Ordered materials with highly crystalline pores provide clarity with respect to charge storage mechanisms. One class of metal ions that provide interesting tunability for fundamental structure-function relationships in MOFs are the lanthanides. They are trivalent with empty 5d shells which in turn form ionic bonds with the chelating functional groups on a given ligand. This allows for flexibility in how the MOF's structure forms based on synthetic conditions such as temperature and equivalence. MOFs constructed with the same constituents can give rise to vastly different symmetry, conductive pathways, and compositional ratios.

Two sets of frameworks are investigated in these studies, one is largely carbonaceous and the other is a metal-organic moiety. Both sets have 2D and 3D topological analogs that are compositionally interchangeable. The symmetric similarities between the two sets provide insight into the nature of conductivity in porous frameworks.

References

(1) Asenbauer, J.; Eisenmann, T.; Kuenzel, M.; Kazzazi, A.; Chen, Z.; Bresser, D. The Success Story of Graphite as a Lithium-Ion Anode Material – Fundamentals, Remaining Challenges, and Recent Developments Including Silicon (Oxide) Composites. Sustainable Energy & Fuels 2020, 4 (11), 5387-5416.

(2) Song, W.; Teng, X.; Liu, Y.; Wang, J.; Niu, Y.; He, X.; Zhang, C.; Chen, Z. Rational Construction of Self-Supported Triangle-Like Mof-Derived Hollow (Ni,Co)Se(2) Arrays for Electrocatalysis and Supercapacitors. Nanoscale 2019, 11 (13), 6401-6409.

(3) Wang, Y.; Liu, Y.; Wang, H.; Liu, W.; Li, Y.; Zhang, J.; Hou, H.; Yang, J. Ultrathin Nico-Mof Nanosheets for High-Performance Supercapacitor Electrodes. ACS Applied Energy Materials 2019, 2 (3), 2063-2071.

(4) Mehek, R.; Iqbal, N.; Noor, T.; Amjad, M. Z. B.; Ali, G.; Vignarooban, K.; Khan, M. A. Metal-Organic Framework Based Electrode Materials for Lithium-Ion Batteries: A Review. RSC Adv 2021, 11 (47), 29247-29266.

(5) Nasalevich, M. A.; van der Veen, M.; Kapteijn, F.; Gascon, J. Metal–Organic Frameworks as Heterogeneous Photocatalysts: Advantages and Challenges. CrystEngComm 2014, 16 (23), 4919-4926.

(6) Liu, M.; Wang, Y.; Wu, F.; Bai, Y.; Li, Y.; Gong, Y.; Feng, X.; Li, Y.; Wang, X.; Wu, C. Advances in Carbon Materials for Sodium and Potassium Storage. Advanced Functional Materials 2022, 32 (31).

(7) Statistical Review of World Energy; 2023.

(8) May 2024 Monthly Energy Review; U.S. Emergy Information Administration, 2024.

(9) Degen, F.; Winter, M.; Bendig, D.; Tübke, J. Energy Consumption of Current and Future Production of Lithium-Ion and Post Lithium-Ion Battery Cells. Nature Energy 2023, 8 (11), 1284-1295.

(10) Layton, B. E. A Comparison of Energy Densities of Prevalent Energy Sources in Units of Joules Per Cubic Meter. International Journal of Green Energy 2008, 5 (6), 438-455.

(11) Erik Emilsson, L. D. Lithium Ion Vehicle Production; Swedish Environmental Research Institute, 2019.

(12) Joyce McLaren, J. M.; Eric O'Shaughnessy, E. W., and Evan Shapiro. Emissions Associated with Electric Vehicle Charging: Impact of Electricity Generation Mix, Charging Infrastructure Availability, and Vehicle Type; National Renewable Energy Laboratory, 2016.

(13) Boyden, A.; Soo, V. K.; Doolan, M. The Environmental Impacts of Recycling Portable Lithium-Ion Batteries. Procedia CIRP 2016, 48, 188-193.

(14) Ballantyne, A. D.; Hallett, J. P.; Riley, D. J.; Shah, N.; Payne, D. J. Lead Acid Battery Recycling for the Twenty-First Century. R Soc Open Sci 2018, 5 (5), 171368.

(15) Division, E. S. Cradle-to-Grave Lifecycle Analysis of U.S. Light-Duty Vehicle-Fuel Pathways: A Greenhouse Gas Emissions and Economic Assessment of Current (2020) and Future (2030-2035) Technologies; Argonne National Lab, 2020.

(16) K. Mizushima, P. C. J., P. J. Wiseman and J. B. Goodenough. Lixcoo2 (0<X~L): A New Cathode Material for Materials of High Energy Density. Materials Research Bulletin 1980.

(17) Whittingham, M. S. Electrical Energy Storage and Intercalation Chemistry. Science 1976, 192 (4244), 1126-1127.

(18) Yoshino, A. The Birth of the Lithium-Ion Battery. Angew Chem Int Ed Engl 2012, 51 (24), 5798-5800.

(19) Touzain, R. Y. a. P. A Reversible Graphite-Lithium Negative Electrode for Electrochemical Generators. Jounral of Power Sources 1982, 9, 365-371.

(20) Bruce Dunn, H. K., Jean-Marie Tarascon. Electrical Energy Storage for the Grid: A Battery of Choices. Science 2011, 334 (6058), 928-935.

(21) Manthiram, A. An Outlook on Lithium Ion Battery Technology. ACS Cent Sci 2017, 3 (10), 1063-1069.

(22) Winter, M.; Barnett, B.; Xu, K. Before Li Ion Batteries. Chem Rev 2018, 118 (23), 11433-11456.

(23) Yazami, P. T. a. R. Lithium-Graphitic Oxide Cells. Journal of Power Sources 1985, 14, 99-104.

(24) Rosamaria Fong, U. v. S., and J. R. Dahn. Studies of Lithium Intercalation into Carbons Using Nonaqueous Electrochemical Cells. Journal of the Electrochical Society 1990.

(25) Dunn, J. B.; Gaines, L.; Kelly, J. C.; James, C.; Gallagher, K. G. The Significance of Li-Ion Batteries in Electric Vehicle Life-Cycle Energy and Emissions and Recycling's Role in Its Reduction. Energy & Environmental Science 2015, 8 (1), 158-168.

(26) Davidsson Kurland, S. Energy Use for Gwh-Scale Lithium-Ion Battery Production. Environmental Research Communications 2019, 2 (1).

(27) Ahmad, T.; Zhang, D. A Critical Review of Comparative Global Historical Energy Consumption and Future Demand: The Story Told So Far. Energy Reports 2020, 6, 1973-1991.

(28) IRENA. World Energy Transitions Outlook 2023; International Renewable Energy Agency, 2023.

(29) Tan, S.; Yang, H.; Zhang, Z.; Xu, X.; Xu, Y.; Zhou, J.; Zhou, X.; Pan, Z.; Rao, X.; Gu, Y.; et al. The Progress of Hard Carbon as an Anode Material in Sodium-Ion Batteries. Molecules 2023, 28 (7).

(30) Moriwake, H.; Kuwabara, A.; Fisher, C. A. J.; Ikuhara, Y. Why Is Sodium-Intercalated Graphite Unstable? RSC Advances 2017, 7 (58), 36550-36554.

(31) Deng, J.; Luo, W. B.; Chou, S. L.; Liu, H. K.; Dou, S. X. Sodium-Ion Batteries: From Academic Research to Practical Commercialization. Advanced Energy Materials 2017, 8 (4).

(32) Conway, B. E. Transition from "Supercapacitor" to "Battery" Behavior in

Electrochemical Energy Storage Electrochemical Science and Technology 1991, 138.

(33) Sergio Trasatti, a. G. B. Ruthenium Dioxide: A New Interesting Electrode Material. Solid State Structure and Electrochemical Behaviour ELECTROANALYTICAL CHEMISTRY AND INTERFACIAL ELECTROCHEMISTRY 1970.

(34) Fleischmann, S.; Mitchell, J. B.; Wang, R.; Zhan, C.; Jiang, D. E.; Presser, V.; Augustyn, V. Pseudocapacitance: From Fundamental Understanding to High Power Energy Storage Materials. Chem Rev 2020, 120 (14), 6738-6782.

(35) Gogotsi, P. S. a. Y. Materials for Electrochemical Capacitors. Nature Materials 2008.

(36) Liu, Q.; Li, S.; Wang, S.; Zhang, X.; Zhou, S.; Bai, Y.; Zheng, J.; Lu, X. Kinetically Determined Phase Transition from Stage Ii (Lic(12)) to Stage I (Lic(6)) in a Graphite Anode for Li-Ion Batteries. J Phys Chem Lett 2018, 9 (18), 5567-5573.

(37) Domi, Y.; Usui, H.; Ando, A.; Nishikawa, K.; Sakaguchi, H. Analysis of the Li Distribution in Si-Based Negative Electrodes for Lithium-Ion Batteries by Soft X-Ray Emission Spectroscopy. ACS Applied Energy Materials 2020, 3 (9), 8619-8626.

(38) Biesheuvel, P. M.; Porada, S.; Levi, M.; Bazant, M. Z. Attractive Forces in Microporous Carbon Electrodes for Capacitive Deionization. Journal of Solid State Electrochemistry 2014, 18 (5), 1365-1376.

(39) Pham, T. A.; Kweon, K. E.; Samanta, A.; Lordi, V.; Pask, J. E. Solvation and Dynamics of Sodium and Potassium in Ethylene Carbonate from Ab Initio Molecular Dynamics Simulations. The Journal of Physical Chemistry C 2017, 121 (40), 21913-21920.

(40) Tao, L.; Xia, D.; Sittisomwong, P.; Zhang, H.; Lai, J.; Hwang, S.; Li, T.; Ma, B.; Hu, A.; Min, J.; et al. Solvent-Mediated, Reversible Ternary Graphite Intercalation Compounds for Extreme-Condition Li-Ion Batteries. J Am Chem Soc 2024.

(41) Fleischmann, S.; Zhang, Y.; Wang, X.; Cummings, P. T.; Wu, J.; Simon, P.; Gogotsi, Y.; Presser, V.; Augustyn, V. Continuous Transition from Double-Layer to Faradaic Charge Storage in Confined Electrolytes. Nature Energy 2022, 7 (3), 222-228.

(42) Cheng, H.; Ma, Z.; Kumar, P.; Liang, H.; Cao, Z.; Xie, H.; Cavallo, L.; Kim, H.; Li, Q.; Sun, Y. K.; et al. High Voltage Electrolyte Design Mediated by Advanced Solvation Chemistry toward High Energy Density and Fast Charging Lithium-Ion Batteries. Advanced Energy Materials 2024, 14 (18).

(43) Read, J. A.; Cresce, A. V.; Ervin, M. H.; Xu, K. Dual-Graphite Chemistry Enabled by a High Voltage Electrolyte. Energy Environ. Sci. 2014, 7 (2), 617-620.

(44) Frances P. McCullough, C. A. L., Roy V. Snelgrove. Secondary Battery. 1989.

(45) Wrogemann, J. M.; Haneke, L.; Ramireddy, T.; Frerichs, J. E.; Sultana, I.; Chen, Y. I.; Brink, F.; Hansen, M. R.; Winter, M.; Glushenkov, A. M.; et al. Advanced Dual-Ion Batteries with High-Capacity Negative Electrodes Incorporating Black Phosphorus. Adv Sci (Weinh) 2022, 9 (20), e2201116.

(46) Stallinga, P. Electronic Transport in Organic Materials: Comparison of Band Theory with Percolation/(Variable Range) Hopping Theory. Adv Mater 2011, 23 (30), 3356-3362.

(47) Carl-Friedrich Schön, S. v. B., Christian Mattes, Aakash Yadav, Martin Grohe, Leif Kobbelt, Matthias Wuttig. Classification of Properties and Their Relation to Chemical Bonding: Essential Steps toward the Inverse Design of Functional Materials. Science Advances 2022, 8.

(48) Per Soderlind, O. E., Borje Johansson, J. M. Wilist, A. M. Borlng A Unified Picture of the Crystal Structures of Metals. Letters to Nature 1996, 374.

(49) Ganguli, K. S. K. a. N. Large Anisotropy of the Electrical Conductivity of Graphite. Nature Energy 1939, 144.

(50) Li, J.; Kumar, A.; Ott, S. Diffusional Electron Transport Coupled to Thermodynamically Driven Electron Transfers in Redox-Conductive Multivariate Metal-Organic Frameworks. J Am Chem Soc 2024, 146 (17), 12000-12010.

(51) Saha, R.; Gupta, K.; Gomez Garcia, C. J. Strategies to Improve Electrical Conductivity in Metal-Organic Frameworks: A Comparative Study. Cryst Growth Des 2024, 24 (5), 2235-2265.

(52) Skorupskii, G.; Trump, B. A.; Kasel, T. W.; Brown, C. M.; Hendon, C. H.; Dinca, M. Efficient and Tunable One-Dimensional Charge Transport in Layered Lanthanide Metal-Organic Frameworks. Nat Chem 2020, 12 (2), 131-136.

(53) Taylor, E. E.; Garman, K.; Stadie, N. P. Atomistic Structures of Zeolite-Templated Carbon. Chemistry of Materials 2020, 32 (7), 2742-2752.

(54) Itoi, H.; Nishihara, H.; Kogure, T.; Kyotani, T. Three-Dimensionally Arrayed and Mutually Connected 1.2-Nm Nanopores for High-Performance Electric Double Layer Capacitor. J Am Chem Soc 2011, 133 (5), 1165-1167.

(55) Chaehoon Kim, D.-Y. K., Yongjin Lee, Jihoon Choi, Hae Sung Cho, Minkee Choi. Bottom-up Synthesis of Two-Dimensional Carbon with Vertically Aligned Ordered Micropores for Ultrafast Nanofiltration. Science Advances 2023, 9.

(56) Lee, H.; Kim, K.; Kang, S. H.; Kwon, Y.; Kim, J. H.; Kwon, Y. K.; Ryoo, R.; Park, J. Y. Extremely High Electrical Conductance of Microporous 3d Graphene-Like Zeolite-Templated Carbon Framework. Sci Rep 2017, 7 (1), 11460.

CHAPTER TWO

METHODS AND METHODOLOGY

YHOTP and Y_6HOTP_2 MOF Synthesis and Characterization

HHTP Recrystallization

2,3,6,7,10,11-Hexahydroxytriphenylene (HHTP) is received at >95% purity from the supplier and must be stored under inert atmosphere. HHTP needs to be recrystallized twice in preparation for YHOTP and Y_6HOTP_2 synthesis. Single crystals large enough for XRD are unattainable unless HHTP is sufficiently pure. 1 g of HHTP is dissolved in 10 mL of DMI while 500 mL of H_2O is boiled. 5 mL of acetic acid is added to the boiling water to create acidic conditions before HHTP addition. The well dissolved (heat can be used) HHTP solution is filtered through a 0.2 μm PTFE filter and added to the boiling water. The hot plate is turned off and the solution is left to mix for 5 minutes before being added to an ice bath. After 1 hour of cooling light brown crystals of HHTP should start to appear. Use a buchner funnel and filter paper to collect the product and wash 3x with and DI 3x with methanol. Repeat this process. Dry under vacuum at 90°C overnight and store under inert atmosphere. When performing 2 recrystallizations it is important to retain as much material as possible throughout the first recrystallization.

Single-Crystal Growth

Large single crystals of MOFs are imperative for advanced characterization techniques such as single crystal XRD, temperature dependent conductivity, AFM, and 4 point probe conductivity. Single crystal XRD provides a clear picture of the topology and the bonding

environment that powder XRD cannot always offer. Single crystal conductivity eliminates resistance contributions from grain boundaries, material anisotropy and contact lead resistance. Linker purity, deoxygenated solvents, filtration techniques, and nucleation are all important aspects to consider when growing large single crystals.

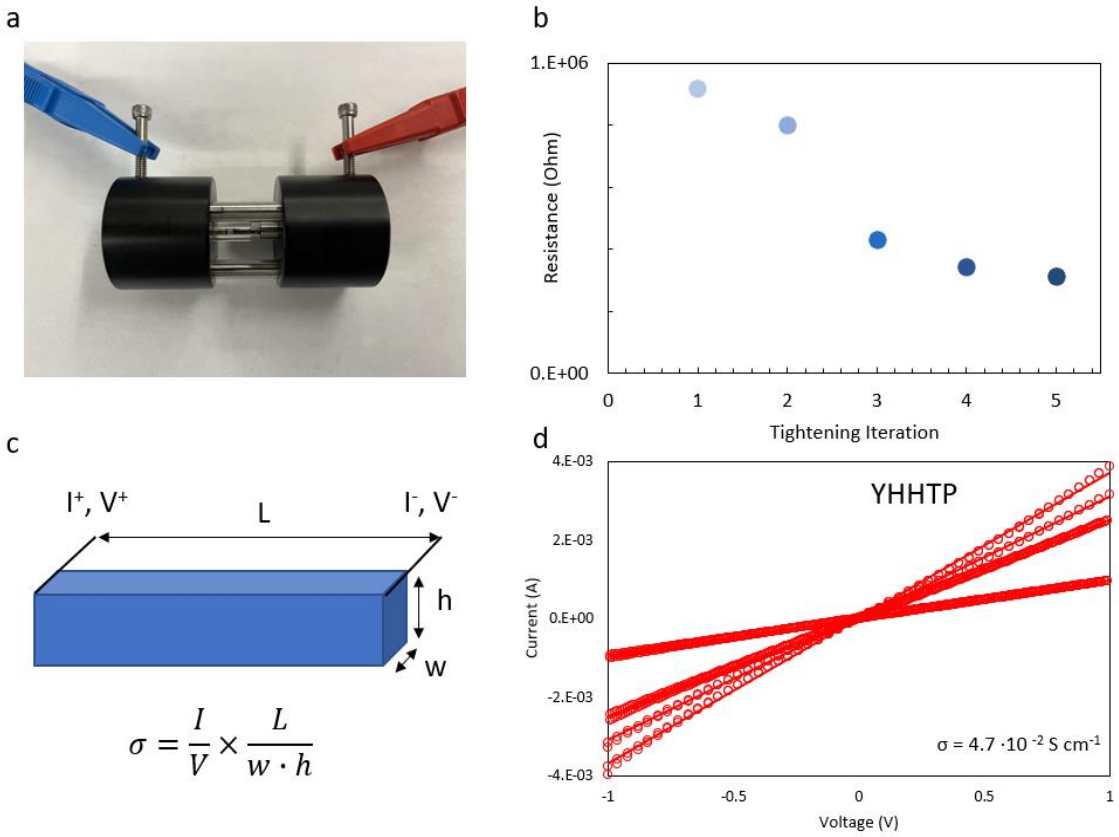

Figure 1. 2-point pressed pellet conductivity method a) conductivity apparatus b) tightening iterations c) schematic of conductivity calculation and d) repeat measurements error deviation

Conductivity Measurements

Band structure calculations are relevant towards understanding charge transport in MOFs, but should be backed up by real, experimental transport properties. Pressed pellet conductivities can be measured for any microcrystalline powder that are insufficient for single crystal 4-point probe conductivity. The maximum conductivity measurable with this apparatus is 20 S cm^{-1}

when using copper components. To obtain reliable results pellets should be completely dry and be at least 0.5 mm thick when not pressed. To maximize surface contact between particles and across grain boundaries, a vice should be used to tighten the apparatus. When the resistance changes by less than 1 mΩ between tightening iterations, the pellet is adequately pressed (see Figure 1d). If overtightened the glass tube containing the pellet can shatter and shards can be sent flying. After collecting an IV curve, the pellet is measured by inserting titanium rods with known length in either side of the glass tube. Using a digital micrometer, accuracy up to 0.01 mm can be reported. Knowing the resistance, diameter, and length of the pellet and employing Ohm's law, conductivity can be calculated using the equation in Figure 1c. 5 different pellets of the same material should be measured and averaged to reduce the experimental error associated with pellet compression and measurement.

Electrochemical Cell Techniques

Detailed Slurry Casting Technique

Electrode casting is the most important step towards making high quality electrochemical cells. Without strong adhesion of the substrate to the foil, proper homogenization of active material, and consistency from slurry to slurry, conclusions cannot be made about the inherent properties of a material. Quality control must be considered for every component; activated material, binder and solvent refreshed before every slurry cast, mortar and pestle dried at 120°C etc. Developing a feel for slurry preparation by hand is helpful given that humidity and temperature can change and will effect a machined slurry mixer.

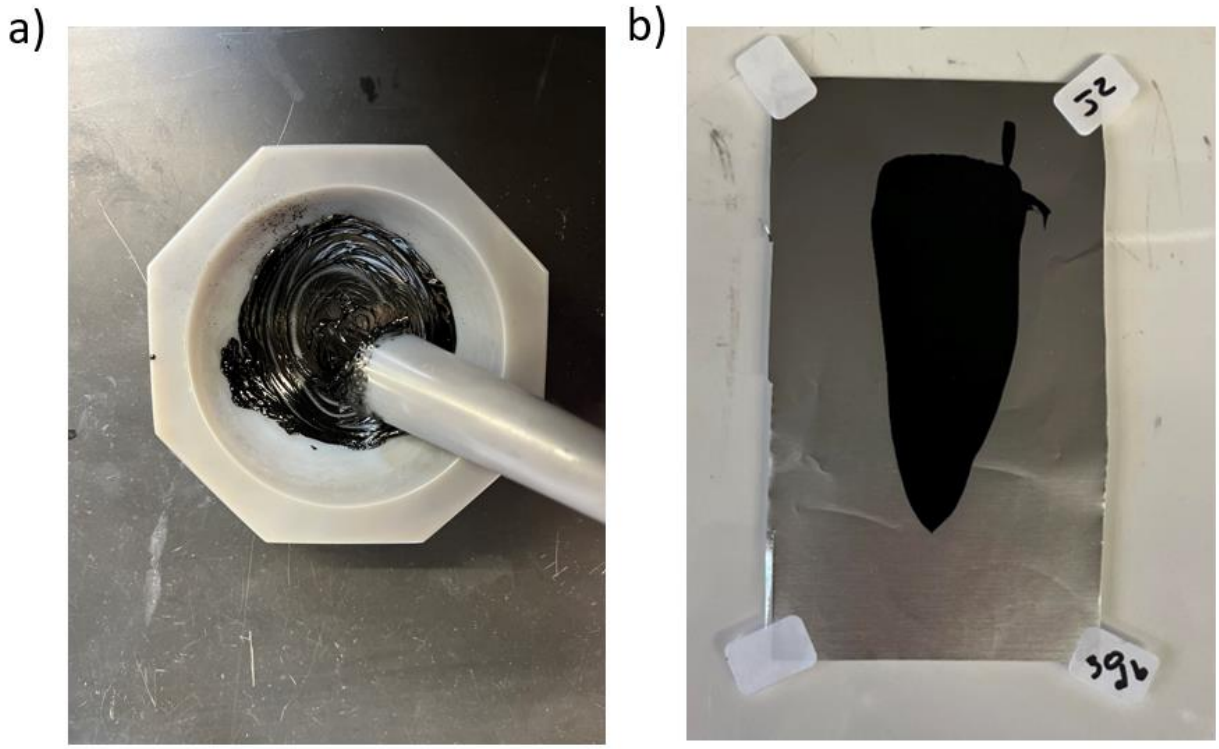

Figure 2. Slurry casting techniques (a) ideal slurry viscosity before casting (b) a slurry cast that will accommodate ~12 electrodes.

Hand grinding of the dry powders (active material and conductive additive) should be done for at least 15 minutes, grinding them with the mortar and pestle and breaking up large agglomerates with a spatula. Addition of the binder, whether it is PVDF in NMP or CMC in H_2O should happen before any extra solvent is added. Cut off the last couple of mm of the pipette tip in order to pull up the viscous binder solution. Be sure to dispense all of the binder by pressing the pipette tip against the mortar. Grind for 1-2 minutes, the consistency of the slurry should be that of chalk. If the surface area of the active material is low or the ratio of binder is high, the slurry consistency could be satisfactory. If the surface area is high or a low ratio of binder is being used, extra solvent will be needed. Add the solvent in aliquots no larger than ¼ the amount of binder used. Grind for 1-2 minutes between each addition until the slurry is the consistency of

soup. To check this, scoop the slurry to the middle of the mortar with a spatula and tilt the mortar 45°, if the slurry drips 1 centimeter over 5 seconds, the consistency is satisfactory. Prepare the foil (Cu for anodes, Al for cathodes) on a glass slide and clean with isopropyl alcohol and kimwipes. This step is very important for getting air bubbles out from under the foil and also must be done quickly as the slurry can dry out. Dab the slurry at the top third of the foil and drag the doctor blade over the slurry at a consistent pace. The doctor blade height will determine the thickness of the electrode, 15 μm is a good starting point. Tape the corners of the foil to avoid wrinkling during drying. Slowly dry the slurry cast at 35°C for 1 hour, then at 80°C for 2 hours, and finally under vacuum at 100°C for 12 hrs.

Coin Cell Fabrication

Standard coin cell fabrication procedures are described in the manuscript experimental sections but specific details that were left out will be described here. When building half cells, it is important to scrape off the oxide layer of the metal using a knife but to accommodate for the extra space the metal takes, a 0.5 mm thick spacer should be used. In full cell set ups, 1 mm spacers should be used to provide adequate compression. Given how small the electrodes are compared to the coin cell cases (10 mm vs 18 mm diameter), lining up the anode and cathode on either side of the separator helps diffusion kinetics. After dispensing the 125 μl of electrolyte and placing the cathode then spacer on top of it, apply pressure until liquid seeps out the side of the separator. If concentrated electrolyte is being used it should be heated before pipetting to avoid high viscosities. A full crimp will ensure the positive case is wrapped around the negative case to the point that no edge can be felt.

CHAPTER THREE

METHODOLOGICAL STUDIES OF THE MECHANISM OF ANION INSERTION IN NANOMETER-SIZED CARBON MICROPORES

Contribution of Authors and Co-Authors

Manuscript in Chapter 3

Author: Connor Welty

Contributions: Fabricated electrochemical cells, collected data, analyzed data, produced figures, and wrote the manuscript

Co-Author: Erin E. Taylor

Contributions: Synthesized material

Co-Author: Sadie Posey

Contributions: Assisted with data collection

Co-Author: Kostiantyn V. Kravchyk

Contributions: Provided intellectual advice

Co-Author: Maksym V. Kovalenko

Contributions: Provided intellectual advice

Co-Author: Nicholas P. Stadie

Contributions: Advised with the experimental direction, interpreted results, and assisted in writing and editing the manuscript

Manuscript Information

Connor Welty, Erin E. Taylor, Sadie Posey, Kostiantyn V. Kravchyk, Maksym V. Kovalenko, and

Nicholas P. Stadie

ChemSusChem

Status of Manuscript:
☐ Prepared for submission to a peer-reviewed journal
☐ Officially submitted to a peer-reviewed journal
☐ Accepted by a peer-reviewed journal
☒ Published in a peer-reviewed journal

European Chemical Societies Publishing
Dual-Ion Batteries
10.1002/cssc.202201847

Abstract

Dual-ion hybrid capacitors (DIHCs) are a promising class of electrochemical energy storage devices intermediate between batteries and supercapacitors, exhibiting both high energy and power density and generalizable across wide chemistries beyond lithium. In this study, a model carbon framework material with a periodic structure containing exclusively 1.2 nm width pores, zeolite-templated carbon (ZTC), was investigated as the positive electrode for the storage of a range of anions relevant to DIHC chemistries. Screening experiments were carried out across 21 electrolyte compositions within a common stable potential window of 3.0-4.0 V vs. Li/Li^+ to determine trends in capacity as a function of anion and solvent properties. To achieve fast rate capability, a binary solvent balancing a high dielectric constant with a low viscosity and small molecular size was used; optimized full-cells based on $LiPF_6$ in binary electrolyte exhibited 146 Wh kg^{-1} and >4000 W kg^{-1} energy and power densities, respectively.

Introduction

Dual-ion batteries (DIBs) are a class of electrochemical energy storage devices that are under serious consideration for the replacement of lithium-ion batteries (LIBs) in specific applications, especially for stationary storage.[1] Such cells comprise a negative and positive electrode which undergo reversible insertion or intercalation of the cations and anions upon charging, respectively, which are initially present in the electrolyte. A possible benefit of DIBs over LIBs is their accommodation of diverse anions and cations beyond Li^+, where the latter is especially appealing for the future sustainability of battery production.[2] Graphite is commonly used as one or both electrodes in a DIB, where the latter case is often referred to as a dual-

graphite battery. Anion intercalation in graphite (e.g., by PF_6^-), which typically occurs at high potentials relative to metal plating and stripping reactions, has been shown to be effective for achieving high cell voltage (and therefore high energy density).[3] In all cases, a DIB functions in distinct contrast to a standard LIB wherein Li^+ ions shuttle back and forth from one electrode to the other (and the anion plays a relatively minor role in overall charge/discharge cycling), referred to as a rocking-chair charge storage mechanism.[4] Dual-ion hybrid capacitors (DIHCs) consist of a carbonaceous material at one of the electrodes that undergoes capacitive charge storage at its surface instead of faradaic intercalation. Such hybrid capacitors typically exhibit high rate capability and charge/discharge reversibility.[5] Porous carbon is an attractive alternative to graphite as a positive electrode material owing to a similarly high working potential and the ability to accommodate large anions.[6]

In a typical DIB, the bare cation and anion are reversibly inserted/intercalated at the negative and positive electrode, respectively, undergoing desolvation at each electrode/electrolyte interface.[7-9] However, it is also possible that one or both relevant ions is co-inserted along with the solvent, sometimes leading to irreversible insertion of just the solvent (as in pillared graphite intercalation compounds).[7,10-11] An example of such behavior is the co-intercalation of PF_6^- along with propylene carbonate (PC) which has been found to occur at high voltages (5.2 V vs. Li/Li^+) to form the stage-I compound $C_{24}PF_6(PC)_4$.[12-13] It has subsequently been determined that PF_6^- can be co-intercalated into graphite in much higher ion:solvent ratios, up to $1:0.7 \pm 0.2$ at the same plateau of 5.2 V using ethyl methyl carbonate (EMC) as the solvent.[13] At lower potentials, irreversible insertion of the solvent occurs during the first cycle co-insertion of PC and Li^+ into graphite at ~1.0 V vs. Li/Li^+, leading to the formation of a

pillared graphite electrode as well as the exfoliation of the graphite, which changes the potential at which all subsequent insertion/deinsertion occurs.[12] Hence, the use of a three-dimensionally connected graphene-like scaffold is an important candidate strategy toward preventing such issues.

Recently, numerous examples of DIHCs have been reported which explore combinations of metal plating/stripping reactions at the negative electrode with capacitive ion storage at high potentials at the positive electrode.[14] Several metals have been explored, including abundant, energy-dense elements such as sodium, magnesium, and aluminum.[15-16] The anions explored have varied across a wide range of weakly coordinating polyatomic species.[17] The solvent must be chosen to maximize the concentration of the salt since the energy density of a DIHC depends directly on the composition of the electrolyte.[18] Ionic liquids have also been explored, such as 1-butyl-1-methylpiperidinium bis(trifluoromethylsulfonyl)imide ($PP_{14}TFSI$) and N-butyl-N-methylpyrrolidinium bis(trifluoromethanesulfonyl)imide ($Pyr_{14}TFSI$).[6, 19] In general, such cells can achieve appreciable energy densities and power densities concurrently, and efforts are underway to improve anion capacity and to increase and flatten the potential of anion adsorption on the positive side. However, each study is typically a one-off (or side-by-side comparison) of a single (or a few) thoroughly investigated electrode-electrolyte system(s).

Zeolite-templated carbon (ZTC) is a class of ordered microporous carbon materials of interest for capacitive charge storage applications owing to its high surface area and dense network of three-dimensionally connected, electrically conductive channels.[20] The pores are isotropically connected owing to the high symmetry of the zeolite template in which the framework is formed; the repeat distance between pores is 14 Å and the N_2 accessible pore width

is ~12 Å, indicating that the molecular-sized channels are separated by atomistically thin carbon walls. Its three-dimensionally connected framework of graphene ribbon-like struts is locally disordered but exhibits long-range pore-to-pore ordering, uniquely enabling the construction of an accurate periodic model.[21] Upon systematic comparison of the numerous such models of ZTC to the experimental properties of the as-synthesized materials, it is possible to deduce that nearly ~80% of the volume of the bulk ZTC framework is accessible to small molecular adsorbates such as small molecular gases and ions.[22] This void volume is double that of highly porous zeolites (≤40%) and equivalent to highly porous metal-organic frameworks (e.g., 82% for MOF-177); i.e., no region of the material structure is off-limits to guests except its atomistically-thin graphene ribbon struts (see **Figure 1a**). Importantly, no part of the ZTC structure contains graphitic stacking and hence faradaic intercalation via staging is impermissible.

ZTCs have been investigated as the positive electrode material in several DIB/DIHC chemistries, including for chloroaluminate ($AlCl_4^-$/$Al_2Cl_7^-$/Cl^-) anion storage[23] and bis(fluorosulfonyl)imide (FSI^-) anion storage[24], as well as for divalent magnesium (Mg^{2+}) cation storage in a type of Mg-ion hybrid capacitor (MHC)[25]. The maximum reversible capacity observed (under varying conditions) in each cell type was 382, 141, and 113 mAh g^{-1}, respectively, which corresponds to 6.9, 2.6, and 1.0 ions per ZTC "supercage" (a rough estimation of the primary cavity within the pore network of ZTC, connected by four 12 Å pore entrances). Such cells were possible to cycle between 2.43 V, 3.60 V, and 2.01 V, all vs. Li/Li^+, respectively, permitting relatively high voltages and therefore high energy densities, both gravimetrically and volumetrically. The differences in ion size cannot account for the different ultimate capacities within each chemistry. Furthermore, none of these capacities seems to have

reached the maximum packing density of ions into the ZTC pore space, indicating that solvent is co-inserting along with the relevant ions during charge/discharge cycling. It is also clear that the type of solvent significantly effects the maximum ion capacity of ZTC.

Guiding principles for how to design DIBs and DIHCs where the solvent co-inserts with the anion of interest in the porous carbon electrode are needed. In this work, the solvent, anion, and electrochemical conditions are methodologically varied to understand the roles of ion shape and size, solvent shape and size, and viscosity and ionic conductivity of the electrolyte. Lithium was chosen as the counter ion for simplicity, and was not the focus of this study. A series of carbonate solvents was chosen since this type of solvent has the greatest issues associated with anion co-insertion. A simple protocol for down-selection of the electrolyte composition and voltage range of study was conceived, as shown in **Figure 1b**. Based on this approach, trends could be determined and used to draw conclusions regarding the optimal electrolyte to achieve high ion inclusion within the ZTC structure at different current rates and voltage windows. The optimal electrolyte for high power density was then optimized to demonstrate the utility of this approach in achieving useful cell formulations for applications.

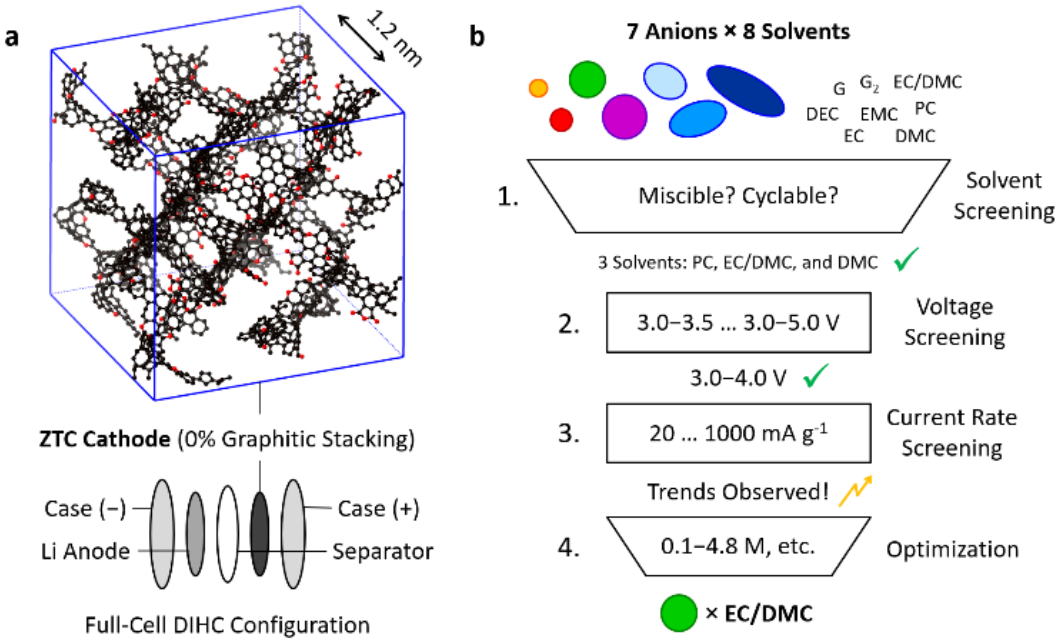

Figure 1. (a) Atomistic structural model of **FAU**-ZTC (Nishihara Model II+[20]), showing extremely high porosity (~80%) and no graphitic stacking, and the corresponding DIHC full-cell configuration. (b) Experimental protocol showing the field of anions and solvents screened herein, and subsequent down-selection of solvents and conditions for determining trends in capacitive ion storage in ZTC, leading to the final optimization of one anion/solvent pair.

Results and Discussion

Dual-Ion Electrochemistry

In a porous carbon/metal DIHC, the anion is inserted within the porous carbon positive electrode upon charge (while the cation plates at the bare metal negative electrode) and the opposite upon discharge. Hence, half-cell chemistry is the same as full-cell chemistry since the intended full-cell contains the bare metal as the negative electrode. The focus of the present study is to investigate insertion/deinsertion within the porous carbon framework, and interrogate the effects of anion size, solvent molecular size, and solvent properties on reversible storage capacity and rate capability. A purely microporous (12 Å pore width, without any graphitic stacking) carbon cathode material (ZTC) was used without any binder or additive (the effects of

a PTFE binder are shown in the Supporting Information). All studies were performed with Li metal as the negative electrode, and hence Li^+ as the counterion. Upon charging, the relevant reactions are as follows:

$$\text{Negative Electrode:} \qquad Li^+ + e^- \rightarrow Li \qquad (1)$$

$$\text{Positive Electrode (ZTC):} \qquad x\,C + A^- \rightarrow [A]C_x + e^- \qquad (2)$$

The charging process ends when either all of the Li^+ cations or all of the relevant anions are depleted in the electrolyte (and therefore plated at the negative electrode or stored within the pore network of ZTC) or when the ZTC reaches its maximum anion storage capacity. A large excess of electrolyte is used in this work to prevent the former scenario. Contrary to LIBs, the OCV of a DIHC depends on the electrolyte and the chemical potentials of its substituents, as described by the Nernst equation:

$$-e\,V = \mu^{\circ}_{Li} + \mu^{\circ}_{A} - \mu^{\circ}_{Li^+} - \mu^{\circ}_{A^-} - 2\,k_B T \ln[Li^+] \qquad (3)$$

In this equation, $\mu^{\circ}_{Li^+}$ and $\mu^{\circ}_{A^-}$ are the chemical potentials of the cation and anion in solution, μ°_{Li} is the chemical potential of the Li atoms in the metal, and μ°_{A} is the chemical potential of the anions inserted into ZTC upon charging.[7] This means that the OCV of a DIHC will depend on the identity of both the anion and the solvent. The OCV of the cell compositions explored in this work varied between 2.8-3.4 V vs. Li/Li^+ (see Tables S2-S3).

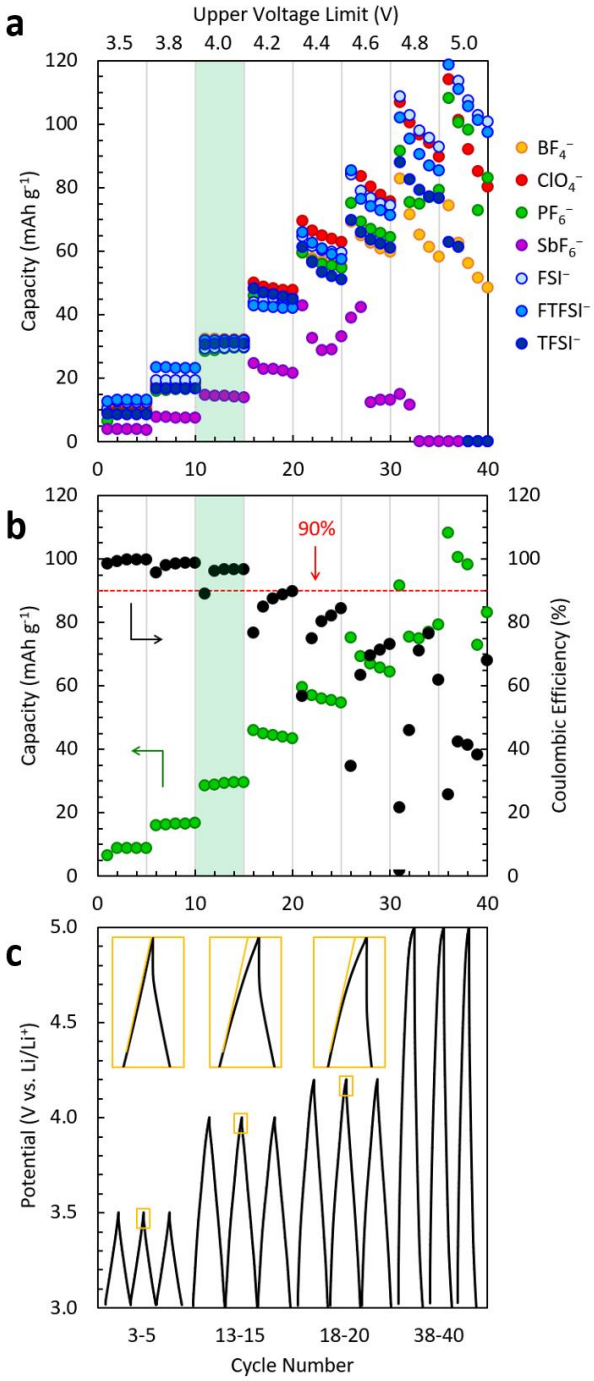

Figure 2. Voltage opening electrochemical characterization of ZTC DIHCs cycled at 100 mA g^{-1}. (a) Potential window screening (3.0-3.5…5.0 V) of all anions in EC/DMC, showing discharge capacity (colored symbols) at 100 mA g^{-1}. (b) Representative potential window screening for PF_6^- in EC/DMC , showing discharge capacity (green symbols) and coulombic efficiency (black symbols) at 100 mA g^{-1}. (c) Representative three-cycle galvanostatic charge/discharge profiles for PF_6^- in EC/DMC between: 3.0-3.5 V, 3.0-4.0 V, 3.0-4.6 V, and 3.0-5.0 V, as a function of cycle number.

Electrochemical Protocols

The electrochemical focus of this research is two-fold: to establish common reversibility limits with respect to the electrochemical stability window of ZTC within a diverse assortment of electrolytes and, thereafter, to study the effects that anion and solvent properties have on capacity and current rate within a stable cycling regime. Stepwise opening of the potential window of charge/discharge cycling (in 5 cycle intervals) as well as cyclic voltammetry revealed the extent of oxidation at the ZTC electrode and other side reactions. Based on this information, an appropriate window was chosen for further current rate dependency experiments within the range of 20 to 1000 mA g^{-1}. This method of down-selection of electrolyte compositions and operation parameters is shown schematically in Figure 1b.

Three solvents (DMC, EC/DMC, and PC) and seven different anions (ClO_4^-, BF_4^-, PF_6^-, SbF_6^-, FSI^-, $FTFSI^-$, and $TFSI^-$), a total of 21 electrolytes, were studied. Solvents composed of DEC, glyme, and diglyme either never achieved a capacity above 1 mAh g^{-1} or became too viscous to operate at the desired 1 M concentration, and were therefore disregarded. The anions consist of two distinct types: spherical oxo- or fluoro-anions (ClO_4^-, BF_4^-, PF_6^-, and SbF_6^-) and spheroidal fluorosulfonylimide anions (FSI^-, $FTFSI^-$, and $TFSI^-$). Perchlorate, ClO_4^-, while spherical, is an outlier within that series due to its low oxidative stability/potential and high HOMO energy.[33]

Potential Window Studies

To achieve cycling stability in a DIHC, the cathodic and anodic potentials must be between the HOMO and LUMO of the electrolyte.[34] If the Fermi level of the cathode is located below the HOMO of the electrolyte, oxidation of the electrolyte occurs (unless the reaction is

blocked by an SEI layer). On the other hand, if the Fermi level of the anode is located above the LUMO of the electrolyte, then the electrolyte will be reduced. The SEI layer, though mainly formed in the first charge cycle, continues to thicken in each subsequent charge cycle; as this decomposition occurs, Li^+ cations, anions, and solvent are depleted, one potential cause of capacity fading.[35] The OCV is the difference between the Fermi levels of the electrodes and, in order to maximize the energy density of a cell, this difference must be maximized without exceeding the window afforded by the electrolyte stability. The anion often sets the oxidation limit of the electrolyte[33] whereas solvent properties (dielectric constant, molecular size, viscosity, etc.) play an important role in ionic conductivity.[36-37]

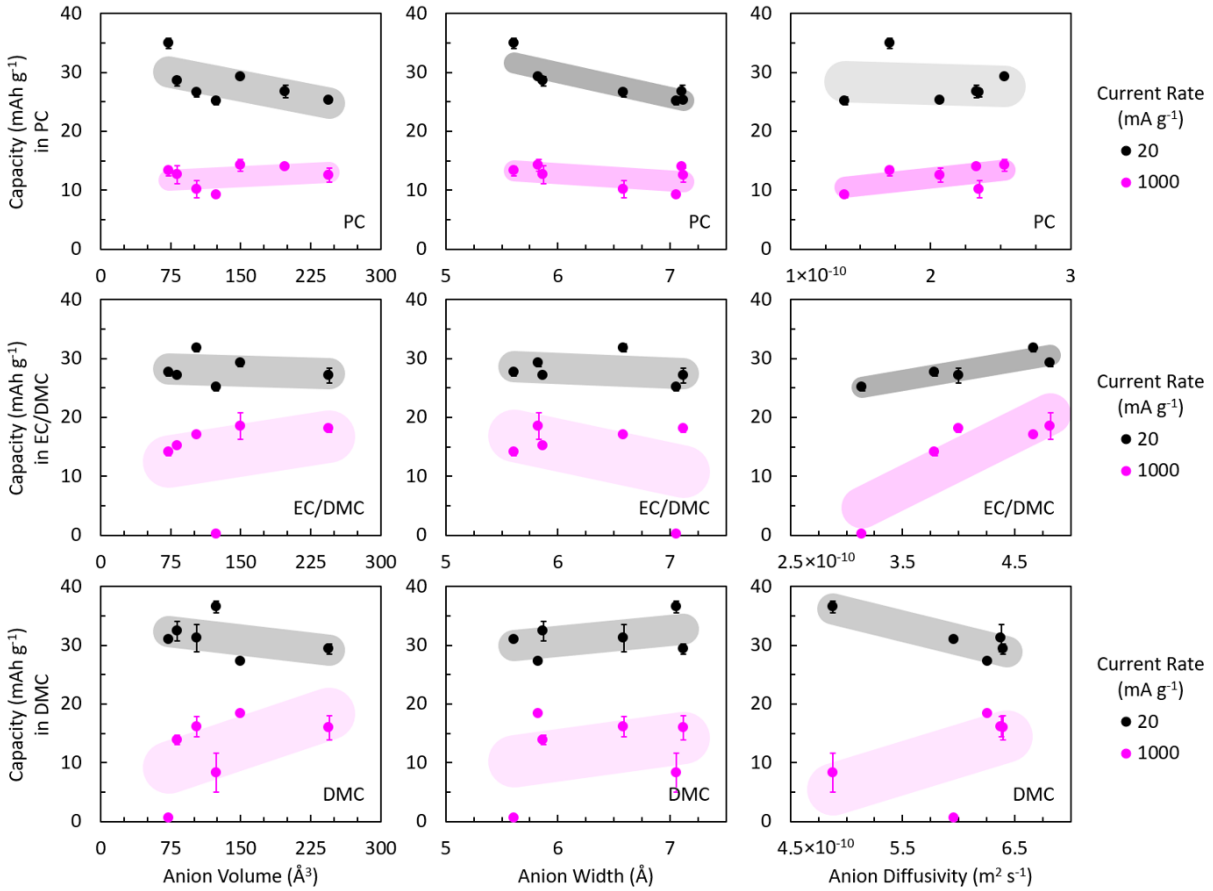

Figure 3. Anion storage capacity in ZTC as a function of anion volume, narrowest width, and diffusivity, from reversible discharge capacity between 3.0-4.0 V vs. Li/Li+. Low current rate data (20 mA g-1) are shown in black and high current rate data (1 A g-1) are shown in pink. Stronger correlations are indicated by heavier and narrower (linear) trend lines, as a guide for the eye. Error bars are across measurements in triplicate or more.

To establish the stable potential window for later rate capability tests, each cell was cycled 40 times at the benchmark current rate established in previous work (100 mA g^{-1}),[24] widening the voltage window every 5 cycles, thereby exploring 8 different voltage ranges of interest (from 3.0-3.5 to 3.0-5.0 V vs. Li/Li^+). In this way, the voltage limit beyond which degradation occurs due to oxidative side reactions at the ZTC electrode could be identified. The results for all anions in EC/DMC are shown in Figure 2a, and representative results for PF_6^- in EC/DMC are shown in Figure 2b. In $LiPF_6$ in EC/DMC, ZTC showed a steady increase in

discharge capacity with increasing maximum voltage, up to the widest potential window explored (3.0-5.0 V). This electrolyte showed five consecutive cycles of coulombic efficiencies exceeding 90% up to the 3.0-4.2 V potential window (Figure 2a). A plateauing feature at the top of the charge step in a voltage profile indicates decomposition of the electrolyte; for example, 1 M $LiPF_6$ in EC/DMC begins to show such decomposition at >4.2 V vs. Li/Li^+ (Figure 2c).

Across all of the 21 electrolyte combinations explored in stepwise potential opening studies, between 0.1-0.6 anions could be reversibly inserted into each ZTC supercage (defined as described in the Supporting Information) within the 3.0-4.0 V range, suggesting that general conclusions could be made about the role of anion size/shape and solvent molecular size/character on current rate dependencies in that range (Figures S1a-S1c). Therefore, the 3.0-4.0 V voltage window was chosen for further trend analysis due to consistent coulombic efficiencies above 90%. Higher capacities within wider overall voltage windows were observed for $LiPF_6$ in EC/DMC and therefore that system was later chosen for further optimization.

Current Rate Studies

A wide range of electrolyte compositions were explored to determine the role of the previously mentioned electrolyte properties on specific capacity at current rates up to 1 A g^{-1}. Cells containing each of the 21 electrolyte combinations (at 1 M concentration) were subjected to an increasing current rate protocol (20, 50, 100, 200, 500, and 1000 mA g^{-1}) within the aforementioned common voltage window of 3.0-4.0 V vs. Li/Li^+ (Figures S2a-S2c). As expected, the capacities of all cells were inversely correlated with current rate. The experimental results reveal that anion/solvent size and solvent viscosity/dielectrics have subtle but important effects on specific capacity, current rate dependence, and voltage window stability. The structural and

electrochemical properties of the anions and solvents used are shown in Table 1, and a summary of the results of the broad electrochemical screening experiments is presented in Figure 3. A discussion of some of the important trends in these data is given in the next several sections.

Type	Anion	Volume (Å^3)	Narrowest Width (Å)	Length (Å)	Diameter[a] (Å)	OS[b] [33] (V vs. Li/Li$^+$)	OS[b] [38] (V vs. Li/Li$^+$)
Spherical	BF_4^-	73	5.61	5.66	5.19	6.35	6.01
	ClO_4^-	82	5.87	5.90	5.39	4.36	3.87
	PF_6^-	103	6.59	6.60	5.82	8.57	6.51
	SbF_6^-	124	7.06	7.12	6.19	NR	NR
Spheroidal	FSI^-	150	5.83	8.40	6.59	5.34	4.19
	$FTFSI^-$	198	7.11	9.43	7.23	NR	NR
	$TFSI^-$	245	7.12	10.34	7.76	6.12	4.48

Table 1. Structural and electrochemical properties of anions in this study. [a] Diameter of a sphere with the same volume. [b] Oxidative stability. NR – not reported.

Anion Size Effects

At low current rates, equilibrium is effectively reached and the maximum number of anions are stored, regardless of the electrolyte composition. Accordingly, the maximum reversible capacity generally decreases as a function of anion volume at 20 mA g^{-1} (Figure 3, black series). The smallest anion studied, BF_4^-, exhibits the highest capacity in the screening tests (35 mAh g^{-1}, or 0.63 anions per supercage, in PC). Likewise, the largest anion studied,

$TFSI^-$, exhibits the lowest capacity (25 mAh g^{-1}, or 0.46 anions per supercage, in PC). The maximum capacities at each current rate among the different anions are surprisingly similar. Hence, the overall volume occupied by the anions within the ZTC supercages is higher for the larger anions; this indicates that occupancy within the pores is less limited by a "pore filling" mechanism and rather more limited by a "monolayer adsorption" mechanism (i.e., limited by a fixed number of adsorption sites) and strongly reveals solvated anion insertion. The narrowest width is typically more correlated to capacity than the anion volume, which also indicates a "monolayer adsorption" type model as opposed to "pore filling." At high current rates (Figure 3, pink series), anion size shows significantly less correlation (except in PC, where the capacity is effectively the same for all anions) and capacity is therefore better attributed to other factors.

Anion Diffusion Effects

The diffusivity of each anion in each solvent was measured using pulsed-field gradient NMR analysis (see Table 2). Efforts to perform ^{35}Cl NMR were unsuccessful and therefore ClO_4^- was excluded from this comparison. In general, anion diffusivity was inversely correlated with both viscosity and dielectric constant among the three solvents explored (see Figure S3). Hence, diffusivity was found to be more significantly a property of the solvent rather than the anion. Since diffusivity is expected to play an important role at high current rates, the capacity of all anions as a function of diffusivity at the maximum current rate explored (1 A g^{-1}) is shown in Figure 4.

The spherically shaped anions did not show a correlation between diffusivity and width in any solvent, which suggests that the higher electronegativity of phosphorous played a key role in its diffusivity (see Figure 4a). In EC/DMC and PC, the spheroidal shaped ions showed a

negative correlation between diffusivity and width. The solvent that gave rise to the largest differences in diffusivity of the anions (within the same solvent) was EC/DMC, and this solvent system is therefore best representative of anion diffusivity effects. In EC/DMC, there is a strong correlation between diffusivity and capacity, as shown in Figure 3. This is consistent with the general trend observed for all solvent systems in Figure 4, thus confirming the importance of anion diffusivity for high current rate storage within the nanometer-sized channels of ZTC. In EC/DMC, the cations and anions are more closely paired and therefore diffusion takes priority over anion size in determining anion capacity.

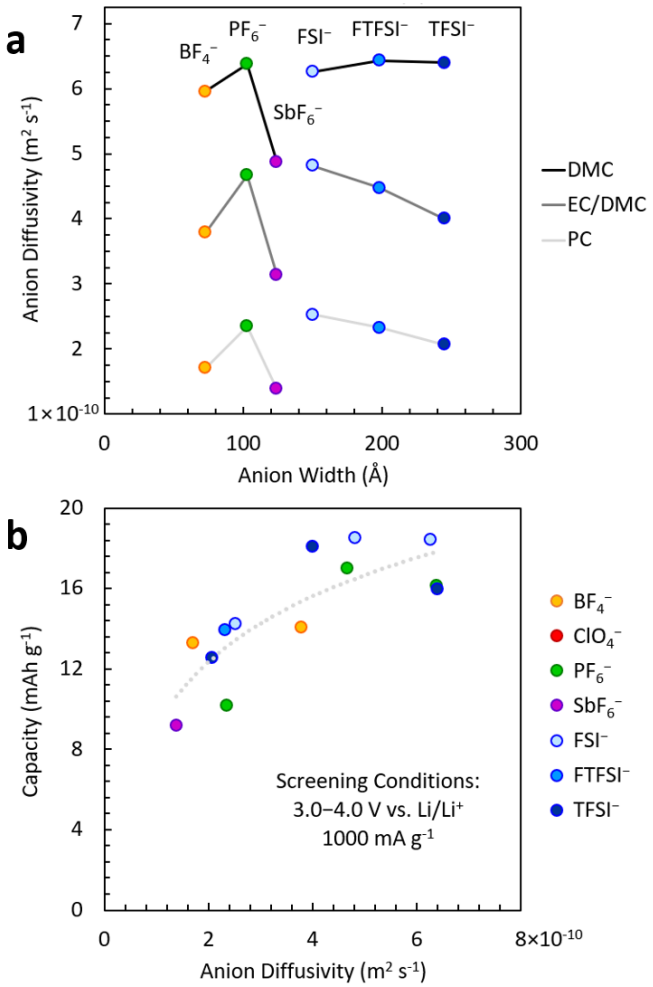

Figure 4. (a) Anion diffusivity as a function of anion volume in each of the solvents in this study: DMC, EC/DMC, and PC. (b) Anion storage capacity in ZTC as a function of anion diffusivity across all solvents, from reversible discharge capacity at 1 A g^{-1} between 3.0-4.0 V vs. Li/Li^+.

Solvent Size Effects

The three solvents chosen for analysis in this study also display a range of physicochemical properties, permitting an assessment of the role of the solvent in anion storage in ZTC-based DIHCs. Anion capacity as a function of solvent molecular size is shown across all anions in **Figure 5**. It is clear that solvent molecular size is not the main dictating property of anion capacity in ZTC, neither at low nor at high current rates. Solvation structure influences several aspects of anion insertion, including diffusion as well as volume and shape occupied by

the anion within the ZTC pores; the identity of the solvent also affects the structure of the passivation layer formed at the electrode interface (cathodic electrolyte interphase, CEI).[14,37] Solvents with a high dielectric constant provide good solubility of the electrolyte salt, but also bring about high viscosity which slows ion transport. Solvents with a low dielectric constant provide fast ion transport but also increased ion-pairing effects between Li^+ and the anion due to their low solubility.[13] Therefore, solvent mixtures comprising components with different individual properties are often chosen to provide an effective compromise within this trade-off. A more detailed comparison of the properties of the three solvents chosen in this work is given in Table S5.

Type	Anion	DMC	EC/DMC	PC
Spherical	BF_4^-	5.96	3.79	1.71
	PF_6^-	6.38	4.67	2.35
	SbF_6^-	4.88	3.14	1.39
Spheroidal	FSI^-	6.26	4.82	2.53
	$FTFSI^-$	6.43	4.48	2.33
	$TFSI^-$	6.40	4.00	2.07

Table 2. Anion diffusivity (in 10^{-10} m^2 s^{-1}) in each of the solvents in this study: DMC, EC/DMC, and PC.

Solvation Structure Effects

To better understand the complex role of solvation structure on anion capacity in ZTC, the smallest (BF_4^-) and the largest ($TFSI^-$) anions were chosen for further analysis (Figure 6). It has been shown that the binding energy of the Li-BF_4 pair is slightly higher than the Li-TFSI pair, with binding distances of 1.91 Å and 2.00 Å respectively.[39] At low current rates, smaller and more electronegative anions such as BF_4^- benefit from a highly polar solvent that reduces ion pairing. For example, the highest capacity reported in this work's initial screening studies

(32.5 mAh g^{-1}, at 20 mA g^{-1}) corresponds to the storage of BF_4^- solvated by PC. On the other hand, large anions such as $TFSI^-$ dissociate more readily due the more delocalized charge over the entire molecule. Hence, $TFSI^-$ benefits from a low viscosity solvent that enhances ion mobility, even at low current rates. At high current rates, both BF_4^- and $TFSI^-$ show their highest capacities in EC/DMC, suggesting that the high dielectric constant of EC and the low viscosity of DMC permit a synergy of properties accommodating both types of anions. It is possible that anions in EC/DMC preferentially insert under solvation by EC (leaving the DMC molecules in solution), serving to maintain a low viscosity (high ion mobility) electrolyte; further studies are warranted to assess the role of stored ion solvation in binary solvent electrolytes. Nevertheless, the results obtained herein generally support the strategy of employing a binary solvent system to exploit the trade-off between solubility and ion mobility. [13,38]

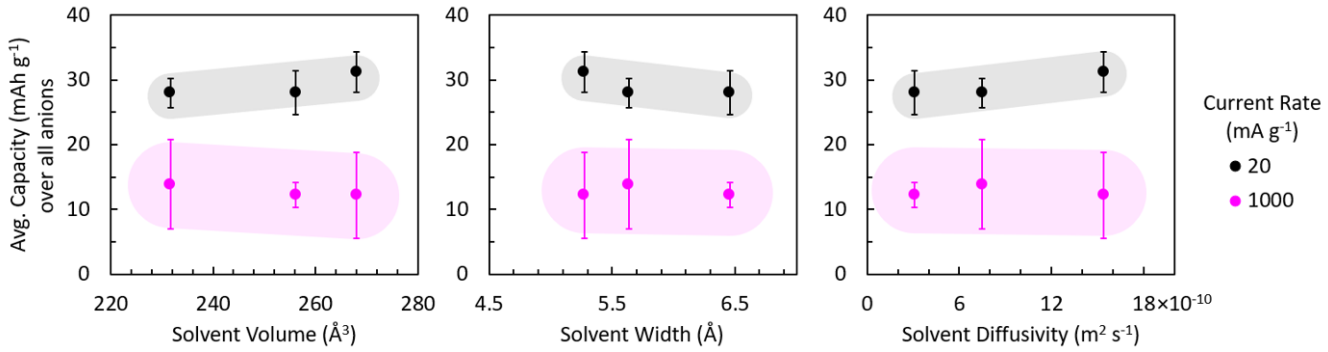

Figure 5. Average anion storage capacity in ZTC as a function of solvent diameter, narrowest width, and diffusivity from reversible discharge capacity between 3.0-4.0 V vs. Li/Li^+. Low current rate data (20 mA g^{-1}) are shown in black and high current rate data (1 A g^{-1}) are shown in pink. Error bars are standard deviations across all anions, tested in triplicate.

Optimization Studies

The screening studies across many electrolyte compositions were performed in the common stability range of 3.0-4.0 V vs. Li/Li^+ and with 1 M nominal concentrations to permit a

controlled analysis of the effects of anion and solvent properties. In these experiments, less than 1 anion per ZTC supercage was observed to be inserted even at the slowest current rates explored, far lower than the maximum expectable capacity on the basis of complete pore filling by bare anions. For example, we estimate that 2.7 PF_6^- ions per supercage can be inserted into the pore volume of ZTC (probe accessible volume per unit cell: 17,605 $Å^3$, total volume per unit cell: 111,563 $Å^3$, for Nishihara Model II+). While such estimates do not consider the role of solvent nor the effect of anion-anion repulsion, they indicate that higher capacities would be achievable under optimized conditions.

Owing to its high capacity at low current rates, good oxidative stability at >4.0 V vs. Li/Li^+, and admirable rate capability at up to 1 A g^{-1}, further optimization studies were focused on PF_6^- in EC/DMC as the model electrolyte. Cyclic voltammetry was first performed within incrementally increasing potential windows to establish the maximum stable window in which electrolyte and/or ZTC decomposition could be avoided. This window was determined to be between 2.5-4.6 V vs. Li/Li^+ (Figure S4). A concentration series was analyzed that consisted of 0.1, 1.0, 2.0, 3.0, and 4.8 M electrolyte solutions. In this study, a maximum capacity of 128.9 mAh g^{-1} was achieved between 2.5-4.6 V vs. Li/Li^+ in 3.0M $LiPF_6$ in EC/DMC at 100 mA g^{-1}, corresponding to ~2.3 anions per ZTC supercage (Figure 7). This is slightly shy of the theoretical limit described above which suggests that further optimization could perhaps improve capacity.

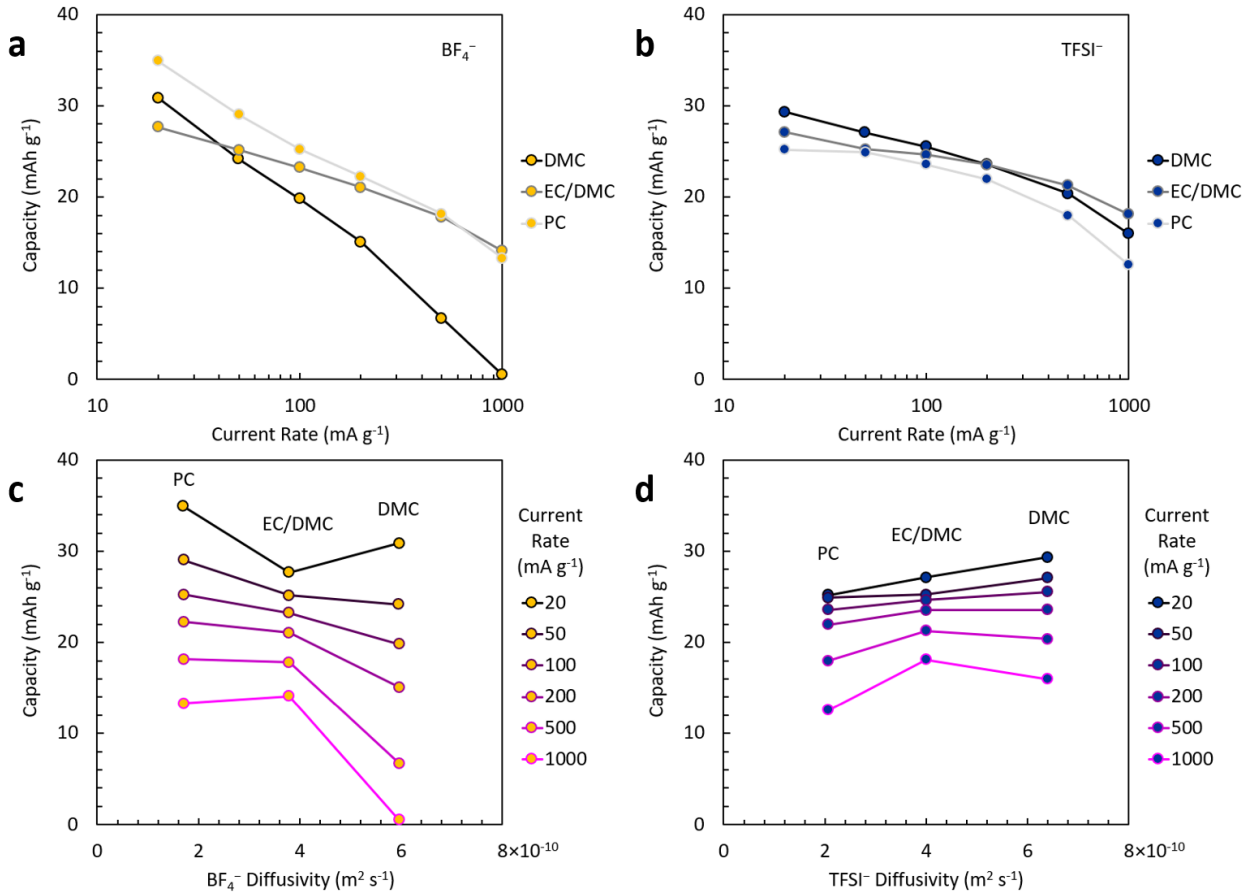

Figure 6. Anion storage capacity as a function of (a, b) current rate (mA g^{-1}) and (c, d) anion diffusivity, for (a, c) BF_4^- and (b, d) $TFSI^-$ cycled between 3.0-4.0 V vs. Li/Li^+.

Several effects on the anion capacity can be observed upon varying the concentration of the electrolyte. The concentration of $LiPF_6$ in EC/DMC was positively correlated to discharge capacity at low current rates, but negatively correlated at high current rates for all concentrations except 0.1 M (Figure 7a). In other words, while high concentration (e.g., 4.8 M) improves capacity at low current rates, the capacity is subject to extreme reduction upon increasing the current rate, an effect that can be attributed to increased viscosity and slow diffusion. The diffusivity as measured by PFGSTE NMR experiments corroborates this explanation (as shown by the pink trace for 2 A g^{-1} in Figure 7c). Evidence for increased ion pairing with concentration

is also observed in that the Li^+ and PF_6^- diffusion rates converge at high concentrations. The slightly higher deviation of the capacities at 0.1 M compared to 1.0 M can be attributed to a decrease in ionic conductivity caused by a low concentration of charge carries, even though the diffusivity is the highest.

Cyclic voltammetry and Randles-Ševčík analysis of PF_6^- storage within ZTC showed exclusively capacitive behavior within the common stability window chosen for comparison to all other anions (3.0-4.0 V vs. Li/Li^+). Upon widening the voltage window to between 2.5-4.6 V vs Li/Li^+, charge storage adopted a more Faradaic character (Figure S6), suggesting that the anions are adsorbed within more confined regions of the ZTC supercages that encourage more charge transfer than when stored under lower density conditions (Figure S6). Self-discharge analysis revealed that some leakage occurs even from within these confined regions of the ZTC pores (Figure S10), a common issue facing DIHC electrodes. Interestingly, after 100 cycles at 100 mA^{-1}, electrolytes of all concentrations explored converged on the same capacity of ~110 mAh g^{-1} or ~2.0 ions per supercage. This indicates a seeming equilibrium capacity of ZTC toward PF_6^- that is reversible across a wide range of electrolyte compositions at the benchmark current rate. To better understand this capacity, a comparison can be drawn to PF_6^- storage in graphite; the maximum intercalation capacity in graphite corresponds to a stage-1 compound of composition PF_6C_{24}.[12,13] Hence, in graphite, the minimum in-plane PF_6-PF_6 distance is ~8.5 Å. In ZTC, this distance is reduced to (on average) ~6 Å given the accessible pore width of 12 Å. Likewise, the composition is slightly more enriched with anions on a per-carbon basis, corresponding to a maximum of ~PF_6C_{18} for ZTC (without regard for the hydrogen or oxygen content). Nevertheless, it is expectable that anion-anion repulsion, in addition to steric hindrance

of the included solvent, is responsible for determining the maximum upper capacity within the ZTC framework.[40]

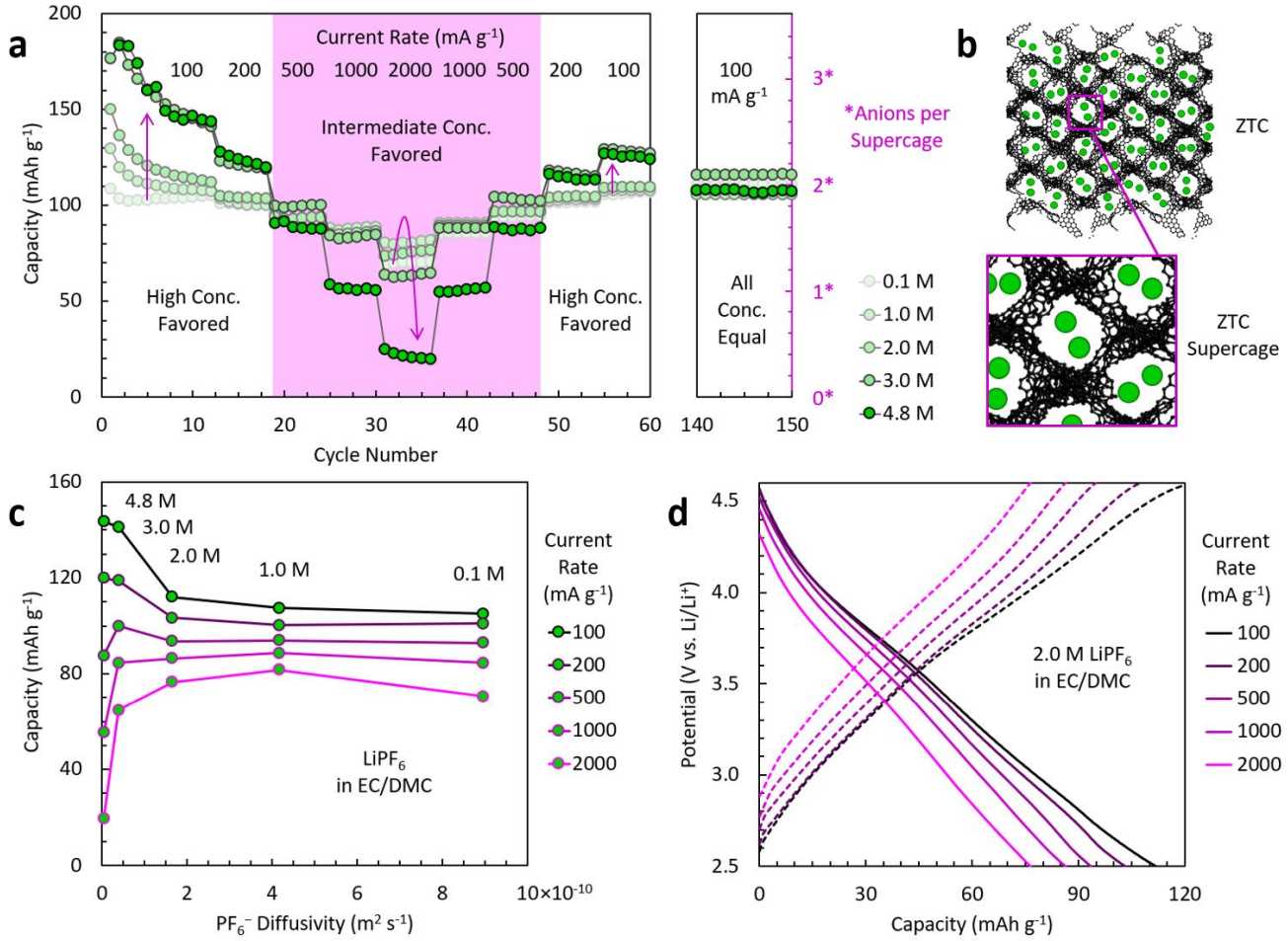

Figure 7. Concentration series of PF_6^- in EC/DMC cycled from 2.5-4.6 V vs Li/Li^+ and from 100 mA g^{-1} to 2000 mA g^{-1} in units of (a) discharge capacity (in mAh g^{-1}) and/or ions per supercage as a function of cycle number and (c) discharge capacity as a function of diffusion coefficient (in 10^{-10} m^2 s^{-1}). (b) Schematic depiction of long-cycling anion capacity of PF_6^- in ZTC and (d) representative voltage profiles for 2.0 M $LiPF_6$ in EC/DMC. Note: the concentration is given as the nominal (initial) concentration prior to dissolution.

Conclusions

Zeolite-templated carbon (ZTC) serves as an ideal model material for understanding the mechanism of anion storage in nanometer-sized carbon pore spaces because of its ordered framework of 1.2 nm pores that is robust to charge and discharge at potentials relevant to use as a positive electrode in DIHCs. The methodological variation of anions and solvents has been employed herein to elucidate guiding principles for the roles of anion and solvent molecular size, shape, and other properties (such as diffusivity) on storage capacity, at both the low and high current rate extremes. Full-cells based on a ZTC cathode and electroplating/stripping of lithium metal at the negative electrode demonstrate specific energies of 146 Wh kg^{-1} and power densities of >4000 W kg^{-1} which are realistic values for studying the effects of electrolyte properties. Solvation structure upon charging is difficult to study due to the rigid nature of ZTC and therefore future work analyzing binary and tertiary solvent systems will help to understand the effects of ion pairing. Electrolyte composition is a key part of battery and capacitor design and the fundamental understanding of how these molecules interact within such systems provides insights towards optimization.

Experimental

Materials Synthesis

ZTC was prepared according to the established two-step method[26-27], via liquid impregnation of zeolite NaY with furfuryl alcohol at room temperature and then chemical vapor deposition of propylene at 700 °C; after heat treatment at 900 °C, the zeolite template was

removed upon repeated dissolution in aqueous HF. The synthesis methods are described in detail in the Supporting Information.

Materials Characterization

Powder X-ray diffraction (XRD) measurements were performed using a Bruker D8 Advance diffractometer with Cu $K\alpha_{1,2}$ radiation (λ = 1.54 Å) in reflection geometry. Nitrogen adsorption/desorption isotherms were measured at 77 K between 10^{-4}-100 kPa using an automated volumetric instrument (3Flex, Micromeritics Instrument Corp.). Specific surface areas were calculated by the Brunauer-Emmett-Teller (BET) method between $P/P_0 = 4\times10^{-6}$-0.11 and micropore volumes were calculated by the Dubinin-Radushkevich (DR) method.[28] Pore-size distributions were determined by non-localized density functional theory (NLDFT) calculations with a carbon slit-pore model (using MicroActive Share software, Micromeritics Instrument Corp.).

Electrochemical Cell Materials

The following materials were used in the preparation of electrochemical cells: ethylene carbonate (EC, battery grade, BASF), dimethyl carbonate (DMC, battery grade, BASF), propylene carbonate (PC, 99.7%, Sigma Aldrich), lithium perchlorate ($LiClO_4$, 99,9%, ABCR), lithium tetrafluoroborate ($LiBF_4$, 99%, Acros), lithium hexafluorophosphate ($LiPF_6$, 99%, Novolyte), lithium hexafluoroantimonate ($LiSbF_6$, 99%, Apollo), lithium bis(fluorosulfonyl)imide (LiFSI, 99%, Henan Tianfu Chemical Co.), lithium (fluorosulfonyl)(trifluoromethanesulfonyl)imide (LiFTFSI, 99.7%, Provisco), lithium bis(trifluoromethanesulfonyl)imide (LiTFSI, 99%, Acros), lithium foil (Li, 99%, Fluka), and glass microfiber discs (0.67 × 257 mm, GF/D grade, 1823-257, Whatman).

Electrolyte Preparation

The electrolyte was prepared by slowly mixing the given lithium salt/solvent combinations at the specified concentrations (see Supporting Information, Tables S1-S2) under inert Ar atmosphere (< 0.1 ppm H_2O/O_2). A dual solvent electrolyte (EC/DMC) was prepared at a 1:1 ratio, by weight. In all cases, an exothermic reaction takes place upon dissolution of the salt, resulting in the eventual formation of a viscous, transparent liquid. The electrolyte concentration reported is the nominal concentration based on the initial volume of the solvent, not the final volume. The actual (final) concentrations corresponding to each nominal concentration in the $LiPF_6$ in EC/DMC series are shown in Table S2.

Current Collector Coating To improve cycling stability under high-voltage conditions, the stainless steel coin cell caps (316L, 2032 size, Hohsen Corp.) were coated at the positive electrode side with TiN by pulsed DC magnetron sputtering using a titanium target under a flowing Ar/N_2 atmosphere at a pressure of 0.5 Pa, as previously described.[29-30] The sides of the current collectors, parallel to the sputtering beam and thus less coated by TiN, were further protected with a thin layer of epoxy glue (Araldite Rapid).

Electrochemical Cell Preparation

Stainless-steel coin cells were assembled in a glovebox under inert Ar atmosphere (<0.1 ppm H_2O/O_2). The active electrode material (ZTC), simply as a dry, activated powder, was homogeneously dispersed on the TiN-coated stainless-steel cap. In general, the use of a binder results in poorer accessibility of the porous electrode; these effects are described in the Supporting Information. A single glass microfiber disc was then placed on top of the bare ZTC powder as the separator, and saturated with 250 μL electrolyte. A thin lithium film (~60 mg)

pressed onto a stainless-steel disc was placed on top of the separator and was used as both the reference and counter electrodes. A stainless-steel spring and cell bottom were placed on top of the reference electrode and compressed with a hydraulic press. The working electrode was prepared as a loose powder without the use of any binder, conductive additive, or solvent, and the electrolyte was used as prepared above. Each cell contained a 0.9-1.3 mg loading of active cathode material (ZTC).

Electrochemical Measurements

Before galvanostatic cycling, the prepared cells were held at open circuit voltage (OCV) for 2 hours to allow the ZTC electrode to become fully wetted with electrolyte. The OCV of the cells was between 2.8-3.4 V vs. Li/Li^+. Galvanostatic cycling was performed using a multi-channel workstation (CT2001A, 0.005-1 mA, Landt Corp.). The measured specific discharge capacity (number of ions deinserted) was normalized by the total initial mass of the active material (since no binder or conductive additive were used). Cyclic voltammetry was performed using a separate multi-channel workstation (MPG-2, BioLogic SAS).

NMR Spectroscopy

The diffusivity and ionic conductivity of each species in each electrolyte was determined using multinuclear (^1H, ^7Li, and ^{19}F) NMR spectroscopy. A 200 μL aliquot of each as-prepared electrolyte was subjected to a pulsed-field gradient stimulated echo (PFGSTE) pulse sequence using a 500 MHz NMR spectrometer (Ascend 500, Bruker Corp.) equipped with an Avance III HD console (Bruker Corp.), an automatic sample loading system (SampleJet, Bruker Corp.), and a 5 mm liquid nitrogen-cooled broadband (BBO) cryoprobe (Prodigy, Bruker Corp.). Spectra were acquired using the ledbpgp2s pulse sequence (Bruker Corp.), and t2×t1 matrices of

16384×20 points (for ^{1}H) or 131072×20 points (for ^{7}Li and ^{19}F) were collected. The z-axis gradient strength varied linearly from 2% to 98% of its maximum value (65.7 G cm^{-1}), the gradient pulse duration was 2.8 ms (for ^{1}H and ^{19}F) or 4.8 ms (for ^{7}Li), and the time period between the two gradient pulses was 50 ms (for ^{1}H and ^{19}F) or 100 ms (^{7}Li). The relaxation delay (D1) ranged between 3-10 s. All measurements were performed at a constant temperature of 300 K and the results were analyzed using a dedicated software package (Topspin v3.6, Bruker Corp.). Self-diffusion coefficients (referred to herein as diffusivity, D) were determined by fitting the NMR intensity as a function of time to the Stejskal-Tanner equation.[41]

Anion Capacity Metrics

Reversible charge/discharge capacity (in mAh g^{-1}) was converted into "number of ions per supercage" of the ZTC framework on the basis of the number of “supercages” per unit mass of ZTC. The number of ZTC supercages per gram was determined based on a periodic model of ZTC referred to herein as Nishihara Model II+;[21] 64 “supercages” (pore spaces of roughly the same size and shape), corresponding to 64 tetrahedral nodes in the original faujasite (**FAU**) zeolite template in which it was formed, exist within the cubic unit cell weighing 0.4626 g mL^{-1} (corresponding to a 2×2×2 supercell of unit cells of the faujasite template, a = 48.14 Å). An example calculation of ions per supercell, n, is given in the Supporting Information. In brief, a capacity of 55 mAh g^{-1} corresponds to 1 anion adsorbed within each supercage of the **FAU**-ZTC framework.

Computational Methods

Theoretical calculations of molecular size and shape were performed using density functional theory (DFT). A global hybrid functional (MN15) together with a triple-zeta basis set

(6-311++G**) was chosen based on recent methods employed in our group[31] and general benchmarking studies[32] and implemented using the Gaussian 16 software package. The size of each anion in solution was estimated by optimizing the anion within a polarizable continuum model. To establish the solvent environment for anion calculations, a unique polarizable continuum was generated for each solvent using the solvent radius, dielectric constant, index of refraction, and macroscopic surface tension (see Supporting Information). Each anion was then optimized in the polarizable continuum, resulting in a solvent excluded surface solvation cavity. The length and width of the solvation cavity were defined as the longest distance between two points on the solvation cavity, and the longest distance between two points perpendicular to the length, respectively. The convex hull of the solvent excluded surface solvation cavity was then calculated to determine the effective volume of each anion. The size of each solvent was estimated by optimizing the solvent molecule alone.

Associated Content

Acknowledgments

We thank Wei Xu for insightful discussions. C.W. and N.P.S. are grateful for funding provided by the National Science Foundation (grant OIA-2034110). P.V., K.V.K., and M.V.K. gratefully acknowledge financial support provided by Empa (internal project “GRAPHION”). We also thank the MSU NMR Center (supported by National Science Foundation grant DBI-1532078 and the M. J. Murdock Charitable Trust grant 2015066:MNL) for access to their instrumentation and Brian Tripet for assistance in performing the measurements and analysis.

Supporting Information

Electrolyte Compositions: The electrolyte compositions explored in this work are shown in Tables S1-S2. Note that the concentration is described according to the initial solution volume, not the final solution volume after dissolution, and is hence only an approximation of actual electrolyte concentration. The molality remains precisely defined before and after dissolution.

Salt	Solvent	Salt Mass (g)	Solvent Mass (g)	Initial Molarity (mol L^{-1})	Molality (mol g^{-1})
$LiClO_4$	DMC	0.2171	2.0821	1.05	11.1
	EC/DMC	0.1064	1.0612	1.11	10.7
	PC	0.1073	1.2472	0.97	9.2
$LiBF_4$	DMC	0.1877	2.1355	1.00	8.2
	EC/DMC	0.0987	0.0983	1.25	94.1
	PC	0.0963	1.2375	1.00	7.3
$LiPF_6$	DMC	0.3049	2.0939	1.03	22.1
	EC/DMC	0.0924	0.6302	1.15	22.3
	PC	0.1525	1.2876	0.93	18.0
$LiSbF_6$	DMC	0.2435	1.0762	1.00	54.9
	EC/DMC	0.2434	1.1799	1.00	50.1
	PC	0.2830	1.2183	1.01	56.4
LiTFSI	DMC	0.2854	1.0251	0.96	79.9
	EC/DMC	0.2868	1.2245	0.96	67.2
	PC	0.2850	1.2073	1.02	67.8
LiFTFSI	DMC	0.2413	1.0975	0.99	52.1
	EC/DMC	0.2362	1.1691	1.00	47.9
	PC	0.2422	1.2430	0.99	46.2
LiFSI	DMC	0.1734	1.1313	0.88	28.7
	EC/DMC	0.1914	1.1906	1.01	30.1
	PC	0.1911	1.2073	1.02	29.6

Table S1. Electrolyte compositions used in preliminary (anion and solvent effects) studies. EC/DMC refers to a mixture of EC and DMC in a 1:1 ratio, by weight.

Salt	Solvent	Salt Mass (g)	Solvent Mass (g)	Initial Molarity (mol L^{-1})	Final Molarity (mol L^{-1})	Molality (mol kg^{-1})	OCV (V)
$LiPF_6$	EC/DMC	0.08	6.0	0.1	0.0982	0.08	2.65
	EC/DMC	0.76	6.0	1.0	0.9332	0.83	2.87
	EC/DMC	1.5	6.0	2.0	1.7881	1.7	3.13
	EC/DMC	2.3	6.0	3.0	2.5545	2.5	3.26
	EC/DMC	3.6	6.0	4.8	3.7904	4.0	3.39

Table S2. Electrolyte compositions used in optimization (concentration effects) studies. EC/DMC refers to a mixture of EC and DMC in a 1:1 ratio, by weight.

Open-Circuit Voltages: The open circuit voltage (OCV) for each cell composition is shown in Table S3.

Salt	Solvent	Initial Molarity (mol L^{-1})	OCV (V)
$LiClO_4$	DMC	1.05	2.84
	EC/DMC	1.02	2.68
	PC	0.97	3.04
$LiBF_4$	DMC	1.00	3.23
	EC/DMC	1.05	3.40
	PC	1.00	3.10
$LiPF_6$	DMC	1.03	3.14
	EC/DMC	1.06	2.89
	PC	0.93	2.92
$LiSbF_6$	DMC	1.00	2.99
	EC/DMC	1.00	3.02
	PC	1.01	2.87
LiFSI	DMC	0.88	2.97
	EC/DMC	1.01	3.07
	PC	1.02	2.95
LiFTFSI	DMC	0.99	2.93
	EC/DMC	1.00	2.95
	PC	0.99	3.12
LiTFSI	DMC	0.96	2.79
	EC/DMC	0.96	3.09
	PC	1.02	3.05

Table S3. OCV as a function of cell configuration (in two-electrode cells containing Li metal as the counter electrode).

Electrochemical Screening Data (Voltage Opening): The voltage opening experiments for all experiments carried out in the preliminary studies of all 21 final electrolytes are shown in Figures S1a-S1c.

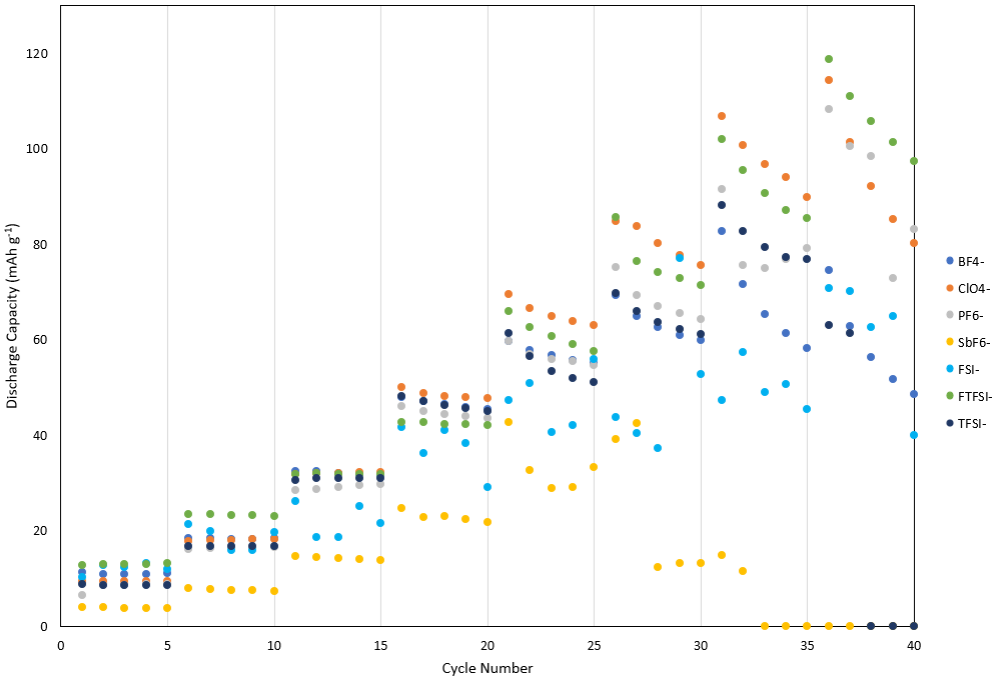

Figure S1a. Voltage opening dependencies (V vs. Li/Li+) of 7 anions in EC/DMC at 100 mA g-1.

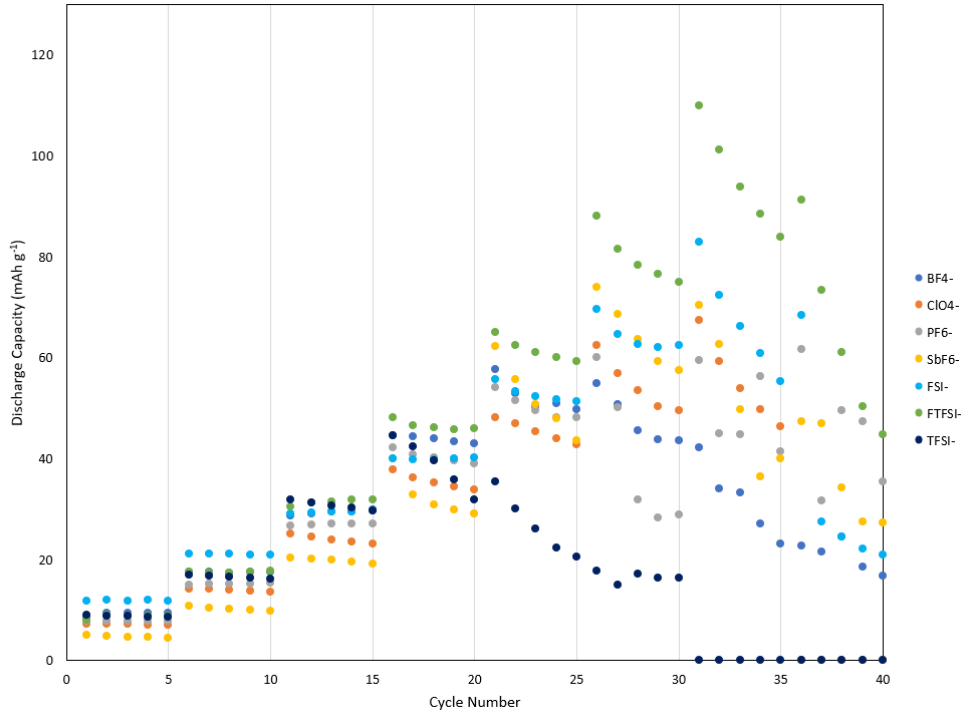

Figure S1b. Voltage opening dependencies (V vs. Li/Li+) of 7 anions in DMC at 100 mA g-1.

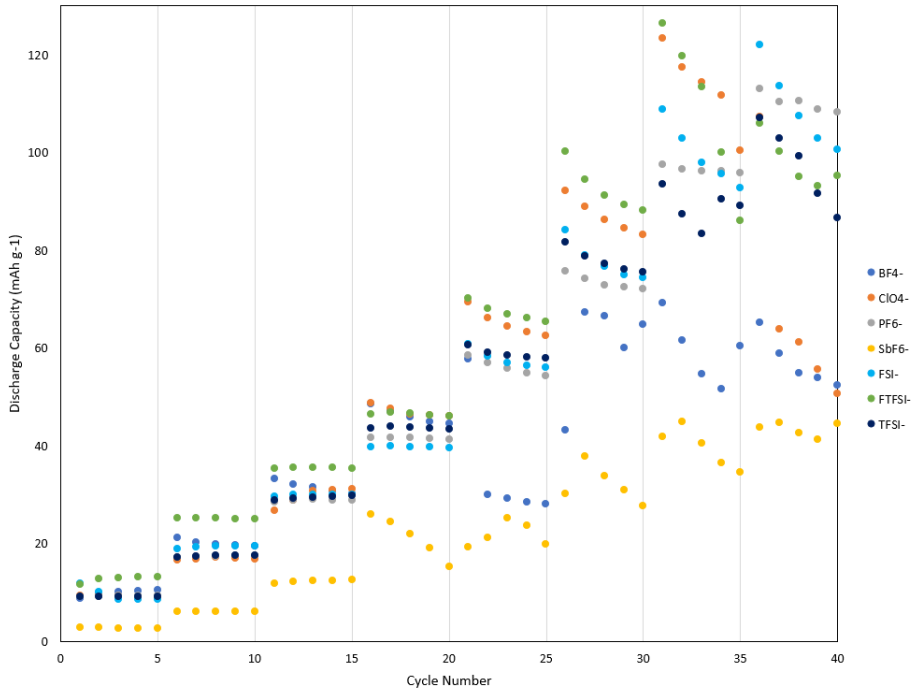

Figure S1c. Voltage opening dependencies (V vs. Li/Li^+) of 7 anions in PC at 100 mA g^{-1}.

Electrochemical Screening Data (Current Rate): The stepwise increasing current rate experiments carried out in the preliminary studies of all 21 final electrolytes are shown in Figures S2a-S2c.

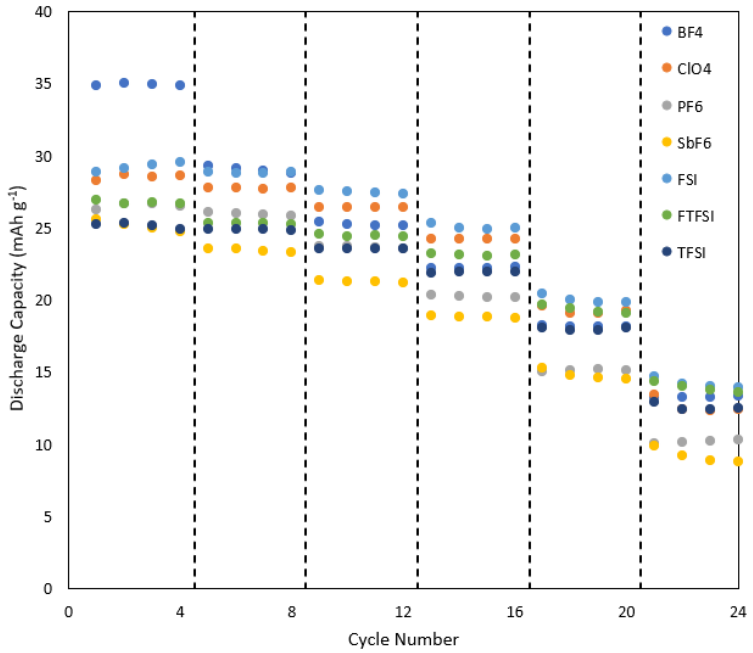

Figure S2a. Current rate dependencies (in mA g^{-1}) of 7 anions in PC cycled between 3.0-4.0 vs. Li/Li^+.

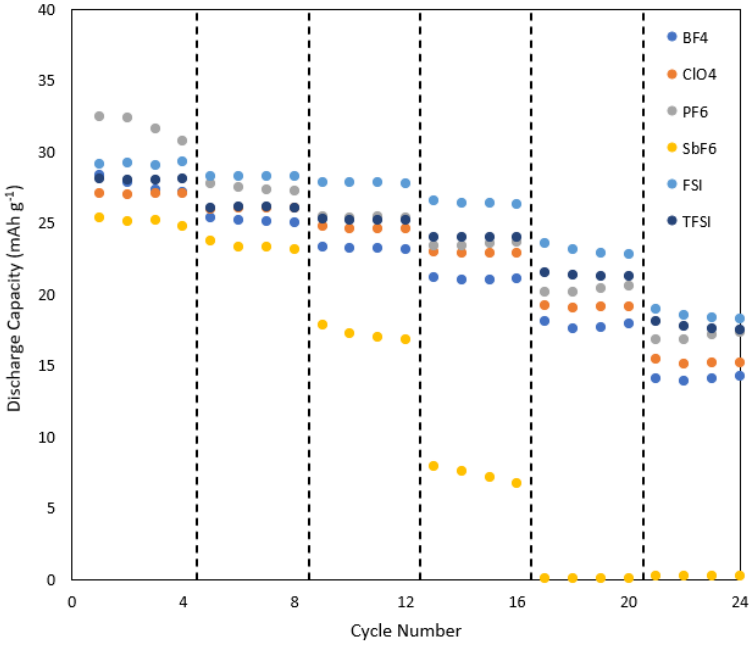

Figure S2b. Current rate dependencies (in mA g^{-1}) of 7 anions in EC/DMC cycled between 3.0-4.0 vs. Li/Li^+.

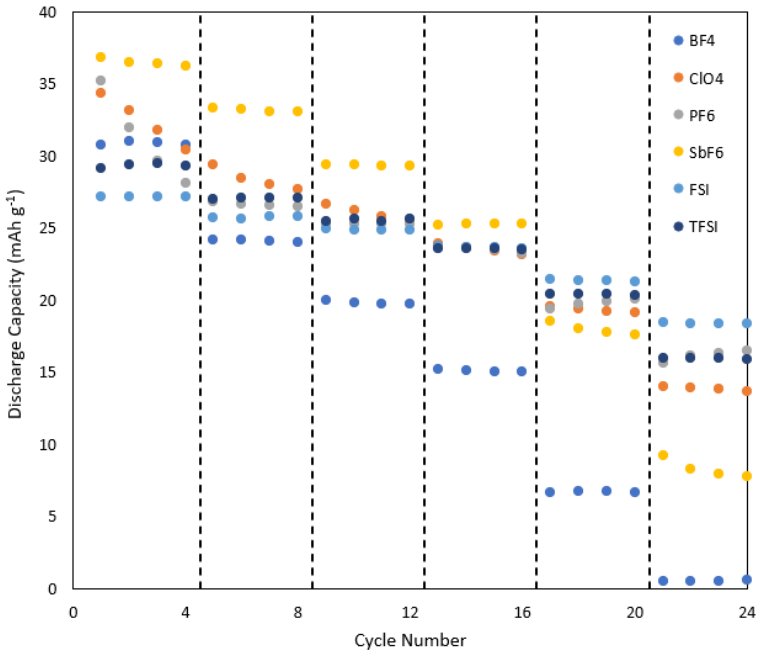

Figure S2c. Current rate dependencies (in mA g^{-1}) of 7 anions in DMC cycled between 3.0-4.0 vs. Li/Li^+.

Solvent Properties: Viscosity and dielectric are closely correlated among the three solvents studied in this work, as shown in Figure S3. In general, solvent choice can affect ion-pairing, solvation thermodynamics, diffusion, decomposition stability, and co-insertion (solvation shell size, diffusivity, etc.). [13]

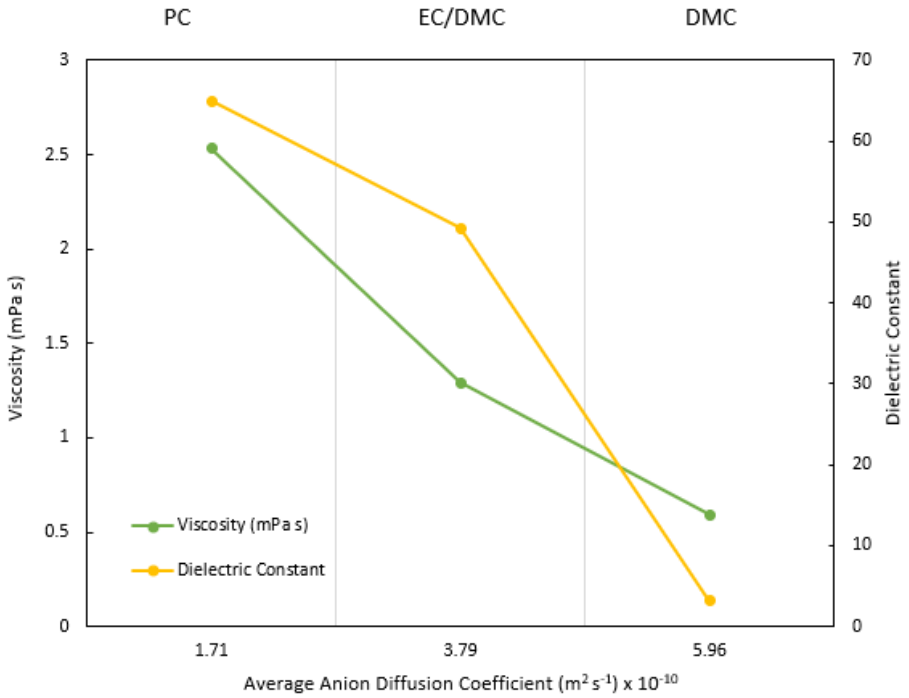

Figure S3. Viscosity and dielectric constant of PC, EC/DMC, and DMC as a function of the average anion diffusivity across all six fluorinated anions explored in this work.

	PC	**EC/DMC**	**DMC**
Viscosity (mPa s)	2.53	1.29	0.59
Dielectric Constant	64.96	49.21	3.12
Avg. Anion Diffusivity* (10^{-10} m^2 s^{-1})	1.71	3.79	5.96

Table S4. Solvent properties of PC, EC/DMC, and DMC. *Averaged over all fluorinated anions in this study.

Electrochemical Optimization Data (LiPF6 in EC/DMC): The voltage opening cycling voltammetry experiments carried out in the optimization studies of LiPF6 in EC/DMC are shown in Figure S4. The lower potential cutoff of 2.5 V vs. Li/Li+ was used to avoid undesirable Li+ ion insertion in ZTC, as described in previous studies.[24]

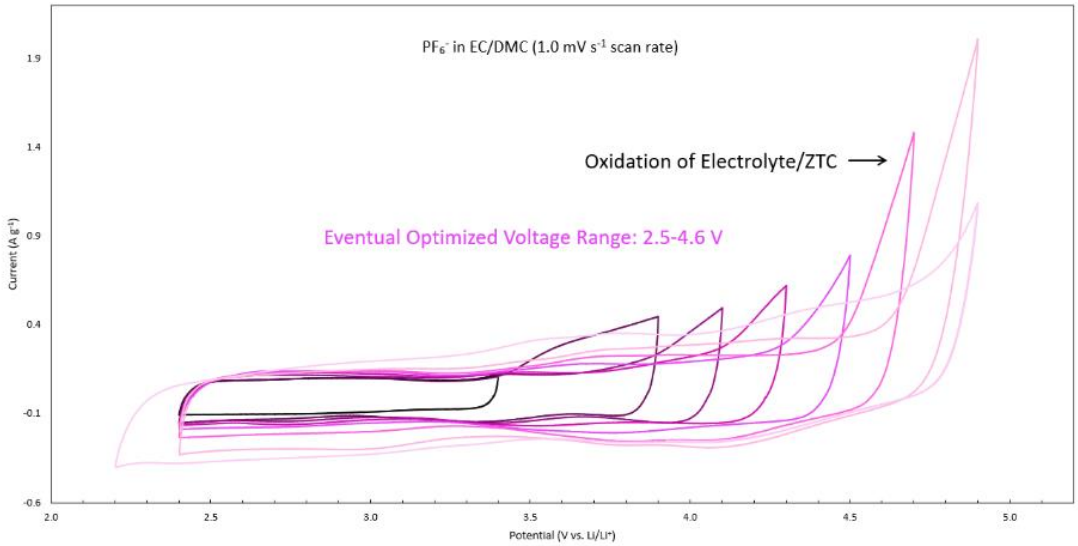

Figure S4. Cyclic voltammetry studies of 1.0 M $LiPF_6$ in EC/DMC at 1.0 mV s^{-1} cycled between 2.5-3.4 up to 2.5-4.9 V vs. Li/Li^+.

The voltage profiles for all experiments carried out in the subsequent optimization studies of $LiPF_6$ in EC/DMC are shown in Figure S5. The nominal concentrations are shown; actual concentrations are shown in Table S2.

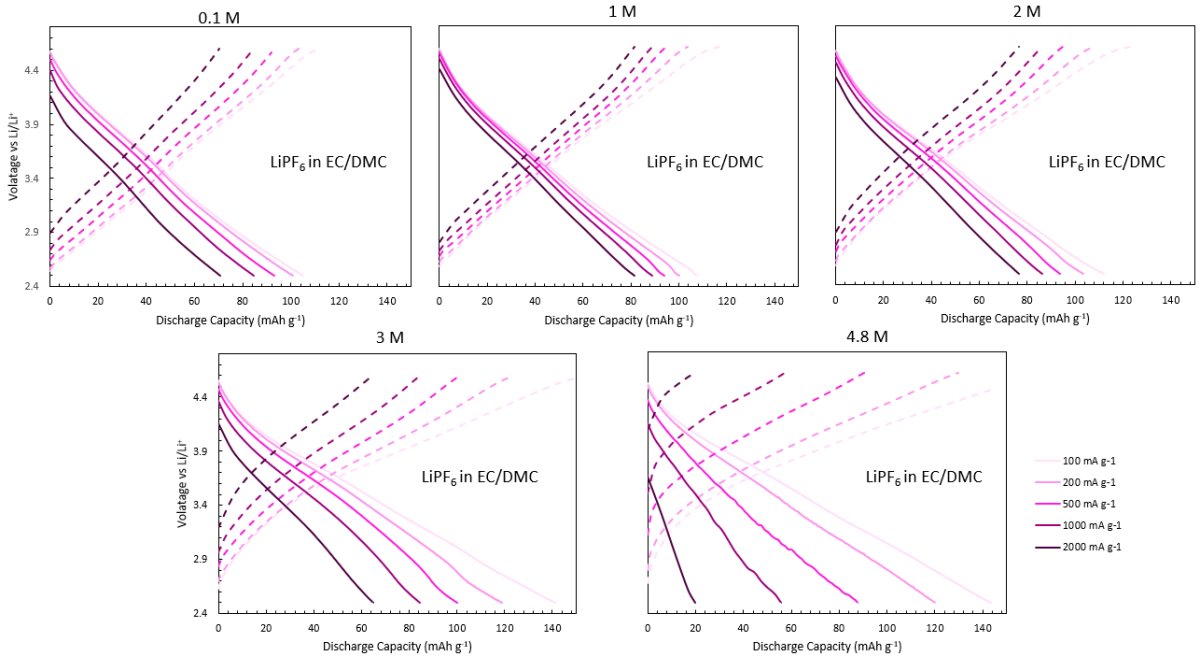

Figure S5. Voltage profiles for different concentrations of $LiPF_6$ in EC/DMC cycled between 2.5-4.6 V vs. Li/Li^+ and from 100 to 2000 mA g^{-1}.

Nominal Concentration (M)	**Actual Concentration (M)**	**Li^+**	**PF_6^-**	**EC**	**DMC**
0.1	0.0982	0.947	8.960	12.70	14.60
1.0	0.9332	0.414	4.170	5.27	6.32
2.0	1.7881	0.180	1.660	2.22	2.83
3.0	2.5545	0.047	0.396	0.50	0.56
4.8	3.7904	0.010	0.054	0.14	0.13

Table S5. Anion, cation, and solvent diffusivity (in 10^{-10} m^2 s^{-1}) for $LiPF_6$ in EC/DMC at the five concentrations explored in this study.

A Randles–Ševčík analysis of the insertion/deinsertion of PF_6^- within ZTC (1.0 M $LiPF_6$ in EC/DMC) is shown in Figure S6. Within the reduced 1.0 V window, charge storage in ZTC is purely capacitive with a B value of 0.94. In the wider 2.1 V window, more diffusive character is observed with a B value of 0.85.

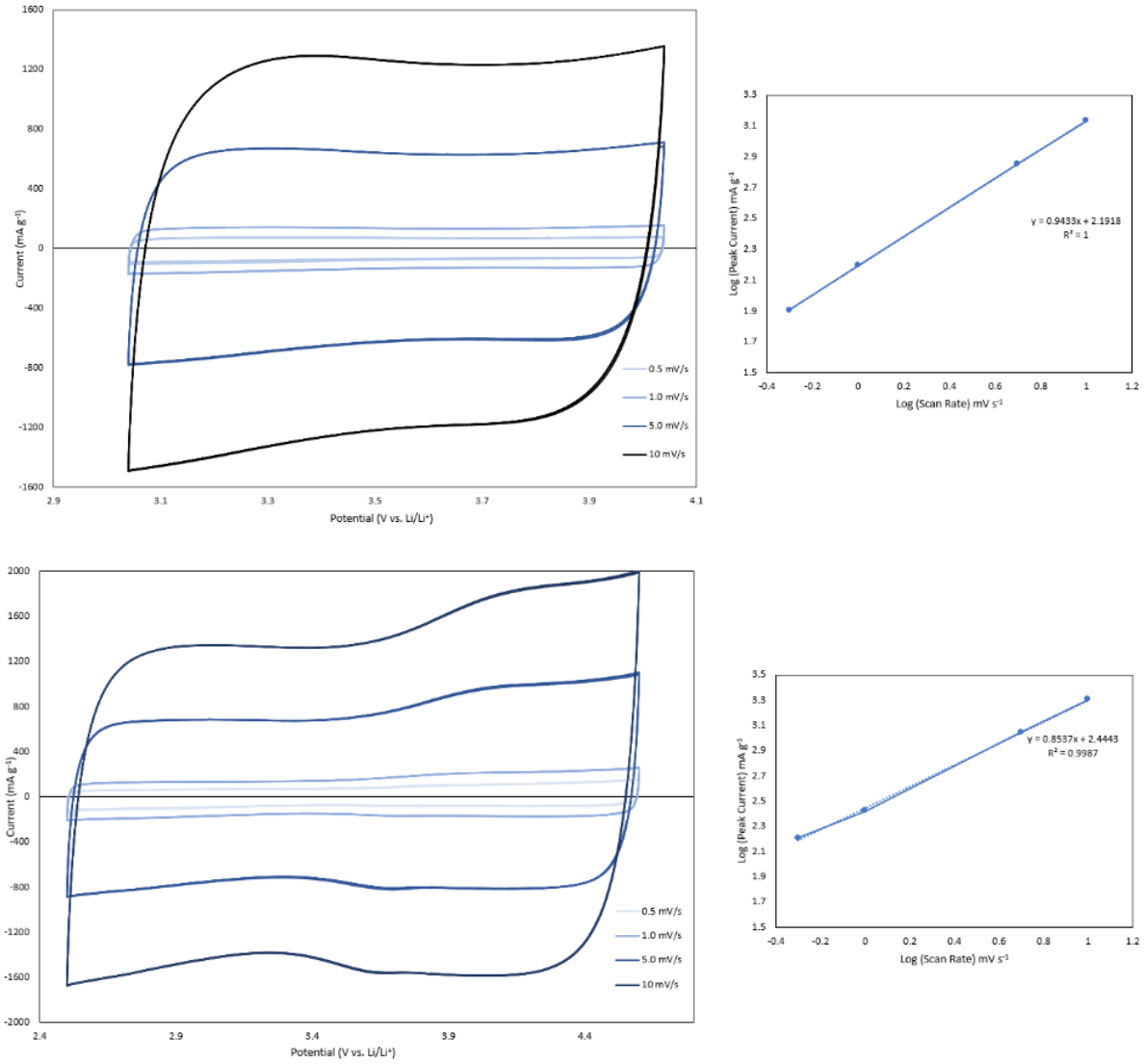

Figure S6. Cyclic voltammetry and Randles–Ševčík analysis between 3.0-4.0 V and 2.5-4.6 V vs. Li/Li^+ for 1.0 M $LiPF_6$ in EC/DMC. Separate cells were tested within each potential window and a total of three cycles were performed at each scan rate (0.5, 1.0, 5.0, and 10 mV s^{-1}).

ZTC Synthesis: ZTC was synthesized by a two-step (liquid/vapor) impregnation procedure. The zeolite NaY template (HSZ 320NAA, Tosoh Corp.) was degassed in a Büchi glass oven at 300 °C for 24 h under oil-free vacuum (<2 × 10-3 mbar). The dried zeolite (2 g) was then transferred (under Ar) into a 2-neck round bottom flask. The dried zeolite was

combined with 20 mL of furfuryl alcohol (FA, 99% Aldrich) via syringe and the mixture was stirred at room temperature, under passive vacuum for 24 h. The impregnated solid was collected by vacuum filtration in air, washed three times with 10 mL aliquots of mesitylene (97%, Aldrich), and then dried under suction on the filter frit for 15 minutes. The impregnated and rinsed zeolite was placed in an alumina boat (10 × 30 × 107 mm) which was inserted into a quartz tube (ø 45 mm) installed in a horizontal tube furnace (HST 12/600, Carbolite Gero). The tube was purged under dry argon flow (200 sccm) at ambient pressure. The FA within the zeolite pores was first polymerized by heating up to 80 °C via a 10 min ramp and held for 24 h. The poly-FA was then carbonized by heating up to 700 °C via a 2 h ramp and held for 30 min. Further carbon impregnation was accomplished via propylene CVD at 700 °C for 5 h; the gas flow was switched to 7 mol% propylene in argon (99.99% propylene in 99.999% argon) at 200 sccm. An annealing step (under pure argon flow) was performed by heating the zeolite-carbon composite up to 900 °C via a 40 min ramp and held for an additional 1 h. The system was then cooled overnight, the gas flow was stopped, and the annealed zeolite-carbon composite was collected. Removal of the zeolite templated was accomplished by three sequential dissolutions in 35 mL of aqueous hydrofluoric acid (HF, 48-51%, ACROS Organics). The final ZTC product was collected by centrifugation, washed three times with 35 mL aliquots of distilled water, and then dried in air at 40 °C prior to electrode fabrication.

ZTC Supercage Calculations: Each ZTC unit cell (Nishihara Model II+[20] contains 64 supercages of the original zeolite template, where the void space of the original supercages becomes a “filled” region comprising the struts of the ZTC while the excluded volume of the original zeolite (its silicate framework) becomes the void space of the ZTC. Owing to the self-

dual property of the diamond net (a simplification of the FAU structure), the number of supercages in faujasite is equal to the number of supercages in the corresponding FAU-ZTC. Thus, the conversion factor remains 64 supercages per unit cell. A single unit cell of Model II+ (a 2×2×2 supercell of the faujasite unit cell) has a lattice constant of a = 48.14 Å.

To determine the number of ions per supercage from the charge/discharge capacity in mAh g-1, the equation below is used:

$$n = x\frac{\text{mAh}}{\text{g}} \times \frac{3.6\ \text{C}}{\text{mAh}} \times \frac{6.241 \times 10^{18}\ \text{e}^-}{\text{C}} \times \frac{1\ \text{anion}}{\text{e}^-} \times \frac{0.4626\ \text{g}}{\text{mL}} \times \frac{1.116 \times 10^{-19}\ \text{mL}}{\text{cell}} \times \frac{1\ \text{cell}}{64\ \text{supercages}}$$

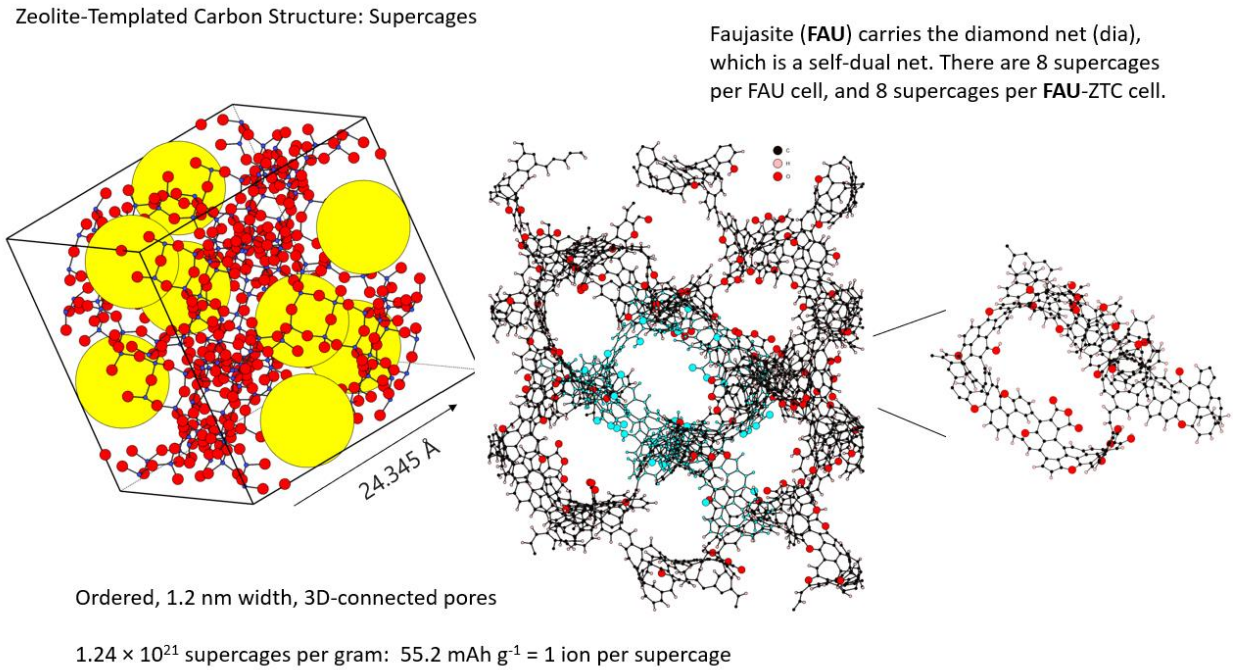

Figure S7. A representative ZTC "supercage".

Binder Effects: Three different techniques were tested for the fabrication of ZTC electrodes: PVDF slurry cast on Cu foil, PTFE free-standing electrodes, and bare ZTC powder

with no binder. The PVDF slurry did not adhere to the Cu foil and therefore did not proceed to electrochemical testing. The bare powder technique (no binder or additives) was chosen for all studies in this work due to its better performance over PTFE free-standing electrodes for capturing the "true" anion storage capacity of ZTC. The reduced capacity in PTFE electrodes can be attributed to pore-blocking.

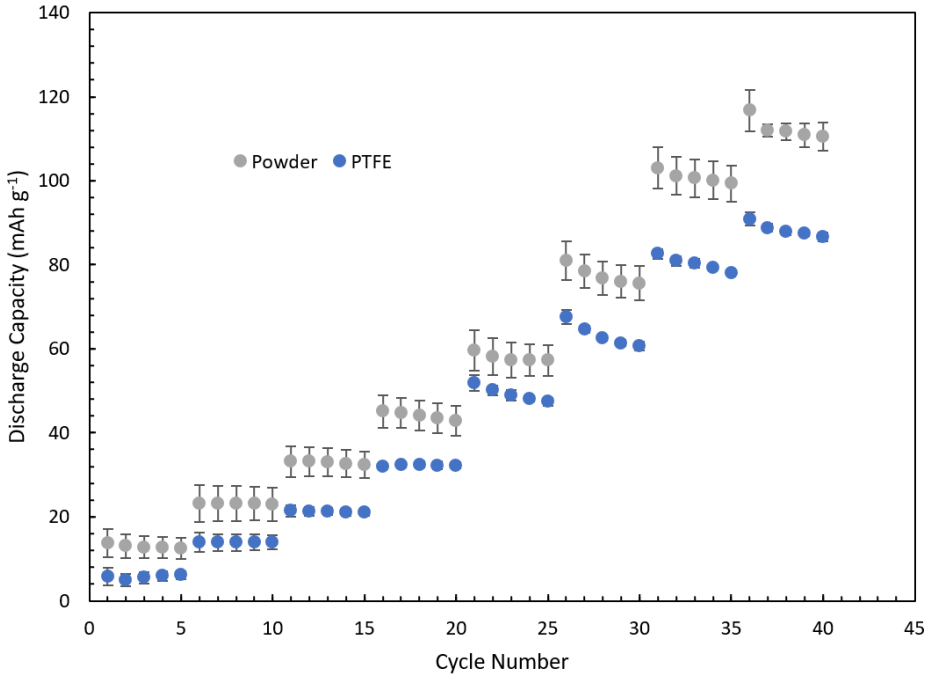

Figure S8**.** Direct comparison of ZTC electrodes formed by binding with PTFE and simply sprinkled into the cell without binder (as a bare powder). Error bars are standard deviations across all anions, tested in triplicate.

Self-Discharge Analysis: Ion leakage and self-discharge were analyzed by charging to 4.6 V vs Li/Li+, rested for 5 hours, and discharged to 2.5 V. A potential drop of 0.18 V and a capacity loss of 8.7 mAh g-1 was observed. The 10th cycle of 2 replicate cells is displayed so that capacity loss between charge and discharge can be diagnosed as ion rearrangement or leakage as opposed to side reactions.

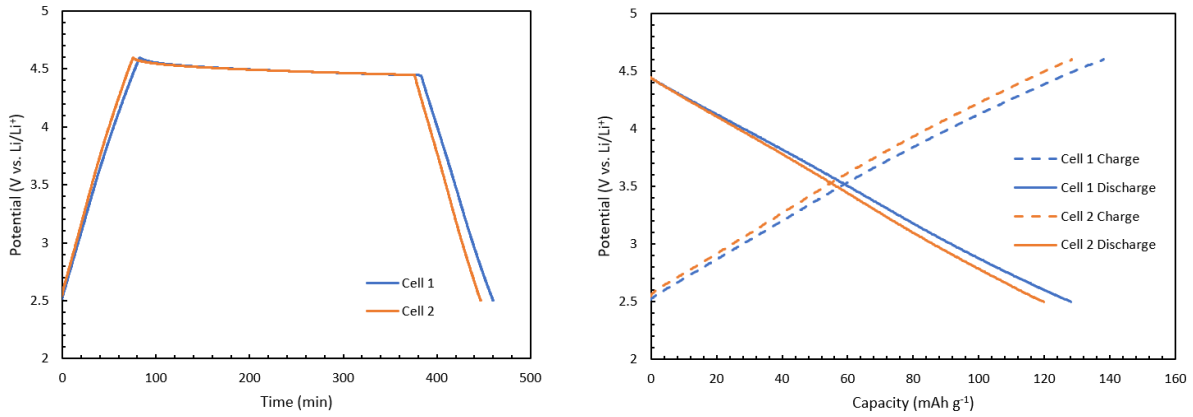

Figure S9. Galvanostatic charge/discharge was performed at 100 mA g^{-1} in the model electrolyte (1M $LiPF_6$ in EC/DMC) and cycled between 2.5 and 4.6 V vs Li/Li^+.

References

[1] T. Placke, R. Kloepsch, S. Dühnen, M. Winter, *J. Solid State Electrochem.* **2017**, 21, 1939-1964.

[2] W. H. Li, X. L. Wu, *Electrochem. Sci. Adv.* **2022**, *2* (4) e2100127.

[3] T. Ishihara, M. Koga, H. Matsumoto, M. Yoshio, *Electrochem. Solid-State Lett.* **2007**, *10*, A74.

[4] J. Xie, Y. C. Lu, *Nat. Commun.* **2020**, *11*, 2499.

[5] T. Panja, J. Ajuria, N. Diez, D. Bhattacharjya, E. Goikolea, D. Carriazo, *Sci. Rep.* **2020**, *10*, 10842.

[6] W. Fan, H. Zhang, H. Wang, X. Zhao, S. Sun, J. Shi, M. Huang, W. Liu, Y. Zheng, P. Li, *RSC Adv*. **2019**, *9*, 32382-32394.

[7] J. A. Seel, J. R. Dahn, *J. Electrochem. Soc.* **2000**, *147*, 892.

[8] T. Placke, O. Fromm, S. F. Lux, P. Bieker, S. Rothermel, H.-W. Meyer, S. Passerini, M. Winter, *J. Electrochem. Soc.* **2012**, *159*, A1755-A1765.

[9] M. Wang, Y. Tang, *Adv. Energ. Mater.* **2018**, *8* (19), 1703320.

[10] J. O. Besenhard, H. P. Fritz, *Angew. Chem. Int. Ed.* **1983**, *22* (12), 950-975.

[11] H. Zhang, Z. Li, W. Xu, Y. Chen, X. Ji, M. M. Lerner, *Nanotechnol.* **2018**, *29*, 325402.

[12] J. A. Read, *J. Phys. Chem. C* **2015**, *119*, 8438-8446.

[13] D. M. Seo, S. Reininger, M. Kutcher, K. Redmond, W. B. Euler, B. L. Lucht, *J. Phys. Chem. C* **2015**, *119*, 14038-14046.

[14] S. Han, *Sci. Rep.* **2019**, *9*, 5555.

[15] Z. Hu, Q. Liu, K. Zhang, L. Zhou, L. Li, M. Chen, Z. Tao, Y. M. Kang, L. Mai, S. L.

Chou, J. Chen, S. X. Dou, *ACS Appl. Mater. Interfaces* **2018**, *10*, 35978-35983.

[16] Y. Liang, H. Dong, D. Aurbach, Y. Yao, *Nat. Energy* **2020**, *5*, 646-656.

[17] I. A. Rodríguez-Pérez, X. Ji, *ACS Energ. Lett.* **2017**, *2*, 1762-1770.

[18] X. Zhou, Q. Liu, C. Jiang, B. Ji, X. Ji, Y. Tang, H. M. Cheng, *Angew. Chem. Int. Ed.* **2020**, *59*, 3802-3832.

[19] T. Placke, P. Bieker, S. F. Lux, O. Fromm, H.-M. Meyer, S. Passerini, M. Winter, *Z. Phys. Chem.* **2012**, *226*, 391-407.

[20] H. Nishihara, T. Kyotani, *Chem. Commun.* **2018**, *54*, 5648-5673.

[21] H. Nishihara, H. Fujimoto, H. Itoi, K. Nomura, H. Tanaka, M. T. Miyahara, P. A. Bonnaud, R. Miura, A. Suzuki, N. Miyamoto, N. Hatakeyama, A. Miyamoto, K. Ikeda, T. Otomo, T. Kyotani, *Carbon* **2018**, *129*, 854-862.

[22] E. E. Taylor, K. Garman, N. P. Stadie, *Chem. Mater.* **2020**, *32*, 2742-2752.

[23] N. P. Stadie, S. Wang, K. V. Kravchyk, M. V. Kovalenko, *ACS Nano* **2017**, *11*, 1911-1919.

[24] R. J. Dubey, J. Nussli, L. Piveteau, K. V. Kravchyk, M. D. Rossell, M. Campanini, R.

Erni, M. V. Kovalenko, N. P. Stadie, *ACS Appl. Mater. Interfaces* **2019**, *11*, 17686-17696.

[25] R. J. Dubey, T. Colijn, M. Aebli, E. E. Hanson, R. Widmer, K. V. Kravchyk, M. V. Kovalenko, N. P. Stadie, *ACS Appl. Mater. Interfaces* **2019**, *11*, 39902-39909.

[26] K. Matsuoka, Y. Yamagishi, T. Yamazaki, N. Setoyama, A. Tomita, T. Kyotani, *Carbon* **2005**, *43*, 876-879.

[27] Z. Ma, T. Kyotani, A. Tomita, *Carbon* **2002**, *40* (13), 2367-2374.

[28] S. J. Gregg, K. S. W. A. Sing, *Adsorption, Surface Area and Porosity*, **1982**, 2nd ed., Academic Press, New York.

[29] S. Wang, K. V. Kravchyk, A. N. Filippin, U. Muller, A. N. Tiwari, S. Buecheler, M. I. Bodnarchuk, M. V. Kovalenko, *Adv. Sci.* **2018**, *5*, 1700712.

[30] S. Wang, K. V. Kravchyk, A. N. Filippin, R. Widmer, A. N. Tiwari, S. Buecheler, M. I. Bodnarchuk, M. V. Kovalenko, *ACS Appl. Energ. Mater.* **2019**, *2*, 974-978.

[31] R. Rowsey, E. E. Taylor, S. Irle, N. P. Stadie, R. K. Szilagyi, *J. Phys. Chem. A* **2021**, *125*, 6042-6058.

[32] N. Mardirossian, M. Head-Gordon, *J. Chem. Theory Comput.* **2016**, *12*, 4303-4325.

[33] E. Jonsson, P. Johansson, *Phys. Chem. Chem. Phys.* **2015**, *17*, 3697-3703.

[34] J. B. Goodenough, K. S. Park, *J. Am. Chem. Soc.* **2013**, 135, 1167-1176.

[35] S. J. An, J. Li, C. Daniel, D. Mohanty, S. Nagpure, D. L. Wood, *Carbon* **2016**, *105*, 52-76.

[36] M. Ue, M. Takeda, M. Takehara, S. Mori, *J. Electrochem. Soc.* **1997**, *133*, 2684-2688.

[37] K. Xu, *Chem. Rev.* **2004**, 104, 4303-4418.

[38] O. Borodin, W. Behl, T. R. Jow, *J. Phys. Chem. C* **2013**, *117*, 8661-8682.

[39] J. B. Haskins, W. R. Bennett, J. J. Wu, D. M. Hernandez, O. Borodin, J. D. Monk, C. W. Bauschlicher, Jr., J. W. Lawson, *J. Phys. Chem. B* **2014**, *118*, 11295-11309.

[40] M. T. Ong, O. Verners, E. W. Draeger, A. C. van Duin, V. Lordi, J. E. Pask, *J. Phys. Chem. B* **2015**, *119*, 1535-1545

[41] E. O. Stejskal, J. E. Tanner, *J. Chem. Phys.* **1965**, *42*, 288-292.

CHAPTER FOUR

ON THE DIVERGENT ELECTRICALLY CONDUCTIVE PATHWAYS IN YTTRIUM-BASED 2- AND 3-DIMENSIONAL METAL–ORGANIC FRAMEWORKS

Contribution of Authors and Co-Authors

Manuscript in Chapter 4

Author: Connor Welty

Contributions: Synthesized materials, collected data, analyzed data, produced figures, and wrote the manuscript.

Co-Author: Eoghan L. Gormley

Contributions: Collected computational data and produced figures.

Co-Author: Julius J. Oppenheim

Contributions: Assisted with data collection.

Co-Author: Mircea Dincă

Contributions: Inspired the research direction and supplied the work space.

Co-Author: Christopher H. Hendon

Contributions: Provided intellectual advice and assisted in writing and editing the manuscript.

Co-Author: Nicholas P. Stadie

Contributions: Advised with the experimental direction, interpreted results, and assisted in writing and editing the manuscript.

Manuscript Information

Connor Welty, EoghanL. Gormley, Julius J. Oppenheim, Mircea Dincă, Christopher H. Hendon and Nicholas P. Stadie

ACS Materials Letters

Status of Manuscript:
☐ Prepared for submission to a peer-reviewed journal
☐Officially submitted to a peer-reviewed journal
☐ Accepted by a peer-reviewed journal
☒Published in a peer-reviewed journal

ACS Publications

Abstract

Despite most porous framework solids exhibiting insulating character, some are known to conduct electrical charge. The peak performing conductive metal-organic frameworks are composed of redox-active hexasubstituted triphenylene linkers, but the impact of redox activity on material conductivity remains enigmatic because of limited availability of direct structure-function relationships. Here, we report a hexagonal yttrium-based conductive porous scaffold, comprising hexahydroxytriphenylene connected by Y-chains (YHOTP). In comparison to its known porous cubic counterpart (Y_6HOTP_2), this material features a 1000-fold increase in peak conductivity in polycrystalline samples (~10^{-1} S cm^{-1}). Furthermore, through a comparison of their electronic structures, we rationalize the origin of this difference and highlight the role of charge carrier concentration in dictating bulk electrical conductivity. Together, this work provides a design principle for the development of next-generation conductive porous frameworks.

Most metal-organic frameworks (MOFs) are electrical insulators due to energetic mismatch between the metal clusters and the ligands that support them. [1-3] MOFs that do conduct electricity feature conductive pathways that permit charge mobility either through space (through π-stacking or other secondary bonding) [4] or through bond (through dative, ionic, or covalent bonds) [5], and are potentially useful as active materials in electrocatalysis[6-8] and in electrochemical energy storage devices. [9-13] To date, the highest performing conductive MOFs feature conductivity values exceeding 100 S cm^{-1} and are through-space conductors. Effort has been invested in understanding how the spatial orientation of the MOF components dictates the crystal conductivity, however very few structure-function relationships have been revealed. A

comparison of compositionally similar frameworks with dissimilar geometries is required to elucidate basic principles that underpin electrical conduction in molecular materials.

Since electrical conductivity is primarily dictated by the number and mobility of charge carriers, interest has been focused on methods to affect band curvature and the free carrier concentration in the materials. Towards the latter, two strategies have been developed; either through electrochemical doping[14] or through narrowing of the electronic band gap via ligand functionalization. [15] With the exception of mixed-valent Fe-based frameworks, the most conductive MOFs are composed of hexasubstituted triphenylenes (e.g., hexahydroxytriphenylene, HHTP, which is referred to as HOTP once incorporated into the framework) [16] and their synthesis does not afford an obvious route to introduce functionalization beyond the ligating atoms themselves.[17–19] Instead, those linkers are known to oxidize during self-assembly, introducing charge carriers through redox events. Once assembled, the charge carriers are thought to traverse the closely-spaced π-stacked layers, leading to anisotropic through-space conduction. [20, 21]

When paired with first row transition metals (e.g., Co, Ni, Cu) [22-24], the resultant 2D-connected layered materials exhibit among the highest known electrical conductivity of any MOFs to date. Stacking faults may disrupt the π-overlap between layers, and subsequently result in variable and reduced conductivity. Larger metal cations (e.g., La, Ho, Nd, Yb) have been shown to reduce stacking faults and form large crystals.[25] In those cases, the metals sit between the organic sheets and, like the other 2D-conductive MOFs, those formed from *f*-block elements are known to be in-plane insulators, and out-of-plane metals. Meanwhile, some of the same metal ions can be used to form a 3D-connected cubic framework, with reported structures made

from La, Eu, and Y.[26] Thus, the formation of iso-compositional frameworks with dissimilar connectivity, but high degrees of covalency remain key targets in MOF syntheses.

Noting that Y^{3+} supports a larger coordination sphere than its kainosymmetric azimuthal analogue (Sc^{3+}), we surmised that Y could be used to form the tightly spaced layered structure of MHOTP. In doing so, Y would be the only *d*-block element capable of reliably forming both the hexagonal and cubic structures, permitting a controlled analysis of the properties that drive electrical conduction in this class of materials. Here, we report the synthesis of YHOTP, and through comparison with its known cubic 3D counterpart, Y_6HOTP_2, we show that the spatial orientation of the linkers dictates the conductive pathways due to divergent linker behavior. The 2D material exhibits strong intermolecular electron and hole charge transfer coupling, while the 3D structure hosts high charge carrier concentrations.

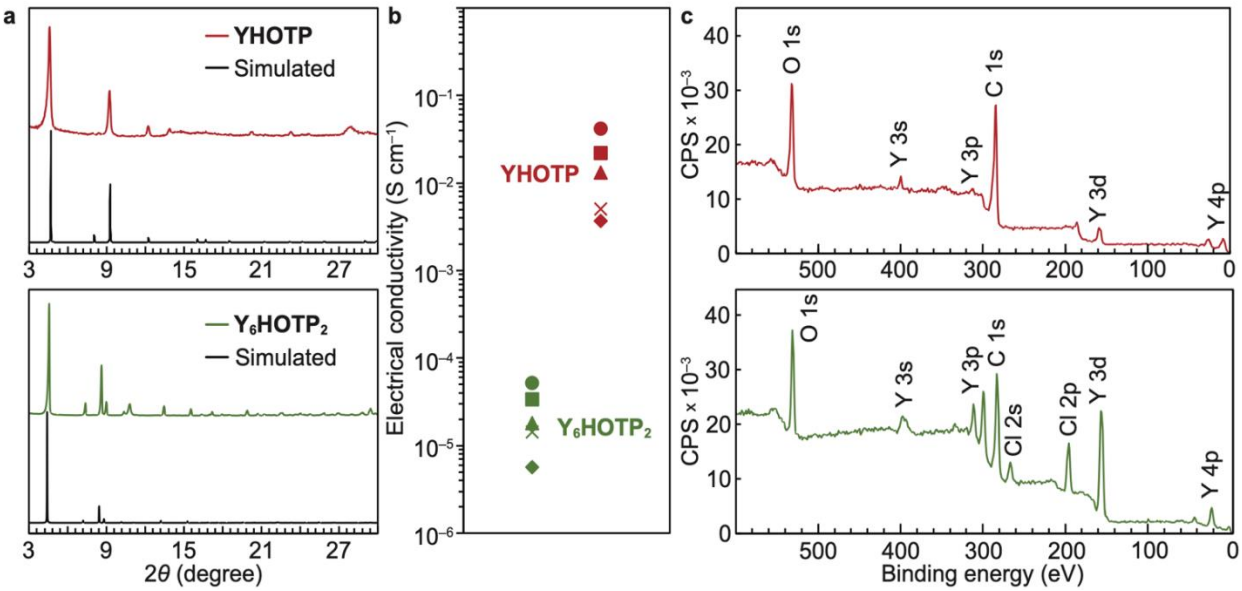

Figure 1. Materials characterization comparison of YHOTP and Y_6HOTP_2. **(a)** Powder XRD patterns reveals the microcrystalline sample is highly crystalline. **(b)** Pressed pellet conductivities of five different batches of each MOF. **(c)** XPS show the presence of Cl in the Y_6HOTP_2, and differences in the C 1s binding energy, attributed to differences in linker oxidation state.

To target the layered hexagonal 2D structure, YHOTP was obtained by mixing $Y(NO_3)_3 \cdot 6H_2O$ with HHTP in a mole ratio of 10:1 in a mixture of water, *N,N'*-dimethylimidazolidinone (DMI), and sodium acetate (NaOAc). The reaction mixture was held at 80 °C for 16 h in air, then washed and dried to obtain $(YOH)_{1-x}HOTP(H_2O)_n$ (x = 0 to 0.2; referred to as YHOTP). Y-vacancies are accounted for with positive values of x. To obtain the cubic 3D structure, YCl_3 was used in a metal:linker mole ratio of 80:1. To promote crystallization and disincentivize oxidation, the mixture was heated to 135 °C for 72 h in a nitrogen-filled glovebox in a similar solvent mixture. The resultant material, $Y_6(HOTP)_2(CO_3)Cl_6$ (Y_6HOTP_2) was obtained. We surmised that the carbonate was formed during self-assembly through solvent decomposition, and trace nitrogen in the elemental analysis likely corresponds to trapped solvent within the pores. Both products' chemical compositions were determined by a combination of single-crystal X-ray diffraction (XRD), X-ray photoelectron spectroscopy (XPS), and elemental analysis (Tables S1-S6). Microcrystalline samples of each product were found to have the same crystallographic structure as that of the bulk single crystals of each MOF (Figure 1a).

Following the reported procedure for measuring electrical conductivity on polycrystalline samples, pressed pellet conductivities were determined in pentaplicate, using a two-point probe device detailed in the Experimental Methods. The hexagonal 2D framework, YHOTP, consistently exhibited at least 1000× higher conductivity than its cubic 3D counterpart, with a peak conductivity of $\sim 3 \times 10^{-1}$ S cm^{-1} (Figure 1b). A similar conclusion is predicted through a comparison of the computed electronic band structures (Figure 2). However, despite the cubic material possessing an insulating ground state electronic structure[8], the material has surprisingly

high peak conductivities of ~10^{-4} S cm^{-1}, which is as much as 9 orders of magnitude greater than MOFs with comparable band gaps.[5] Thus, we surmised that another effect may be dictating the electrical conduction in these frameworks.

One explanation for this divergence could be a difference in charge carrier concentration. Since we are unable to grow single crystals large enough to perform a Hall measurement, we instead deduce the concentration from theory. By comparing the curvature of the bands in the direction with the lightest holes and electrons (Γ–A for YHOTP, Γ–X for Y_6HOTP_2), the electronic band structure calculations reveal approximately two orders of magnitude difference in effective mass of the charge carriers, with the heavier carrier belonging to Y_6HOTP_2. Since conductivity is proportional to the charge carrier concentration and mobility, and the differences in mobility are of the same order of magnitude as the pressed-pellet conductivity, the corresponding carrier concentration must not vary by more than one order of magnitude.

Considering the composition differences, and that the XPS data presented in Figure 1c indicate that Y exists in the 3+ oxidation state, the differences in conductivity are driven by a combination of dissimilar linker oxidation state and intermolecular orientation. Since the 2D structure only forms in the presence of air, it is understood that the linker oxidizes during self-assembly. With complementary deprotonation, the hexagonal layered material hosts linkers with nominal 3– charge. This charge should result in a single unpaired electron per linker but solid-state EPR reveals YHOTP has substantially less radical character than the cubic analogue (Figure S1), which has been previously attributed to linker vacancies rather than native ligand-centered unpaired electrons.[25] Thus, we surmised that the linkers rather exist as a delocalized 2– and 4– pair, an electronic configuration common in the 2D conductive family of frameworks.[20]

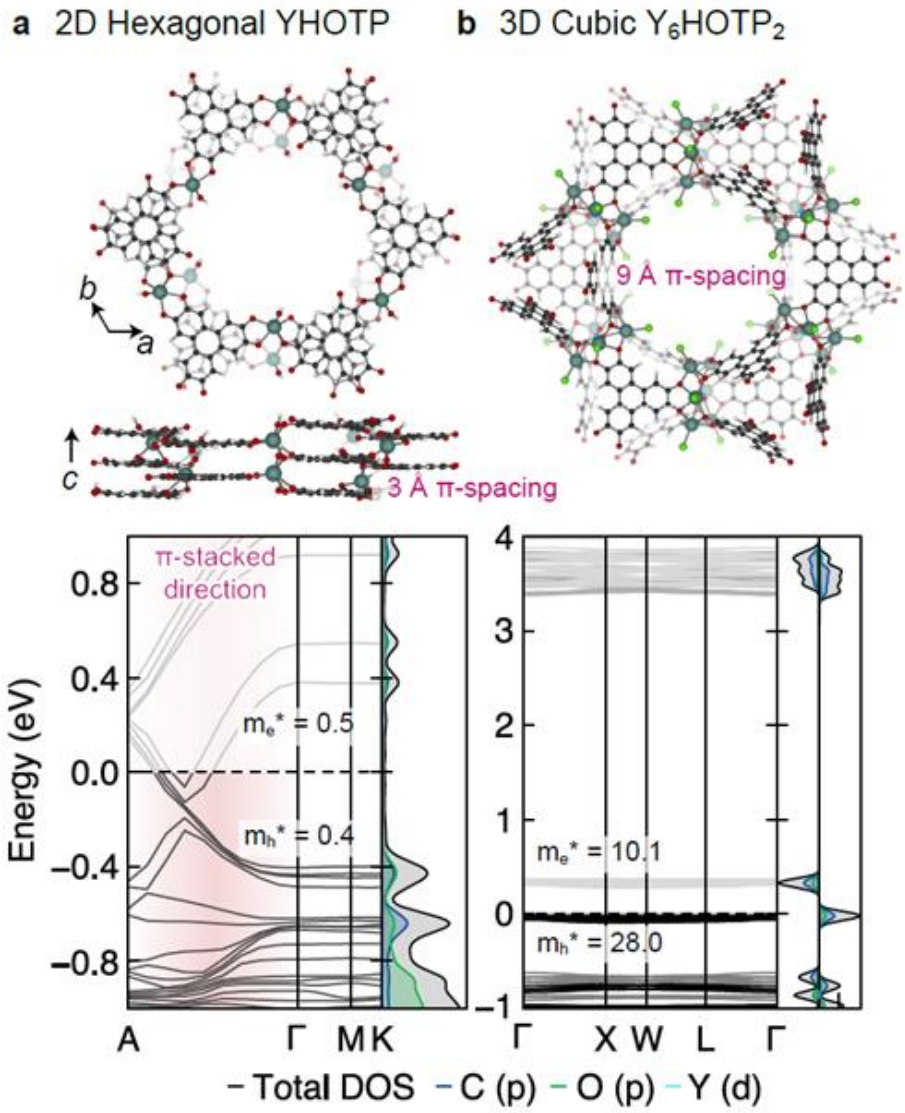

Figure 2. (a) The hexagonal (YHOTP) and (b) cubic (Y_6HOTP_2) crystal structures and corresponding electronic band structures. The former has pathways of through-space π-interactions, while the latter features isolated chemical motifs. The proximity of π-clouds in YHOTP is reflected in its electronic band structure, where it is predicted to be an out-of-plane metal and in-plane narrow gap insulator. Y_6HOTP_2 is predicted to be a narrow gap insulator due to limited spatial overlap throughout the crystal, with band edge densities localized on the ligand. Charge carrier effective masses are labeled. C, O, Cl, H, and Y, are depicted in black, red, green, white, and sage, respectively.

Conversely, Y_6HOTP_2 forms under a nitrogen atmosphere and, hence, should be less oxidized. In its case, the linkers exhibit a formal 5– charge. In this charge state, the linkers are

nominally more aromatic than their oxidized counterparts and should host unpaired electrons. EPR revealed a ligand-centered radical associated with a single unpaired electron per linker (Figure S1). The difference concentration in mobile charge carriers cannot vary by more than one electron per linker, supporting our offering that the difference in charge carrier concentration will never exceed one order of magnitude. This may be the origin of elevated conductivity in Y_6HOTP_2 compared to other similarly flat-banded materials — the linker is likely installing large numbers of charge carriers.

Both YHOTP and Y_6HOTP_2 are through-space conductors but have different ligand geometries. This is generally interesting because intermolecular distances usually increase with increasing porosity, and these frameworks serve as a platform to understand how orientation impacts through-space conduction, and whether having spatially separated ligands can permit charge transfer between them. To do so, we turn to Marcus theory to assess the charge transfer coupling between neighboring ligands. We created two models from the bulk crystals, each featuring a pair of linkers with their geometry remaining fixed, as imposed by the geometry obtained for the crystal.[27] The linkers were then protonated to create a charge-neutral system (Figure 3). The cluster's molecular orbitals were computed using the ZINDO method[28], and the electron and hole couplings were extracted using an open-source code, py-MOO.[29] For the cubic system, the hole transfer coupling was found to be 0.075 meV, while the electron coupling was 0.9 meV. Both of these values are extremely weak. The hexagonal crystal featured coupling energies of 363 and 307 meV for the electron and hole, respectively. These values are relatively large and are comparable to other organic charge transfer aggregates.[30, 31] Together we surmise that for the hexagonal system, the mobility of the charge carriers is high reflected in the band

structure and also in the hole and electron coulping energies. Conversely, the cubic system features weak couplings, and highly localized electronic bands.

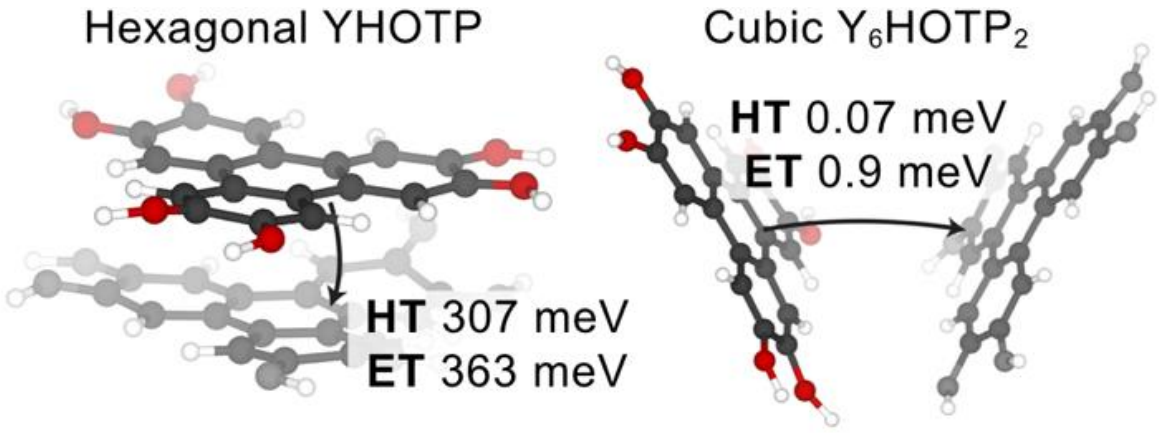

Figure 3**.** A comparison of the hexagonal (**YHOTP**) and cubic (**Y$_6$HOTP$_2$**) ligand charge transfer interactions. The electron coupling (ET) is consistently larger than the hole coupling (HT) driven by the propensity for the ligands to rearomatize. C, O, and H are depicted in black, red, and white, respectively.

Thus, through the isolation of a Y-based hexagonal layered conductor, YHOTP, and by comparison to its cubic counterpart, Y_6HOTP_2, we can make several conclusions. Given that the coupling energies in the latter are extremely weak, but its charge carrier effective masses are comparable to other flat-band insulators, the reason for its surprisingly high conductivity (~10^{-4} S cm^{-1}) is likely due to the differences in linker oxidation state, which we believe is directly influencing the charge carrier concentration in the MOF. Further, given that the linker is more aromatic in the 3D framework — a property that is typically inversely proportional to conductivity[32] — this strongly indicates that linker redox is a critical and primary deciding factor dictating electrical charge conduction in MOFs, and highlights that the interplay between linker redox potential and orientation dictates bulk conductivity. Looking forward, these findings help

rationalize why the HOTP-based materials are the best conductors in their class and should instruct future efforts to diversify ligand design.

Experimental Section

Synthesis of YHOTP and Y_6HOTP_2

Prior to synthesis, HHTP was dissolved in DMI and recrystallized from hot H2O to remove impurities. For the synthesis of YHOTP, 0.63 mmol of Y(NO3)3·6H2O was dissolved in 3 mL of deionized H2O in a 20 mL scintillation vial in air. 0.063 mmol of HHTP was dissolved in 0.8 mL of DMI and the two solutions were combined. A solution of 0.189 mmol of NaOAc dissolved in 0.6 mL of deionized H2O was added to the mixture. The mixture was transferred to a 15 mL pressure tube containing sanded glass slides and heated at 80 °C for 16 h. For the synthesis of Y6HOTP2, 4.8 mmol of YCl3·6H2O was dissolved in 3 mL of deionized H2O and added to a solution of 0.06 mmol of HHTP dissolved in 0.8 mL of DMI in a N2-filled glovebox. 0.18 mmol of NaOAc dissolved in 0.6 mL of deionized H2O was added to the mixture and then the solution was filtered into a 15 mL pressure tube containing sanded glass slides using a 0.2 μm PTFE filter. The reaction was heated at 135 °C for 72 h and then brought back into the N2-filled glovebox. The mother liquor was decanted and the resulting powder was washed 3× with deoxygenated DI water and 3× with deoxygenated methanol. Both samples were activated by drying under vacuum at 90 °C for 1 h.

Electrical Conductivity Measurements

Two-point probe measurements were made on activated pressed pellets using a custom apparatus previously described.[33] 2-3 mg of powder was loaded into a glass tube and compressed

by copper rods that also served as leads. The apparatus was compressed using a hydraulic press while dual linear I-V curves were obtained using a Keithley 2450 source meter. The pellets were further compressed between I-V measurements until the change in resistance was low (Figure S2). The conductivity measurements were made in pentaplicate.

Materials Characterization

Powder XRD measurements were performed using a Bruker D8 Advance diffractometer with Cu $K\alpha_{1,2}$ radiation (λ = 1.54 Å) in reflection geometry. EPR was performed using a Magnettech ESR5000 spectrometer with a microwave power of 20 mW and an amplitude of 0.3 G.

Computational Methods

Density functional theory (DFT) calculations were performed using the Vienna ab initio Simulation Package (VASP)[34]. All structures were optimized using the PBEsol functional with a plane wave energy cutoff of 500 eV, and an ionic convergence criterion of –0.005 eV. Bulk YHOTP was optimized using a 2×2×5 k-mesh to sample the first Brillouin zone, and all structures involving Y6HOTP2 used a Γ-only k-mesh due to the size of the unit cell and the resulting computational cost of the calculation. Y6HOTP2 is charge-balanced by disorder guest molecules in the pores. Here, we achieved charge balance by adding one Cl per Y, capping the open metal sites in the metal clusters. The electron count was adjusted by the removal of 4 electrons, achieving charge neutrality. This strategy significantly reduced the net charge of the structure in the calculations, aligned with the experimental number of charges on each linker from EPR, and is justified due to the presence of Cl in the elemental analysis. We also tested an alternate charge balancing method, by removing the chlorides and subtracting 20 electrons (2.5

per linker) from the system. The former strategy yielded a plausible structure that was then used for the electronic band structure calculation. The HSEsol hybrid functional35 was used to compute the band structures. ZINDO calculations for the linker pairs were performed as implemented in Gaussian0929, and the CT couplings were calculated using the Molecular Orbital Overlap (MOO) method.

Associated Content

Acknowledgements

We thank Grigorii Skorupskii for synthetic insights, Andrei Iliescu for performing the XPS experiments, and Isaac Sanchez for assistance with the EPR experiments. C.W. and N.P.S. are grateful for funding provided by the National Science Foundation (award OIA-2034110). Computational aspects of this paper are supported by the National Science Foundation through the Division of Materials Research (award DMR-1956403) and the Camille and Henry Dreyfus Foundation. Work in the Dincă lab was supported by the Department of Energy (award DE-SC0023288). This work was performed using Expanse at the San Diego Supercomputing Center (SDSC) through allocation CHE-160003 and CHE-230070 from the Advanced Cyberinfrastructure Coordination Ecosystem: Services & Support (ACCESS) program, which is supported by the National Science Foundation (grants 2138259, 2138286, 2138307, 2137603, and 2138296).

Supporting Information.

	YHOTP	Y_6HOTP_2
Chemical Formula	$Y_{1.17}(C_{18}H_6O_6)(H_2O)_{1.17}$	$Y_6(CO_3)(C_{18}H_6O_6)_2(H_2O)_6Cl_6$
Node SBU	$YO_6(H_2O) = [Y]^{3+}$	$Y_6O_{12}(CO_3)(H_2O)_6(Cl)_6 = [Y_6]^{10+}$
Linker SBU	$C_{18}H_6O_6 = [HOTP]^{3-}$	$C_{18}H_6O_6 = [HOTP]^{5-}$
Chemical Composition	$Y_{1.17}C_{18}H_{8.34}O_{7.17}$	$Y_6C_{37}H_{12}O_{21}Cl_6$
Crystal System	Hexagonal	Cubic
Space Group	P6cc (no. 184)	Fd-3m (no. 227)
a (Å)	21.901	34.548
b (Å)	21.901	34.548
c (Å)	6.1825	34.548
α (°)	90	90
β (°)	90	90
γ (°)	120	90
Density (mL g^{-1})	1.15	0.99
Network Connectivity	3D	3D
Pore Connectivity	1D	3D

Table S1. Structural models for YHOTP and Y_6HOTP_2. Coordinated water molecules (identified as one-sided O atoms in single-crystal studies) are included. Charge balance is indicated based on EPR results.

	Y_6HOTP_2
Empirical Formula	$Y_6C_{37}H_{12}O_{21}Cl_6$
Formula Weight	1538.64
Temperature (K)	100
Crystal System	Cubic
Space Group	Fd-3m
a (Å)	34.548(6)
b (Å)	34.548(6)
c (Å)	34.548(6)
α (°)	90
β (°)	90
γ (°)	90
V (Å^3)	41235(2)
Z	16
Density (g mL^{-1})	0.9914
F(000)	126888
μ (mm^{-1})	7.475
Radiation	Cu Kα (λ = 1.54184 Å)
2θ range (°)	4.43–158.724
Reflections collected	151190

Table S2. Single-crystal XRD structure refinement of Y6HOTP2.

	Y	C	N	O	Cl
Y_6HOTP_2	7.5	32.1	4.5	50.9	5.0
YHOTP	3.1	44.8	1.1	50.3	0.7

Table S3. Chemical composition of YHOTP and Y6HOTP2 (in at%, excluding H) determined by combustion analysis (C, N), inductively-coupled plasma (ICP) analysis (Y, Cl), and the difference (O).

	Y	C	N	O	Cl
Y_6HOTP_2	8.6	52.9	0.0	30.0	8.6
YHOTP	4.4	68.3	0.0	27.2	0.0

Table S4. Model chemical composition of YHOTP and Y6HOTP2 (in at%, excluding H) based on the combined experimental analyses: XPS, CHN, ICP-OES, and XRD.

	Y	C	N	O	Cl
$YCl_3 \cdot 6H_2O$	8.1	39.1	0.0	32.0	20.8

Table S6. Chemical composition of YCl3·6H2O (in at%) determined by energy dispersive X-ray spectroscopy (EDX) using a 10 kV accelerating voltage.

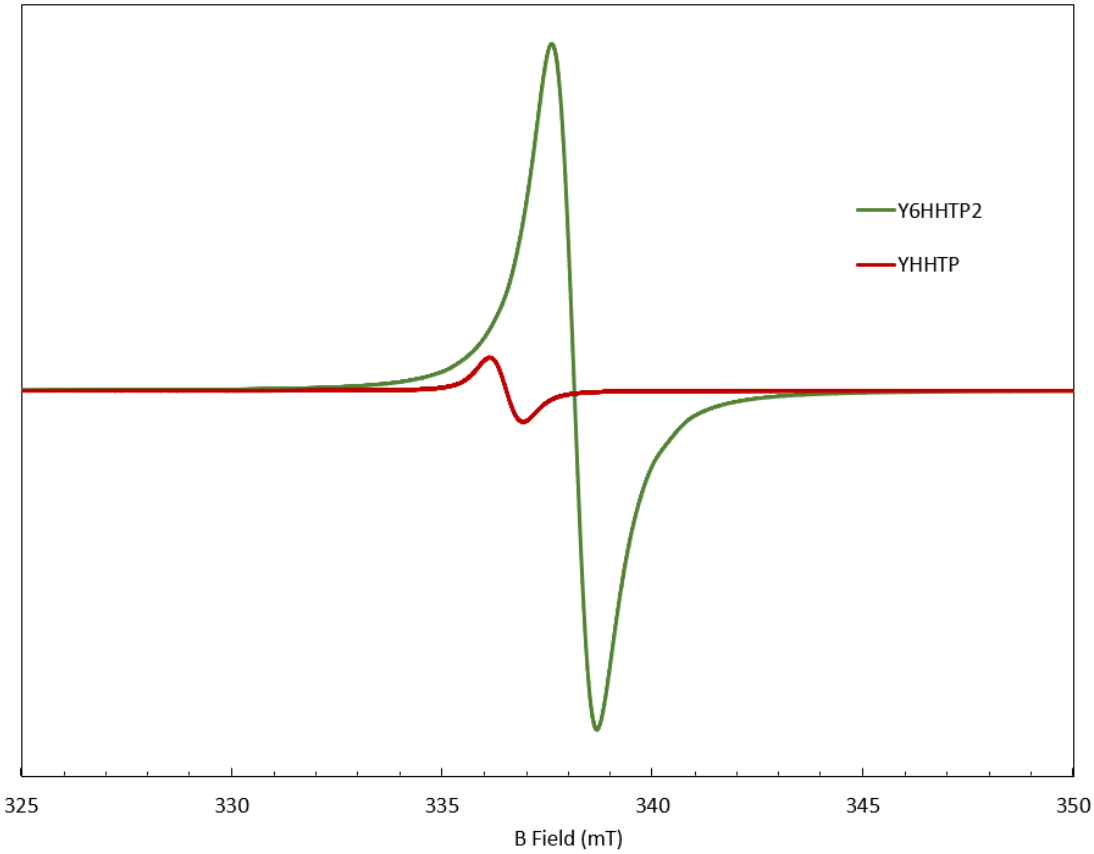

Figure S1. EPR spectra of YHOTP and Y6HOTP2 between 325-350 mT, normalized by mass.

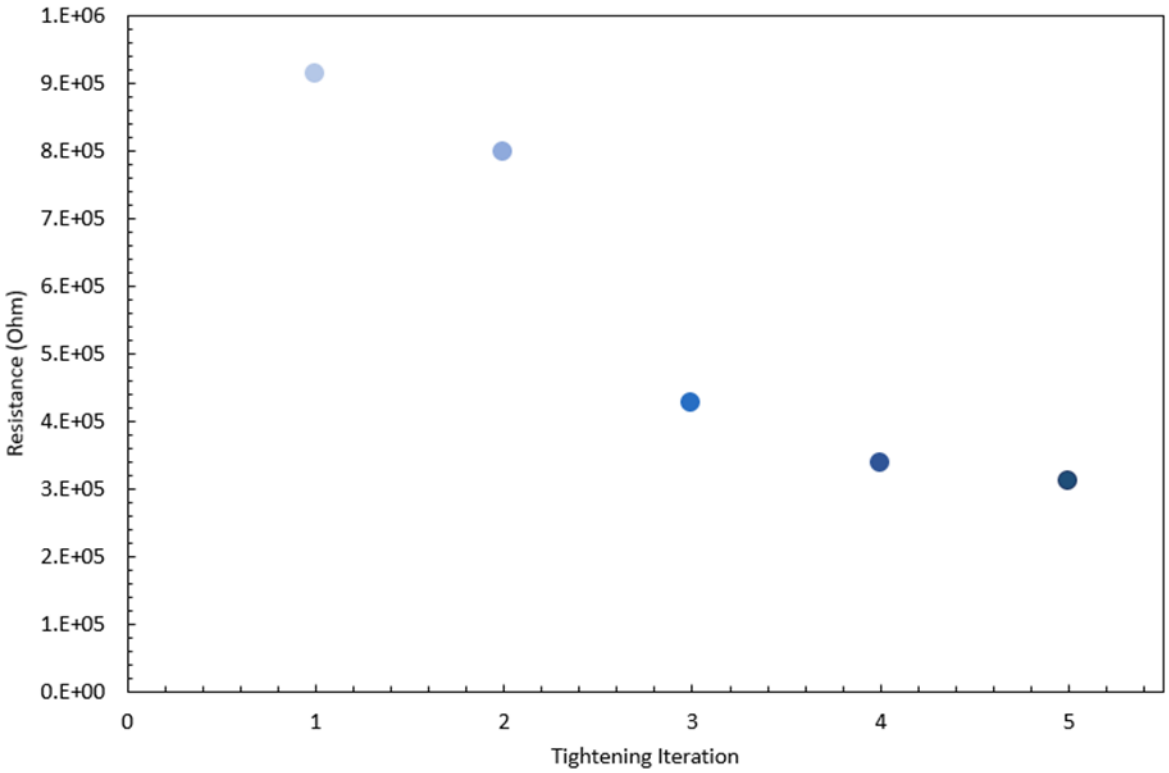

Figure S2. Iterative two-point probe measurements of packed pellet resistance of YHOTP (I-V curve swept from -1.0 to 1.0 V), upon hand tightening between measurements.

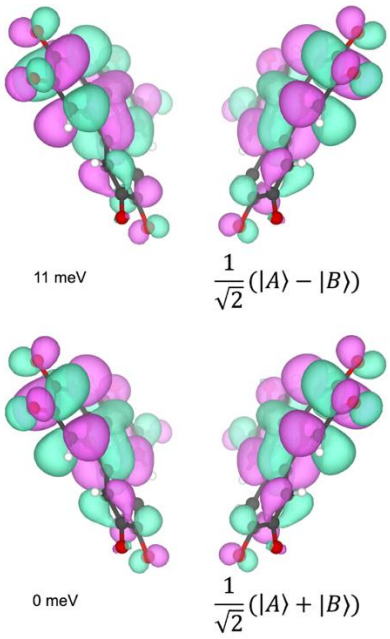

Figure S3. Molecular orbitals of HOTP placed at positions consistent with Y6HOTP2, consisting of symmetric (bottom) and antisymmetric (top) combinations of the individual linker molecular orbitals. The antisymmetric state is higher in energy, suggesting J-like aggregation behavior.

References

(1) Li, C.; Zhang, L.; Chen, J.; Li, X.; Sun, J.; Zhu, J.; Wang, X.; Fu, Y. Recent Development and Applications of Electrical Conductive MOFs. Nanoscale 2021, 13 (2), 485-509

(2) Hendon, C. H.; Rieth, A. J.; Korzynski, M. D.; Dincă, M. Grand Challenges and Future Opportunities for Metal-Organic Frameworks. ACS Cent. Sci. 2017, 3 (6), 554-563

(3) Syzgantseva, M. A.; Stepanov, N. F.; Syzgantseva, O. A. Band Alignment as the Method for Modifying Electronic Structure of Metal-Organic Frameworks. ACS Appl. Mater. Inter. 2020, 12 (15), 17611-17619

(4) Hua, C.; Doheny, P. W.; Ding, B.; Chan, B.; Yu, M.; Kepert, C. J.; D'Alessandro, D. M. Through-Space Intervalence Charge Transfer as a Mechanism for Charge Delocalization in Metal-Organic Frameworks. J. Am. Chem. Soc. 2018, 140 (21), 6622-6630

(5) Xie, L. S.; Skorupskii, G.; Dincă, M. Electrically Conductive Metal–Organic Frameworks. Chem. Rev. 2020, 120 (16), 8536-8580

(6) Wang, H. F.; Chen, L.; Pang, H.; Kaskel, S.; Xu, Q. MOF-Derived Electrocatalysts for Oxygen Reduction, Oxygen Evolution and Hydrogen Evolution Reactions. Chem. Soc. Rev. 2020, 49 (5), 1414-1448

(7) Jin, S. How to Effectively Utilize MOFs for Electrocatalysis. ACS Energy Lett. 2019, 4 (6), 1443-1445

(8) Liu, J.; Zhu, D.; Guo, C.; Vasileff, A.; Qiao, S. Z. Design Strategies toward Advanced MOF-Derived Electrocatalysts for Energy-Conversion Reactions. Adv. Energy Mater. 2017, 7 (23), 1-26

(9) Zhang, H.; Liu, X.; Wu, Y.; Guan, C.; Cheetham, A. K.; Wang, J. MOF-Derived Nanohybrids for Electrocatalysis and Energy Storage: Current Status and Perspectives. Chem. Commun. 2018, 54 (42), 5268-5288

(10) Tahir, M. A., Arshad, N., & Akram, M. Recent Advances in Metal Organic Framework (MOF) as Electrode Material for Super Capacitor: A Mini Review. J. of Energy Storage 2022, 47, 103530

(11) Sheberla, D.; Bachman, J. C.; Elias, J. S.; Sun, C. J.; Shao-Horn, Y.; Dincă, M. Conductive MOF Electrodes for Stable Supercapacitors with High Areal Capacitance. Nat. Mater. 2017, 16 (2), 220-224

(12) Maiti, S., Pramanik, A., Dhawa, T., Sreemany, M., & Mahanty, S. Bi-Metal Organic Framework Derived Nickel Manganese Oxide Spinel for Lithium-Ion Battery Anode. Mater. Sci. & Eng. B. 2018, 229, 27–36

(13) Song, W.; Teng, X.; Liu, Y.; Wang, J.; Niu, Y.; He, X.; Zhang, C.; Chen, Z. Rational Construction of Self-Supported Triangle-Like MOF-Derived Hollow (Ni,Co)Se2 Arrays for Electrocatalysis and Supercapacitors. Nanoscale 2019, 11 (13), 6401-6409

(14) Park, J. G.; Aubrey, M. L.; Oktawiec, J.; Chakarawet, K.; Darago, L. E.; Grandjean, F.; Long, G. J.; Long, J. R. Charge Delocalization and Bulk Electronic Conductivity in the Mixed-Valence Metal-Organic Framework Fe(1,2,3-Triazolate)2(BF4)x. J. Am. Chem. Soc. 2018, 140 (27), 8526-8534

(15) Diamond, B. G.; Payne, L. I.; Hendon, C. H. Ligand Field Tuning of D-Orbital Energies in Metal-Organic Framework Clusters. Commun. Chem. 2023, 6 (1), 67-73

(16) Hmadeh, M.; Lu, Z.; Liu, Z.; Gándara, F.; Furukawa, H.; Wan, S.; Augustyn, V.; Chang, R.; Liao, L.; Zhou, F.; et al. New Porous Crystals of Extended Metal-Catecholates. Chem. Mater. 2012, 24 (18), 3511-3513

(17) Park, G.; Demuth, M. C.; Hendon, C. H.; Park S. S. Acid-Dependent Charge Transport in a Solution-Processed 2D Conductive Metal-Organic Framework. J. Am. Chem. Soc. 2024, 146 (16), 11493-11499

(18) Apostol, P.; Gali, S. M.; Su, A.; Tie, D.; Zhang, Y.; Pal, S.; Lin, X.; Bakuru, V. R.; Rambabu, D.; Beljonne, D.; Dincă, M.; Vlad, A. Controlling Charge Transport in 2D Conductive MOFs─The Role of Nitrogen-Rich Ligands and Chemical Functionality. J. Am. Chem. Soc. 2023 145 (45), 24669-24677

(19) Lu, Y.; Zhang, Y.; Yang, C. Y.; Revuelta, S.; Qi, H.; Huang, C.; Jin, W.; Li, Z.; Vega-Mayoral, V.; Liu, Y.; Huang, X.; Pohl, D.; Položij, M.; Zhou, S.; Cánovas, E.; Heine, T.; Fabiano, S.; Feng, X.; Dong, R.; Precise tuning of interlayer electronic coupling in layered conductive metal-organic frameworks. Nat. Commun. 2022, 13, 7240

(20) Debela, T. T.; Yang, M. C.; Hendon, C. H. Ligand-Mediated Hydrogenic Defects in Two-Dimensional Electrically Conductive Metal-Organic Frameworks. J. Am. Chem. Soc. 2023, 145 (20), 11387-11391

(21) Day, R. W.; Bediako, D. K.; Rezaee, M.; Parent, L. R.; Skorupskii, G.; Arguilla, M. Q.; Hendon, C. H.; Stassen, I.; Gianneschi, N. C.; Kim, P.; et al. Single Crystals of Electrically Conductive Two-Dimensional Metal-Organic Frameworks: Structural and Electrical Transport Properties. ACS Cent. Sci. 2019, 5 (12), 1959-1964

(22) Nam, K. W.; Park, S. S.; Dos Reis, R.; Dravid, V. P.; Kim, H.; Mirkin, C. A.; Stoddart, J. F. Conductive 2D Metal-Organic Framework for High-Performance Cathodes in Aqueous Rechargeable Zinc Batteries. Nat. Commun. 2019, 10 (1), 4948

(23) Clough, A. J.; Skelton, J. M.; Downes, C. A.; de la Rosa, A. A.; Yoo, J. W.; Walsh, A.; Melot, B. C.; Marinescu, S. C. Metallic Conductivity in a Two-Dimensional Cobalt Dithiolene Metal-Organic Framework. J. Am. Chem. Soc. 2017, 139 (31), 10863-10867

(24) Sheberla, D.; Sun, L.; Blood-Forsythe, M. A.; Er, S.; Wade, C. R.; Brozek, C. K.; Aspuru-Guzik, A.; Dincă, M. High Electrical Conductivity in Ni3(2,3,6,7,10,11-Hexaiminotriphenylene)2, a Semiconducting Metal-Organic Graphene Analogue. J. Am. Chem. Soc 2014, 136 (25), 8859-8862

(25) Skorupskii, G.; Trump, B. A.; Kasel, T. W.; Brown, C. M.; Hendon, C. H.; Dincă, M. Efficient and Tunable One-Dimensional Charge Transport in Layered Lanthanide Metal-Organic Frameworks. Nat. Chem. 2020, 12 (2), 131-136

(26) Skorupskii, G.; Dincă, M. Electrical Conductivity in a Porous, Cubic Rare-Earth Catecholate. J. Am. Chem. Soc. 2020, 142 (15), 6920-6924

(27) Nath, A.; Kumar, V.; Shukla, A.; Ghosh, H. N.; Mandal, S. Influence of Molecular Separation on through-Space Intervalence Transient Charge Transfer in Metal-Organic Frameworks with Cofacially Arranged Redox Pairs. Angew. Chem. Int. Ed. 2023, 62 (31), e202308034

(28) Kirkpatrick, J. An Approximate Method for Calculating Transfer Integrals Based on the Zindo Hamiltonian. Int. J. Quantum Chem. 2007, 108 (1), 51-56

(29) Gaussian 09, Revision A.02; 2016.

(30) J.-L. Bredas, D. Beljonne, V. Coropceanu, J. Cornil. Charge-Transfer and Energy-Transfer Processes in π-Conjugated Oligomersand Polymers: A Molecular Picture. Chem. Rev. 2004, 104 (11), 4887-5782

(31) Hsu, C.-P. The Electronic Couplings in Electron Transferand Excitation Energy Transfer. Acc. Chem. Res. 2009, 489-573

(32) Demuth, M. C.; Hendon, C. H. Linker Aromaticity Reduces Band Dispersion in 2D Conductive Metal–Organic Frameworks. ACS Mater. Lett. 2023, 5 (5), 1476-1480

(33) Sun, L.; Park, S. S.; Sheberla, D.; Dincă, M. Measuring and Reporting Electrical Conductivity in Metal-Organic Frameworks: Cd2(TTFTB) as a Case Study. J. Am. Chem. Soc. 2016, 138 (44), 14772-14782

(34) G. Kresse, J. F. Efficiency of Ab-Initio Total Energy Calculations for Metals and Semiconductors Using a Plane-Wave Basis Set. Comput. Mater. Sci. 1996, 6 (1), 15-50

(35) Schimka, L.; Harl, J.; Kresse, G. Improved Hybrid Functional for Solids: The HSEsol Functional. J. Chem. Phys. 2011, 134 (2), 024116

CHAPTER FIVE

TOPOLOGY-DEPENDENT MECHANISMS OF LI-, NA-, AND K-ION INSERTION IN 2D AND 3D ZEOLITE-TEMPLATED CARBONS

Contribution of Authors and Co-Authors

Manuscript in Chapter 5

Author: Connor Welty

Contributions: Characterized materials, fabricated electrodes, collected data, analyzed data, produced figures, and wrote the manuscript.

Co-Author: Chaehoon Kim

Contributions: Synthesized and characterized material, provided intellectual advice.

Co-Author: Minkee Choi

Contributions: Synthesized and characterized material, provided intellectual advice.

Co-Author: Nicholas P. Stadie

Contributions: Advised with the experimental direction, interpreted results, and assisted in writing and editing the manuscript.

Manuscript Information

Connor Welty, Chaehoon Kim, Minkee Choi, and Nicholas P. Stadie

Status of Manuscript:
☒ Prepared for submission to a peer-reviewed journal
☐ Officially submitted to a peer-reviewed journal
☐ Accepted by a peer-reviewed journal
☐Published in a peer-reviewed journal

Abstract

Carbonaceous materials with uniform pore structures and tunable π-stacking character provide ideal models for understanding ion storage mechanisms. Zeolite-templated carbons (ZTCs) are high-fidelity topological replicates of the zeolite in which they are synthesized, exhibiting an ordered framework connectivity determined by the pore connectivity of the zeolite template. In this study, a 2D-connected ZTC based on **IWV** zeolite as the template was compared to a 3D-connected ZTC based on **FAU** zeolite as the template. The "2D ZTC" is comprised of atomistically thin graphene-like sheets with an ordered array of ~1.2 nm holes ("pores") that collapse into random π-stacked structures upon removal of the zeolite, while the "3D ZTC" contains exclusively ~1.2 nm pores enclosed by an ordered network of graphene ribbons and no π-stacking. Electrochemical insertion of Li-, Na-, and K-ions into these model porous carbons revealed the effects of pore structure and stacking character on ion diffusion/resistance behavior. While the permanently porous 3D ZTC structure exhibits excellent ion storage capacity and kinetics toward Li^+, the unique stacked and porous structure of 2D ZTC permits rapid, high-density storage of Na^+ and K^+. An asymmetrical hybrid capacitor (HC) based on 2D/3D ZTC for dual-ion $NaPF_6$ storage is presented which achieves up to 72 Wh kg^{-1} and up to 9.9 kW kg^{-1} at the device level, harnessing the benefits of both porous structure types.

Introduction

Zeolite-templated carbons (ZTCs) are ordered porous carbon framework materials that have designable pore size and structural connectivity based on the zeolite template chosen.[1] Comprised of continuous networks of exclusively sp^2-hybridized carbon, ZTCs have numerous

properties that make them attractive as active materials for Li-ion batteries (LIBs), Na-ion batteries (NIBs), and K-ion batteries (KIBs): ultrahigh electrical conductivity[2], high ionic conductivity[3], light weight, and a large pore space available for ion storage. As an anode in standard liquid-electrolyte LIBs, however, the major drawback to the deployment of ZTCs is the same as for any high-surface-area porous carbon: large irreversible capacity in the first cycle due to solid-electrolyte interphase (SEI) formation at low potentials.[4] On the contrary, ZTCs have proven as excellent cathode materials in several applications (especially in chloroaluminate-based aluminum chemistries[5], for Mg^{2+} storage in several magnesium chemistries[6], and for FSI^- storage in dual-ion KIBs[7]) owing to the higher potentials of insertion subject to the positive electrode of such cells. Thus, the promising attributes of ZTCs as active electrode materials in high energy density electrochemical cells can be realized when the appropriate electrochemical conditions are employed.

Almost all previous work using ZTC as an active ion storage material has focused on the archetypical variant, derived from a faujasite-type (**FAU**) zeolite; such ZTCs exhibit exclusively nanometer-scale porosity and inherently do not exhibit stacking structure (making them purely capacitive), a direct result of the 3D-connected pore space of **FAU** zeolites. Thus, such materials have served as important model materials in contrast to graphite and other dense electrode materials since no intercalation or interlayer-type interactions of any kind occur in **FAU**-ZTCs.[8] More generally, however, zeolites as a class are diverse porous aluminosilicate framework materials with arbitrary porous connectivity, including both 1D- and 2D-connected channels.[9] When a zeolite template is impregnated with a hydrocarbon precursor, carbon–carbon bond formation is permitted only in the molecularly accessible channels, and upon dissolving the

zeolite a porous carbonaceous framework can be extracted that reflects the same connectivity (network topology) as the zeolite porosity.[10] If a zeolite with 3D pore connectivity (like **FAU**) is used, a 3D-connected framework results; however, if a zeolite with 2D pore connectivity (like **IWV**, where the reference material is known as ITQ-27[11]), a series of disconnected carbonaceous sheets will result, comprised of an ordered array of "pores" (i.e., holes) and stacked into weakly ordered layers as a result of van der Waals interactions.[12] Hence, a "2D ZTC" exhibits a drastically different distribution of binding sites and therefore altered desolvation and charge transfer processes when compared to a "3D ZTC", while still maintaining an ordered porosity.

In this work, we systematically investigate a 2D ZTC templated from an **IWV** zeolite in comparison to a standard 3D ZTC templated from an **FAU** zeolite. We find that the disordered stacking structure of 2D ZTC, punctuated by molecularly accessible pores, permits the storage of Li^+, Na^+, and K^+ at ultrafast current rates up to 30 A g^{-1} (i.e., <1 min charging time). The charge storage mechanism of 2D ZTC consists of both intercalation (such as in graphite and hard carbon) and capacitive adsorption (as in 3D ZTC), occurring at the redox-active oxygen functional groups on the edges of the carbon framework.[13] These active sites have been shown to contain both furan-type ethers and quinone-type functional groups that, in large number, can present with characteristic electrochemical signatures of pseudocapacitance.[14, 15] Crucially, these sites are partially protected from exposure to the electrolyte and therefore 2D ZTC can serve as a viable anode compared to 3D ZTC. Since this mechanism of ion storage differs from traditional pseudocapacitance such as in transition metal oxides (TMOs)[16], we apply the term "quasicapacitance" herein, referring to the partial extent of ion desolvation involved.[17] This intermediate charge storage mechanism is especially suited to Na^+ storage and a full-cell hybrid

capacitor is presented that benefits from the relative stability of 2D ZTC as the anode and the high capacity and rate capability of 3D ZTC as the cathode.

Experimental Methods

Materials Synthesis

2D ZTC was prepared as recently described elsewhere.[12] 3D ZTC was prepared according to the established two-step method[18-19] via liquid impregnation of zeolite NaY with furfuryl alcohol at low temperature and then chemical vapor deposition of propylene at 700 °C; after heat treatment at 900 °C, the zeolite template was removed upon repeated dissolution in aqueous HF. The synthesis of 3D ZTC is described in detail elsewhere.[20]

Materials Characterization

Powder X-ray diffraction (XRD) measurements were performed using a Bruker D8 Advance diffractometer with Cu $K\alpha_{1,2}$ radiation (λ = 1.54 Å) in reflection geometry. Nitrogen adsorption/desorption isotherms were measured at 77 K between 10^{-4}-100 kPa using an automated volumetric instrument (3Flex, Micromeritics Instrument Corp.). Specific surface areas were calculated using the Brunauer-Emmett-Teller (BET) method between $P/P_0 = 4\times10^{-6}$-0.11 and micropore volumes were calculated using the Dubinin-Radushkevich (DR) method. Pore-size distributions were determined by non-localized density functional theory (NLDFT) calculations with a carbon slit-pore model (using MicroActive Share software, Micromeritics Instrument Corp.). Electrical conductivity was measured via a 2-point probe technique on pressed powders using a custom apparatus, as described elsewhere.[21] Five replicate measurements were performed for each material and averaged. Elemental analysis (C, H, and O)

was performed in triplicate using flame combustion (Atlantic Microlab Inc.) and converted from weight percent (wt%) to atomic percent (at%) post-analysis.

Electrochemical Cell Materials

The following materials were used in the preparation of electrochemical cells: ethylene carbonate (EC, battery grade, BASF), dimethyl carbonate (DMC, battery grade, BASF), lithium hexafluorophosphate ($LiPF_6$, 98%, Sigma Aldrich), sodium hexafluorophosphate ($NaPF_6$, 99%, Sigma Aldrich), potassium hexafluorophosphate (KPF_6, 99%, Sigma Aldrich), lithium chips (99.9%, MTI), sodium chips (99.7%, MSE Supplies Inc.), potassium metal (99.97%, Sigma Aldrich), carbon black (Super P, Timcal Ltd.), polyvinylidene fluoride (PVDF, 99.5%, MTI Corp.), N-methyl-2-pyrrolidone (NMP, 99.0%, Sigma-Aldrich), copper foil (thickness: 9 μm, MTI Corp.), and glass microfiber discs (0.67 × 257 mm, GF/D grade, 1823-257, Whatman). Synthetic graphite (282863, nominal particle size: <20 μm, Sigma-Aldrich), referred to elsewhere as "AG20"[22], was used as-received as an active electrode material for comparison to 2D and 3D ZTCs under lithiation and potassiation. A hard carbon (SIB-BHC400, 7-11 μm, MTI Corp.), referred to herein as "HC", was used as-received as an active electrode material for comparison to 2D and 3D ZTCs under sodiation due to the inability of graphite to be sodiated.[23]

Electrolyte Preparation

A dual solvent carbonate-based electrolyte (EC/DMC) was chosen based on down-selection among three different solvent systems in previous studies[20]. The mixture consisted of EC and DMC in 1:1 ratio by weight, and MPF_6 as the salt (M = Li, Na, or K). The electrolyte was prepared by slowly mixing the salt into a stock solution of EC/DMC under inert Ar

atmosphere (< 0.1 ppm H_2O/O_2). The reported electrolyte concentration is the nominal concentration based on the initial volume of the solvent, not the final volume.

Electrode Fabrication

Working electrodes were prepared by mixing one of the active materials (80 wt%) with Super P (10 wt%) and PVDF as the binder (10 wt%), and then forming a slurry in NMP (e.g., ~400 μL per 200 mg batch). After grinding by hand for 20 min, the slurry was cast onto Cu foil using a doctor blade, air-dried at 80 °C for 12 h, and then transferred to a vacuum oven and further dried at 100 °C for an additional 12 h. Homogenous loadings were achieved (1.5-2.0 mg cm^{-2}), punched into discs (⌀ 10 mm), and stored in an Ar-filled glovebox (<0.1 ppm H_2O/O_2).

Electrochemical Cell Preparation

Stainless-steel coin cells (316 stainless steel, size 2032, Xiamen AOT Electronics Technology Co.) were assembled in an Ar-filled glovebox in half-cell configuration using the above-prepared electrodes as the cathodes. A metal chip or flattened disc (⌀ 16 mm) was used as the counter and reference electrode, a glass fiber disc (⌀ 16 mm) was used as the separator, and a 1 M solution of $LiPF_6$, $NaPF_6$, or KPF_6 in EC/DMC (125 μL per cell) served as the electrolyte. A stainless steel conical spring and spacer (1.0 mm thick) were used for compression.

Electrochemical Measurements

Galvanostatic charge/discharge (GCD) profiles were measured using a battery cycler (CT30001A, Landt Instruments), while the cell was held at 25.0 °C using an incubator oven (KB 53, Binder). Cyclic voltammetry (CV) was measured using a multi-channel potentiostat (VMP-3e, BioLogic). Before testing, the as-prepared cells were held at open circuit voltage (OCV) for

12 h to allow the active material to become fully wetted with electrolyte. The OCV of the cells was between 2.8-3.4 V vs. M/M^+ (M = Li, Na, or K). The measured capacity (in GCD cycling) and measured current (in CV) were normalized by the mass of the active material. GCD cycling was carried out using a two-step constant current constant voltage (CCCV) protocol to ensure that an identical time was allowed for each half-cycle (e.g., 6 min at 10C). The nominal C-rate of all materials was calculated based on the theoretical capacity of lithium in graphite (370 mAh g^{-1}) for consistency across the entire range of different materials and active ions explored herein (e.g., 3700 mA g^{-1} for the constant current step at 10C, then held at constant voltage until 6 min elapsed).

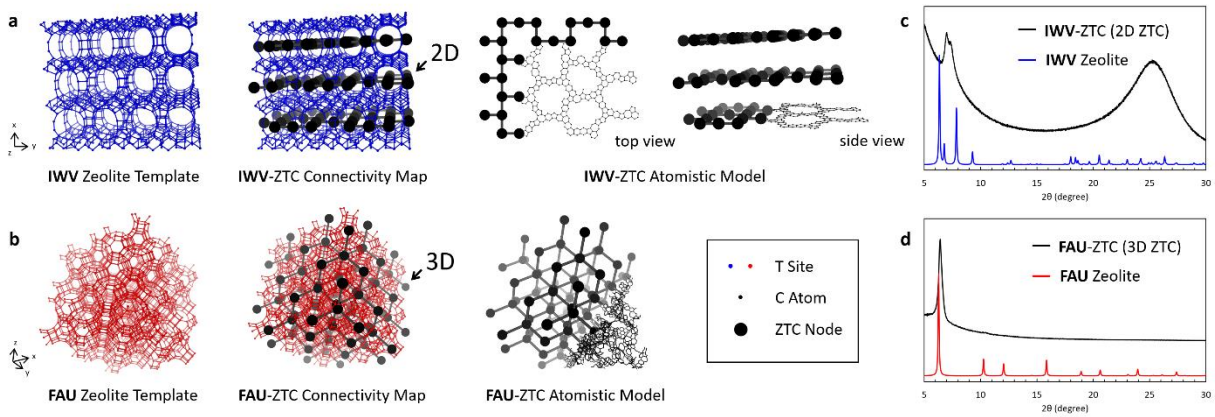

Figure 1. Synthesis schemes and structural models for (a) 2D ZTC from **IWV** zeolite and (b) 3D ZTC from **FAU** zeolite. The atomistic ZTC models are shown for schematic purposes only and hydrogen is omitted for clarity; likewise, oxygen is omitted in the zeolite structures. Powder XRD patterns of (c) 2D ZTC and (d) 3D ZTC, compared to their respective zeolite template.

Results

Materials Properties

Two topological variants of ZTC were prepared for comparison in this work, referred to herein as “2D ZTC” and “3D ZTC” based on the network connectivity of the structure (Figures

1a-1b). 2D ZTC was templated from the orthorhombic **IWV** zeolite which contains dense layers of silicate sheets along the y and z axes separated by pillars along the x axis that frame large 12-ring pores.[9] Upon templating, 2D carbon sheets with ordered windows or "pores" of ~1.2 nm width were formed (Figure 1a). Upon template dissolution, these independent sheets were left intact and freed to stack on top of each other, the dangling bonds at the edges converted into H- and O-bearing functional groups. Powder XRD of the dried product (Figure 1c) reveals a large and non-homogeneous stacking distance centered at 0.36 nm (~0.02 nm larger than graphite, on average), likely prone to rotational disorder. The in-plane pore-to-pore ordering gives rise to a pair of peaks at 6.9° and 7.4° which can be attributed to the (020) and (111) reflections, respectively, imparted by the **IWV** zeolite. The (200) reflection arising from interlayer stacking in the **IWV** zeolite (at $2\theta = 6.3°$) is missing in the 2D ZTC, owing to the collapse of the templated carbon layers into π-stacked sheets upon removal of the zeolite. Hence, N_2 adsorption uptake on **IWV**-ZTC is relatively low compared to other high-quality ZTCs,[1] corresponding to a measured gas-accessible surface area of 156 $m^2\ g^{-1}$ (see Figure S1).

3D ZTC was templated from the cubic **FAU** zeolite which contains a diamond-like network of ordered micropores framed by large 12-ring openings; hence, the resulting ZTC comprises graphene ribbon-like struts with a 3D connectivity of covalently-bonded polycyclic rings.[24] This pore-to-pore ordering gives rise to an XRD reflection at $2\theta = 6.4°$ (d = 1.38 nm) that is imparted by the (111) reflection of the FAU template (at $2\theta = 6.3°$). Hence, the 3D carbon structure remains intact and at nearly the same pore-to-pore repeat distance (slightly contracted) after removal of the zeolite. The lack of intensity at around $2\theta = 26°$ confirms the absence of any graphitic stacking in the structure of 3D ZTC. A high type-I uptake of N_2 at 77 K is indicative of

a homogeneous microporosity centered at a pore width of ~1.2 nm and a high surface area of 3330 $m^2 g^{-1}$, higher even than pristine graphene due to the significant edge character of the 3D ZTC structure. These features are highly consistent with the atomistic model of **FAU**-ZTC proposed by Nishihara and coworkers, referred to as Model II+.[24, 25]

Owing to their difference in structure, pressed powder electrical conductivities of the 2D and 3D ZTCs were measured to be significantly different: 0.3 S cm^{-1} and >16 S cm^{-1}, respectively (the measurement for 3D ZTC is at the detection limit of the two-probe device employed). This reveals significant disruption of the covalent bonding network in the bulk 2D ZTC powder, as consistent with its disordered, π-stacked structure. Meanwhile, the chemical composition of 2D and 3D ZTCs only differ slightly: 75.8%/78.1% C, 17.4%/16.5% H, and 6.8%/5.4% O for 2D/3D ZTC, respectively (measured by flame combustion methods). The large contribution from H and O content reveal a similarly dominant edge character (as opposed to extended graphene-like structure) of both ZTCs. All in all, 2D and 3D ZTCs share much in common: a disordered graphene-ribbon framework decorated with plentiful edge character and O-bearing functional groups, interrupted by a periodic network of ~1.2 nm pores. The primary difference in these two carbonaceous solids is in the 2D versus 3D network connectivity of their covalently-bonded polycyclic ring systems, leading to a disordered, layered structure in 2D ZTC that is largely inaccessible to gas (or solvent).

Electrochemical Characterization

A series of experiments were performed to explore and categorize the different electrochemical insertion mechanisms of Li^+, Na^+, and K^+ into 2D and 3D ZTC, with specific attention to the characteristic rates of each mechanism. Hence, a wide range of current/scan rates

were investigated, corresponding to charge/discharge half-cycle times from 300 minutes to as short as 45 seconds. In order to prevent the insertion of anion species into the ZTC framework, an appropriate upper voltage cutoff was enforced using voltage window opening analysis as in previous work[7] (see Supporting Information). In general, CV was performed within the reversible cation insertion window to identify and categorize electrochemical phenomena (e.g., insertion events/types) and GCD cycling was performed to quantify the capacity corresponding to each event and their rate capability and long cycling stability. A standard electrolyte system (MPF_6 in 1:1 EC/DMC, M = Li, Na, or K) was chosen across all studies due to its balance between solvation ability and viscosity.[20]

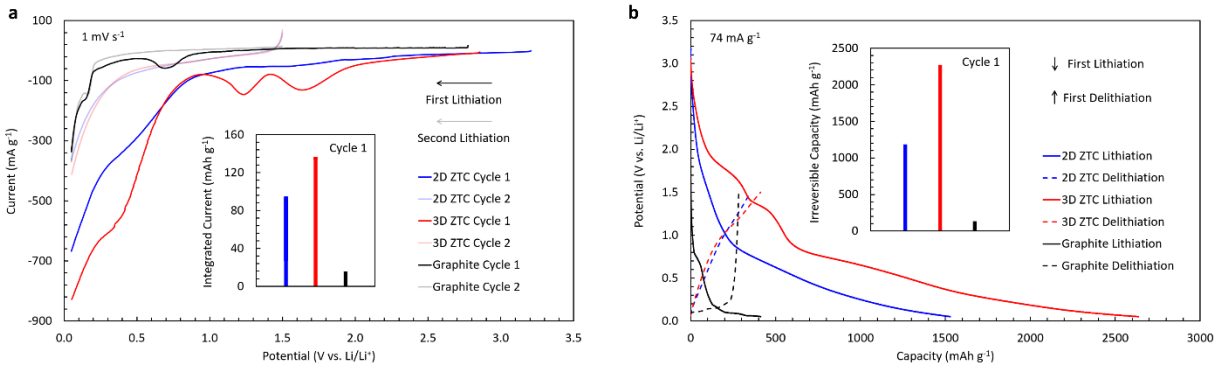

Figure 2. Early cycle electrochemical characterization of lithium insertion in 2D/3D ZTCs compared to graphite: (a) cyclic voltammetry between OCV-0.05 V vs. Li/Li^+ in the 1st half-cycle and 0.05-1.50 V vs. Li/Li^+ in the next three half-cycles at 0.1 mV s^{-1} and (b) galvanostatic charge/discharge profiles in the first cycle at 74 mA g^{-1} (0.2 C).

Table 1. Quantification of surface area and total solid-electrolyte interphase (SEI) formation on 2D/3D ZTCs compared to graphite and hard carbon (HC). Each measurement was performed in half-cell configuration between OCV-0.01-1.5 V vs. M/M^+, in 1 M MPF_6 in EC/DMC, at 0.074 mA g^{-1}.

		Li^+	Na^+	K^+	Li^+	Na^+	K^+	Li^+	Na^+	K^+
	SA_{BET} (m^2 g^{-1})	1st Cycle Discharge Q (mAh g^{-1})			1st Cycle Irreversible Q (mAh g^{-1})			Irreversible Q per SA_{BET} (mAh m^{-2})		
3D ZTC	3330	2633	1196	461	2264	1083	438	0.68	0.33	0.13
2D ZTC	156	1529	715	694	1175	610	591	7.5	3.9	3.8
Graphite	9	329	-	372	128	-	206	14	-	23
HC	4	-	370	-	-	134	-	-	34	-

Solid-Electrolyte Interphase Formation

Both 2D and 3D ZTC exhibit immense solid-electrolyte interphase (SEI) formation during the first cycle of lithiation, sodiation, or potassiation in the presence of MPF_6 dissolved in EC/DMC at low potentials (Table 1). The first cycle coulombic efficiencies were measured to be 23%, 15%, and 10% for 2D ZTC and even lower for 3D ZTC (16%, 10%, and 5%) for M = Li, Na, and K, respectively. This is a well-known effect for 3D ZTC,[4, 26] the high surface area and large number of edge-site functional groups promote a large, irreversible decomposition of the carbonate-based electrolyte.[27] Three peaks in the first cathodic scan of the cyclic voltammogram for 3D ZTC during lithiation can be attributed to SEI formation (1.65, 1.24, and 0.36 V vs. Li/Li^+, Figure 2a), corresponding to three plateaus in the first galvanostatic discharge profile (1.75, 1.35, and 0.29 V vs. Li/Li^+, Figure 2b). A fourth peak at 0.05 V vs. Li/Li^+ corresponds to Li^+ ions adsorbing on the remaining ion-binding sites on the surface of 3D ZTC. In the reversible regime (e.g., after cycle 20), the latter peak/plateau at low potential remains (though subtle) while the other three peaks have disappeared, leaving a predominantly capacitive profile.

On the other hand, 2D ZTC does not show any distinct decompositon peaks associated with SEI formation during lithiation, but rather a broad irreversible hump centered at ~0.45 V vs. Li/Li^+ on the first cathodic scan at 1 mV s^{-1} (Figure 2a). The overall first lithiation profile of 2D ZTC is similar to that underlying the distinct peaks observed for 3D ZTC, but with a lower measured current. For comparison, under the same conditions as explored for the ZTCs, graphite shows far less SEI formation but does exhibit a distinct irreversible decomposition peak at ~0.7 vs. Li/Li^+, different than any of the peaks observed for 3D ZTC. Its relatively high first cycle coulombic efficiency of 71% is typical of non-optimized half-cells such as used herein. The SEI formation observed during lithiation was exacerbated for all three materials under sodiation and potassiation due to the reduced ion pairing of Na^+ and K^+ compared to Li^+, which leads to even more decomposition of the solvation shells on the surface of the carbon frameworks (see Table S2).

At the lowest current rate explored (74 mA g^{-1}), the irreversible capacity in the first cycle for 3D ZTC is measured to be 2264, 1083, and 438 mAh g^{-1} under lithiation, sodiation, and potassiation, respectively. In surface areal terms (using the N_2-accessible BET surface area as the presumed wettable area of 3D ZTC), this corresponds to 0.68, 0.33, and 0.13 mAh m^{-2}, a direct measurement of electrochemically active surface area. By comparison (see Table 1), 2D ZTC, graphite, and hard carbon exhibit far higher active surface areas, which indicates the role of intercalation and insertion-adsorption. This also emphasizes the role for poor solvent penetration within the permanently microporous structure of 3D ZTC.

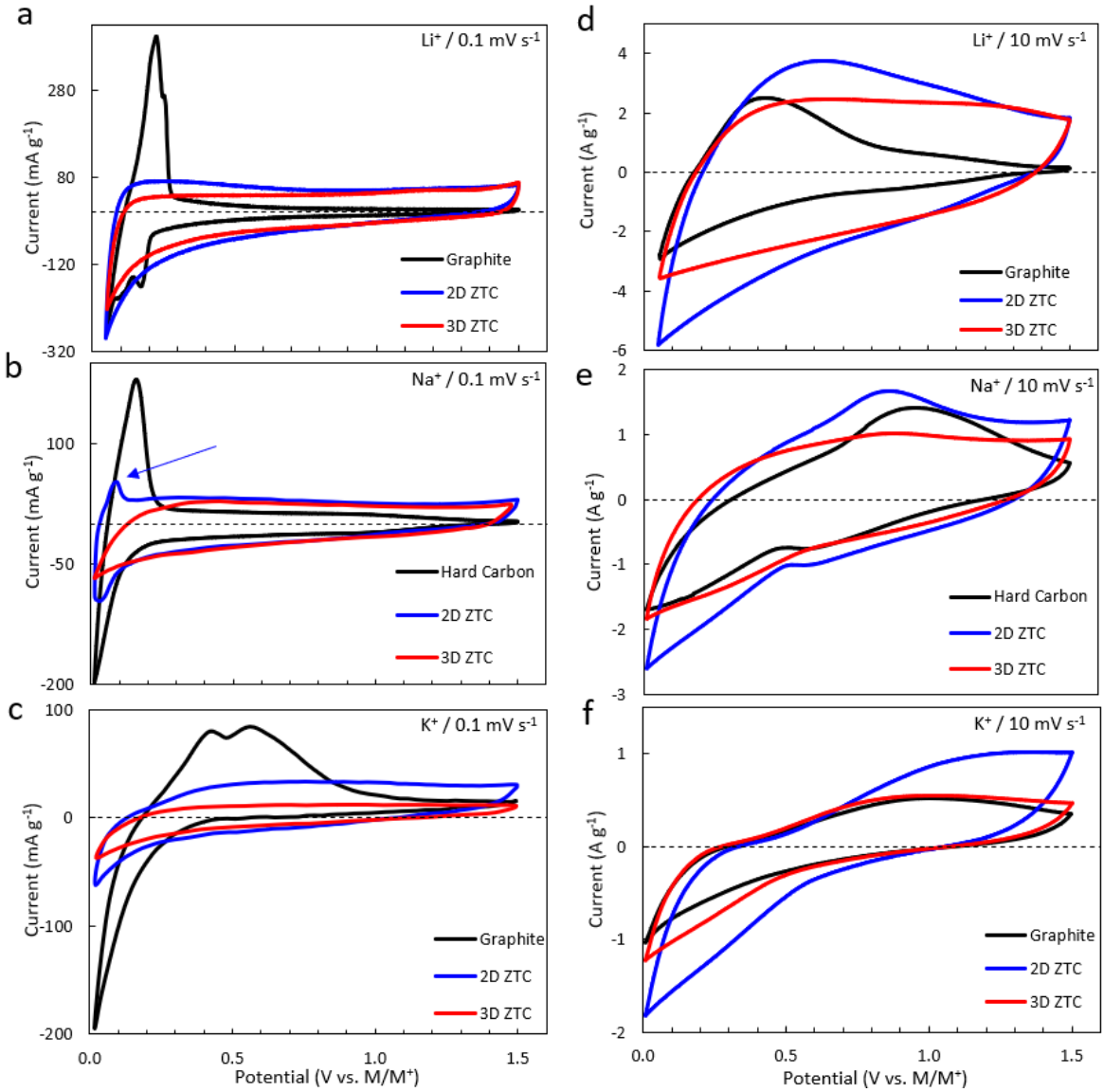

Figure 3. Cyclic voltammetry studies of reversible lithium, sodium, and potassium insertion in 2D/3D ZTCs compared to graphite and hard carbon at (a-c) 0.1 mV s-1 (~4 h per half-cycle, ~8 h per cycle) and (d-f) 10 mV s-1 (~2.5 min per half-cycle, ~5 min per cycle) between 0.05-1.50 V vs. Li/Li^+ and 0.01-1.50 V vs. Na/Na^+ and K/K^+.

Reversible Ion Insertion Mechanisms

The reversible ion insertion mechanism shows interesting topology-dependent differences between 2D and 3D ZTC, as revealed by CV studies in the reversible operation of the cell (20th

cycle and beyond, Figure 3). For 3D ZTC, the reversible CV shows a nearly potential-independent "box-like" shape across all 3 ions, with a subtle peak beginning to appear only at low potentials in the cathodic scan. This implies that all 3 ions are stored capacitively in an electric double-layer at surface sites on 3D ZTC (still accessible after the formation of SEI). A departure from pure box-like capacitive character is seen at low potentials during the reduction of 3D ZTC, owing to reversible surface redox events that must be occurring at specific functional sites.[14] Similarly, the reversible CV of 2D ZTC also shows a predominantly potential-independent shape across all 3 ions, but with the emergence of detectable anodic peaks at 0.23 V, 0.10 V, and 0.75 V for Li^+, Na^+, and K^+, respectively, at slow scan rate conditions (Figures 3a-3c). These peaks, which are very broad for both Li^+ and K^+ but pronounced for Na^+ (Figure 3b), indicate a distinct ion deinsertion mechanism from that was observed in the reversible CV of 3D ZTC. Given that the gas-accessible surface area of 2D ZTC is ~20 times smaller than that of 3D ZTC, this is indicative of intercalation of Na^+ between the layers of the 2D ZTC sheets (where gas is not accessible). A broad but distinct peak is still observed at 10 mV s^{-1} (Figure 3e), indicating that the interlayer galleries are wide enough to allow for Na^+ intercalation even at high rates. The less pronounced peaks observed for Li^+ and K^+ indicate a hybrid mechanism, i.e., only a slight charge transfer between the M^+ ion and the 2D ZTC.

Graphite and hard carbon (HC) serve as important comparison materials to 2D ZTC. Graphite shows typical intercalation/staging behavior under both lithiation and potassiation (Figures 3a and 3c) and hard carbon shows adsorption-intercalation behavior under sodiation (Figure 3b). The comparison between the CV profiles of graphite toward Li^+ and K^+ insertion is informative; even in pristine graphite, the profile broadens significantly under potassiation.

Hence, analysis of the mechanism of charge storage under potassiation via CV is fraught with complexity and caution should be used in attributing broadness to a shift toward capacitive charge storage. While graphite exhibits a distinct profile from 2D ZTC, the latter material lies intermediate between graphite and 3D ZTC in all contexts. Likewise, the insertion mechanism of Na^+ in 2D ZTC is intermediate between hard carbon and 3D ZTC. Here, the presence of a distinct anodic peak in both 2D ZTC and hard carbon can be used to assess the relative faradaic or capacitive character of the primary mechanism of sodiation via variable rate techniques.

Table 2. Reversible discharge capacity of 2D/3D ZTCs compared to graphite and hard carbon (HC). Each measurement was performed in half-cell configuration between 0.01-1.5 V vs. M/M^+, in 1 M MPF_6 in EC/DMC, after 20 cycles at the rates specified (1C = 370 mA g^{-1}, 10C = 3700 mA g^{-1}, 80C = 30,000 mA g^{-1}).

	Li^+	Na^+	K^+	Li^+	Na^+	K^+	Li^+	Na^+	K^+
	Discharge Q at 1C (mAh g^{-1})			Discharge Q at 10C (mAh g^{-1})			Discharge Q at 80C (mAh g^{-1})		
3D ZTC	200	86	28	165	77	18	135	60	8
2D ZTC	223	104	76	183	88	46	100	53	15
Graphite	326	-	91	154	-	14	53	-	5
HC	-	146	-	-	82	-	-	34	-

High Rate Reversible Ion Insertion Capacities

The ion storage capacities of 2D and 3D ZTCs were quantified across a wide range of current rates using GCD cycling under CCCV conditions (Figure 4) and a wide range of scan rates using CV (Figure 5). In general, 3D ZTC shows a box-like profile in CV between 0.1-10 mV s-1 and a linear voltage response during GCD cycling between 0.075-30 A g-1; these, in combination with a relatively stable rate capability across all ions explored, are hallmark features of capacitive ion storage. Under lithiation at the highest current rate tested (80C, 30 A g-1), 3D ZTC discharges in 45 s and stores a capacity of 135 mAh g-1 between 0.05-1.5 V vs. Li/Li+,

which corresponds to 335 F g-1 (see Equation S1). The slope of the Randles-Ševčík plot is ~1 for all three ions on 3D ZTC, but closest to 1 for lithium.

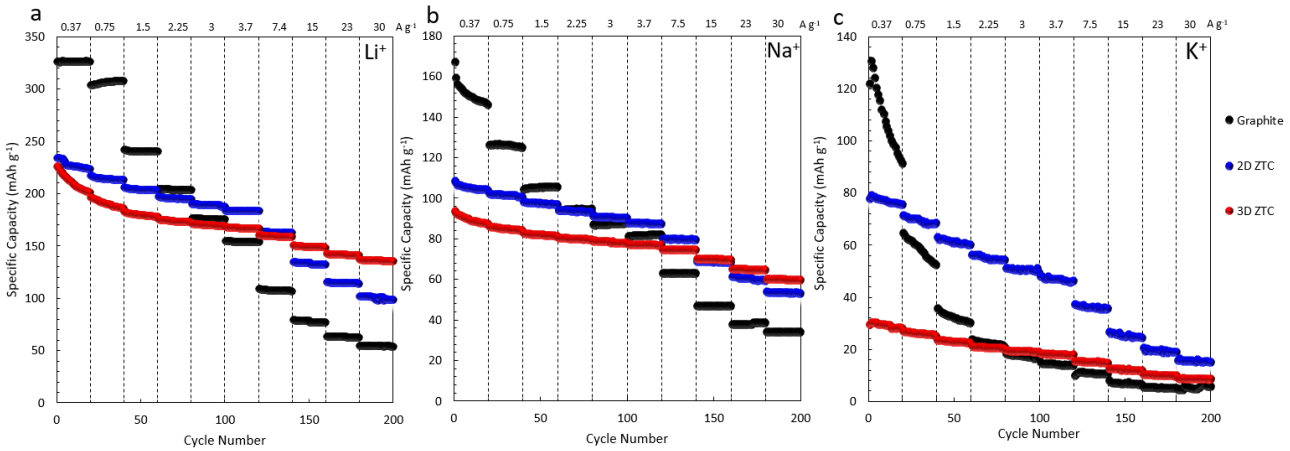

Figure 4. GCD rate capability of lithium, sodium, and potassium insertion into 2D/3D ZTCs compared to graphite and hard carbon between 0.37 to 30 A g^{-1}. All cells were cycled between 0.01-1.50 V vs. M/M^+ (M = Li, Na, or K) using a CCCV protocol.

Meanwhile, 2D ZTC also shows a mostly linear voltage response under GCD cycling with the exception of the low voltage region where (partial) faradaic charge transfer occurs. In comparison to the 3D variant, 2D ZTC shows increasing capacity retention at high rates as the cation changes from Li^+ to Na^+ and K^+. At 30 A g^{-1} 2D ZTC exhibits capacities of 100 mAh g^{-1} (243 F g^{-1}), 53 mAh g^{-1} (128 F g^{-1}), and 16 mAh g^{-1} (38 F g^{-1}) during lithiation, sodiation, and potassiation, respectively. At the same current rate, 3D ZTC lost 93% of its Li^+ capacity when cycling in the presence of K^+, whereas 2D ZTC only lost 83%. The control carbons exhibited lower capacities at 30 A g^{-1} and generally showed poor rate capability compared to 2D/3D ZTCs (see Figure 4). Converting capacity values to capacitance for graphite and hard carbon does not make sense due to their battery-like behavior.

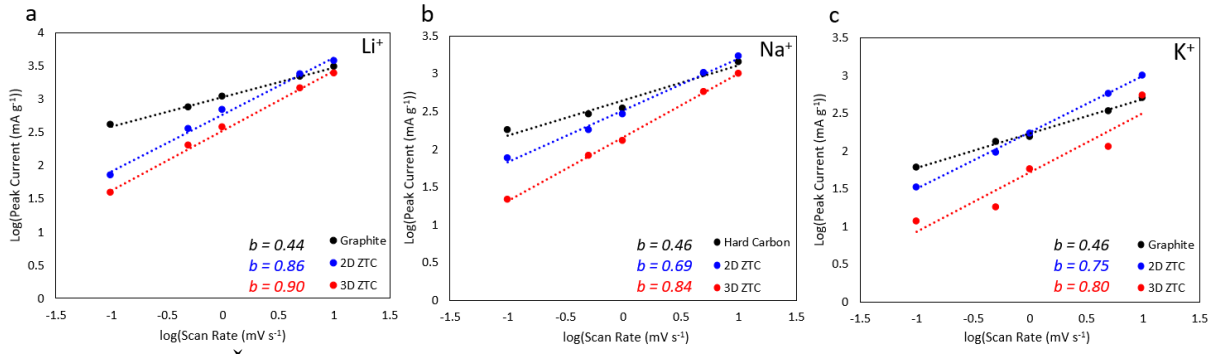

Figure 5. Randles- Ševčík Analysis of lithium, sodium, and potassium insertion into 2D/3D ZTCs compared to graphite and hard carbon between 0.1 to 10 mV s^{-1}.

Discussion

Trends in Cation Storage within 2D/3D ZTCs

The energy of desolvation is known to decrease with cation size; which influences the rate capability of each material differently. Li^+ diffuses 3 times slower than Na^+ and K^+ due to its tight coordination to the oxygen atoms on the EC molecules and therefore requires more energy to desolvate.[28] Pham et al. showed that the bond distance between the cation and the oxygen atom on the EC molecule increases from 1.95, 2.34, to 2.8 Å from Li^+, Na^+, to K^+.[29] As the electronegativity of the cation decreased the coordination number increased from 4 to 6 to 8 EC molecules. We have also shown that in bulk solution, EC and PF_6^- molecules diffuse faster when the size of the cation is larger which can be explained by reduced ion pairing.

The rate capability of 3D ZTC remained consistent as the ion size increased because its large channels and narrow pore distribution allowed solvent molecules to cointercalate. The overall capacity of 3D ZTC dropped as the ion size increased because the accessible surface area for double layer storage decreased. With intercalation dominant systems (graphite/hard carbon) the kinetic limitations of desolvation caused dramatic capacity fade as the current rate increased. Figure 4 shows that at the highest current rate (80C), graphite/hard carbon showed negligible

capacities across all 3 ions, suggesting that desolvation was unable to occur no matter how favorable the desolvation energy was. Across all 3 ions, 2D ZTC avoided the severity of the rate limiting step of desolvation that graphite suffered from. As the size of the cation increased from Li^+ to Na^+ to K^+, the rate of desolvation kinetics increased and 2D ZTC out performed 3D ZTC up to higher and higher current rates. The 3.6 Å interlayer spacing as well as the perpendicular 12 Å pores allowed large ions to diffuse quickly toward the redox sites of 2D ZTC after taking advantage of the fast desolvation step. In the LIB system, the specific capacity of 3D ZTC surpassed graphite at 6C and 2D ZTC at 10C because slow desolvation kinetics hindered the layered materials at high rates (Figure S1). In the NIB system this crossover didn't happen until 40C and in the KIB system, 2D ZTC out performed 3D ZTC throughout all of the current rates explored. This showed that because the size of the cation and therefore the rate of diffusion/desolvation increased, the layered topology of 2D ZTC became a more efficient material over the ultrahigh surface area 3D connected ZTC.

Interlayer Ion Insertion in 2D ZTC

A comparison of the N_2-accessible surface area (measured at 77 K and by employing the BET model) and the reversible ion insertion capacity allows for a prediction of the extent of ion penetration into very narrow cavities or between π-stacked layers where N_2 cannot penetrate. While the N_2 accessible surface area of 2D ZTC is only 156 $m^2\ g^{-1}$, corresponding to a theoretical surface adsorption capacity of 44 mAh g^{-1} upon lithiation (Equation S2), the measured capacity was far higher. For example, even at the ultrahigh current rate of 30 A g^{-1} (80C), the capacity was roughly 100 mAh g^{-1}. This is direct evidence that the Li^+ ions accessed interlayer surface area that was inaccessible to N_2. In comparison, 3D ZTC exhibits a surface area of xxx $m^2\ g^{-1}$ which

corresponds to a theoretical surface adsorption capacity of 945 mAh g^{-1} (far higher than the measured capacity even at low rates), suggesting that all of its capacity can be attributed to capacitive ion storage. In 2D ZTC, the diffusion limitations for interlayer insertion were minimal because of the wide gallery spacing of 2D ZTC (0.36 nm) compared to graphite (0.34 nm), this was evidenced by the peak separation in the CVs.[30] The difference between the cathodic and anodic potentials was 0.06 V for 2D ZTC in the NIB system whereas it was 0.15 V for hard carbon which means the Na^+ ions were able to deintercalate more readily in 2D ZTC. This is attributable to the presence of large, regularly-spaced interlayer pores in 2D ZTC which provide many additional ion diffusion pathways than in a narrow-spaced graphitic system.

Furthermore, this is bolstered by the distinctive shape of the cyclic voltammograms associated with ion insertion in 2D ZTC (Figure 2); an obvious low-potential redox pair is observed for 2D ZTC. This low-potential sodiation environment is absent in all of the 3D ZTC cyclic voltammograms but is clearly visible in the voltage profile of a commercial hard carbon anode material.

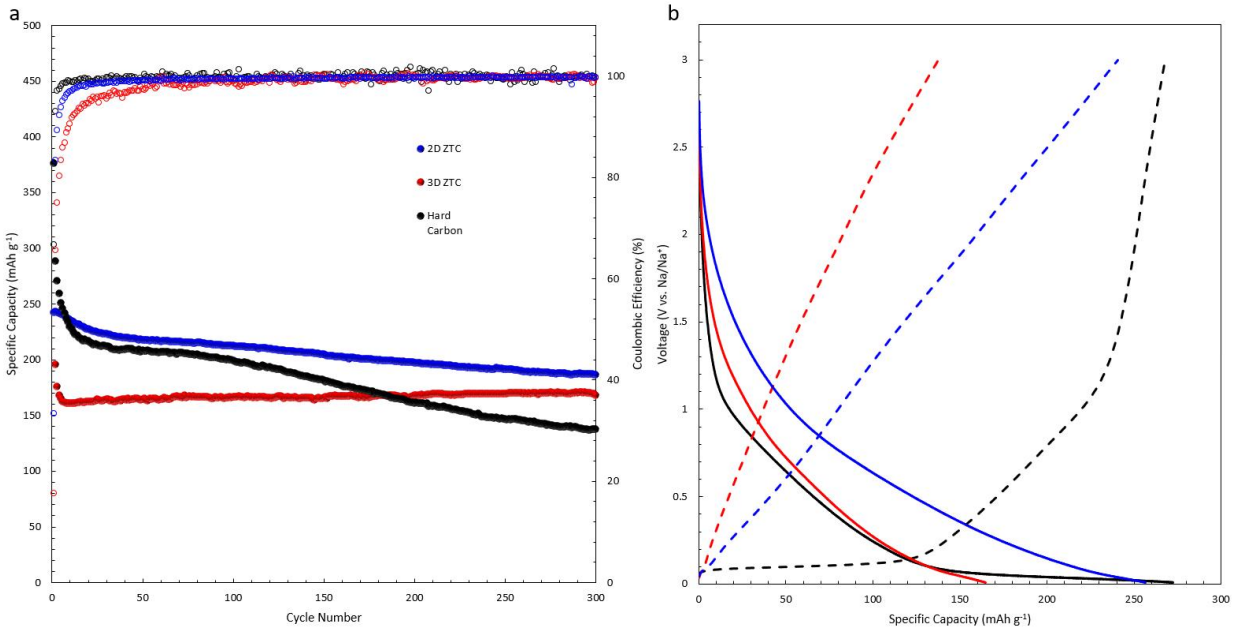

Figure 6. 2D ZTC, 3D ZTC, and Hard Carbon in optimized NIB systems. (a) 300 cycles of GCD at 100 mA g^{-1} (1.5 h up to 2.5 h) and coulombic efficiencies. (b) Voltage profiles of the 5th cycle between 0.01-3.0 V vs. Na/Na^{+}.

Structural Integrity of 2D ZTC

Optimized conditions for high energy density sodium storage in 2D ZTC, 3D ZTC, and hard carbon were investigated to highlight the strengths of 2D in this particular application (Figure 6). A benchmark current rate of 100 mA g^{-1} was employed and the voltage window was increased to between 0.01-3.0 V vs. Na/Na^{+} to maximize capacity (especially favoring the ZTC systems which exhibit appreciable capacity between 1.5-3.0 V). A capacity of >200 mAh g^{-1} was retained by 2D ZTC over 300 cycles (corresponding to 88% retention of the initial capacity). The high reversibility of ion insertion exhibited by 2D ZTC (even higher than commercial hard carbon) indicates that its layered structure is highly rigid and stable enough to withstand repeated ion insertion . This was also evidenced in rate capability investigations (Figure 4) where upon returning to 0.2 C (0.07 A g^{-1}) after cycling up to 80C (29.6 A g^{-1}), 2D ZTC retained 89%, 96%,

and 91% of its capacity under lithiation, sodiation, and potassiation, respectively. It can be inferred that the porous graphene-like layers of 2D ZTC did not experience undesirable exfoliation. Graphite and hard carbon showed reversibilities of 93%, 87%, and 72% capacity in the same systems, only superior to 2D ZTC in the case of lithiation. Potassium intercalation in graphite is known to cause irreversible damage that reduces the number of electroactive sites over cycling, but the more disordered (perhaps puckered) layers of 2D ZTC seem not to be so susceptible.

Hybrid 2D/3D ZTC Full-Cells

Owing to the impressive performance of 2D ZTC as a sodium-ion anode, a full-cell sodium-ion device was designed to take maximum advantage of both its rapid ion insertion kinetics and high sodium ion capacity. In previous work, 3D ZTC has been demonstrated to exhibit rapid, high capacity, and stable PF_6^- storage up to 4.5 V vs. Li/Li^+ (equivalent to 4.2 V vs. Na/Na^+) in standard carbonate-based organic electrolytes.[20] Hence, a dual-ion hybrid capacitor (DIHC) concept was formulated based on $NaPF_6$ as the electrolyte, 2D ZTC at the anode, and 3D ZTC at the cathode. Half-cell investigations of Na^+ storage in 2D ZTC and PF_6^- storage in 3D ZTC were used to balance the N:P ratio of the hybrid full-cell design, determined correspond to an anode:cathode mass ratio of 0.73.

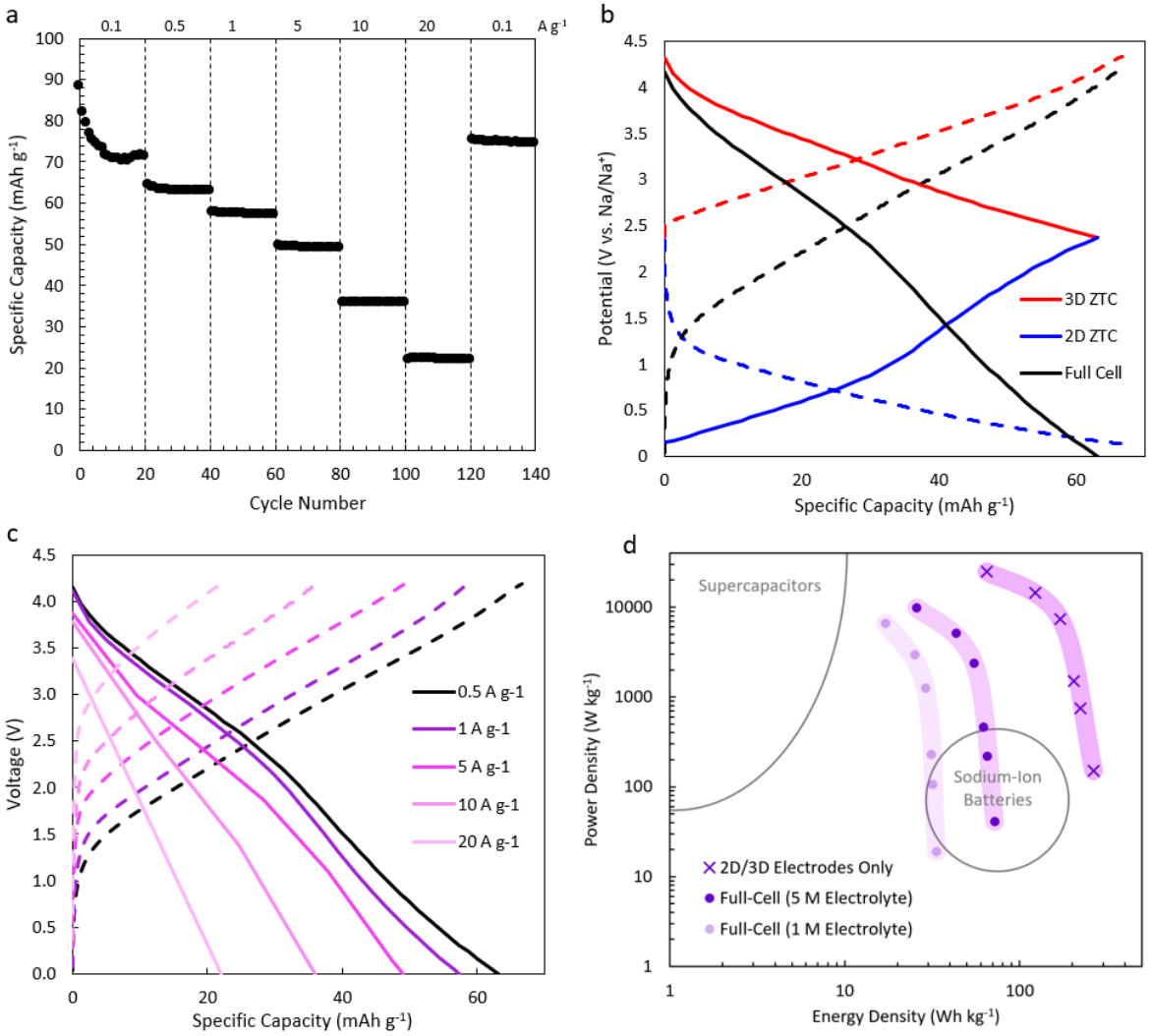

Figure 7. Electrochemical performance of dual-carbon asymmetric sodium-ion full cells with a 2D ZTC anode, 3D ZTC cathode and Na metal reference electrode. Capacities based on the mass of the anode. (a) GCD rate capability test from 0.1 to 20 A g^{-1}. (b) Voltage profiles of 2D ZTC, 3D ZTC and the full cell, cycled at 500 mA g^{-1} between 0-4.2 vs. Na/Na^{+}. (c) Voltage profiles of the last cycle at each current rate. (d) Ragone plot showing the energy/power densities of the sodium-ion cell.

Full-cell testing was performed at increasing current rates between 0.1-20 A g^{-1} (where the "per gram" refers to the mass of active anode, 2D ZTC), as shown in Figure 6. In three-electrode configuration (with sodium metal as a reference), the 2D ZTC anode was found to vary between 0.01-2.5 V vs Na/Na^{+} while the 3D ZTC cathode was found to vary between 2.5-4.2 V

vs. Na/Na^+ when the full-cell was controlled to cycle between 0.0-4.2 V (Figure 6b). These voltage windows correspond exclusively to sodium storage at the anode and PF_6^- storage at the cathode. The operating voltage window varied slightly at each electrode as the current rate increased due to the differing rate capabilities between the two materials.

The voltage profiles of the SIHC are not perfectly linear which can be ascribed to the dissimilar energy storage mechanisms happening in the anode and cathode. 2D ZTC showed a long shallow sodiation plateau below 1.5 V vs. Na/Na^+ and a disjointed but linear de-sodiation curve. 3D ZTC showed quintessential capacitive ion storage with triangular shaped voltage profiles. The SIHC maintained 36 mAh g^{-1} at 10 A g^{-1} over 20 remarkably stable cycles. Upon returning to 100 mA g^{-1} after the rate capability test, 95% of the capacity was recouped. Figure 6d displays the Ragone plot of the energy and power densities of the SIHC calculated based on a previously reported method.[7] Values for the electrode mass only as well as the full device mass are reported. Projected values for a theoretical 5 M $NaPF_6$ cell are reported.

Conclusions

In summary, we introduce a novel anode material, 2D ZTC, synthesized and templated from the IWV zeolite. We characterized the electrochemical behavior of 2D ZTC and compared it to model materials; graphite, hard carbon, and 3D ZTC. First the materials were characterized in half cell systems with a methodological increase in cation size, from Li^+ to Na^+ to K^+. The charge storage mechanisms of each ion into each material was thoroughly elucidated by GCD and CV. Na^+ was chosen as the ideal ion for storage in 2D ZTC and a cycling stability test was carried out in an optimal voltage window of 0.01-3.0 V vs Na/Na^+. 2D ZTC retained 78% of its capacity over 300 cycles. With this information, a sodium full cell was designed with 2D ZTC as

the anode and 3D ZTC as the cathode. In a wide voltage range of 0-4.2 V vs. Na/Na^+ which achieved up to 72 Wh kg^{-1} and 9.9 kW kg^{-1} at the device level. Thus, with this study, we introduce a novel and promising electrochemical system for dual-ion energy storage and provide a mechanistic understanding of the charge storage.

Associated Content

Acknowledgments

We thank Erin Taylor for synthesizing 3D ZTC and Dalton Compton for performing N_2 adsorption measurements. C.W. and N.P.S. are grateful for funding provided by the National Science Foundation (grant OIA-2034110).

Supporting Information

Equation S1. Example calculation of capacity to capacitance:

$$0.135\frac{A\cdot h}{g}\cdot\frac{3600s}{h}\cdot\frac{1}{1.45\,V}=335.2\frac{F}{g}$$

Equation S2. SA is the N2-accessible surface area of the material (in m2 g-1) and the factor 0.2839 (in mAh m-2) is the theoretical maximum capacity per unit surface area, assuming that a single-sided graphene sheet (1310 m2 g-1) can be lithiated up to 372 mAh g-1 (LiC6).

$$QA(mAh\ g^{-1}) = SA(m^2\ g^{-1}) \times 0.2839\ (mAh\ m^{-2})$$

Table S1. Surface area, initial discharge capacity, stable capacities at 4C and 80C, and reversibility of ZTCs and standard materials.

		Li	Na	K	Li	Na	K	Li	Na	K	Li	Na	K
	SBET ($m^2 g^{-1}$)	first discharge capacity (mAh g^{-1})			capacity at 4C (mAh g^{-1})			capacity at 80C (mAh g^{-1})			reversibility (%)		
3D ZTC	3330	2633	1196	461	180	82	23	135	60	8	74	84	91
2D ZTC	156	1529	715	694	203	97	53	100	53	15	88	96	91
Graphite	9	329	N/A	372	240	N/A	32	53	N/A	5	93	N/A	72
Hard Carbon	4	N/A	370	N/A	N/A	105	N/A	N/A	34	N/A	N/A	87	N/A

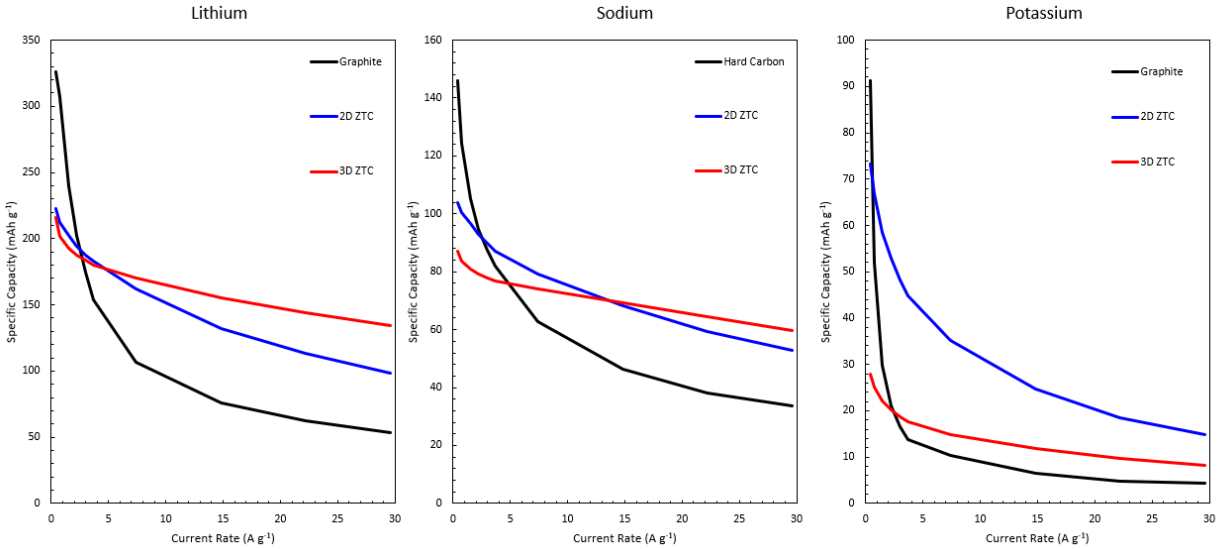

Figure S1. Specific capacities of 2D ZTC, 3D ZTC, and graphite/Hard Carbon across all 3 cations with increasing current rate.

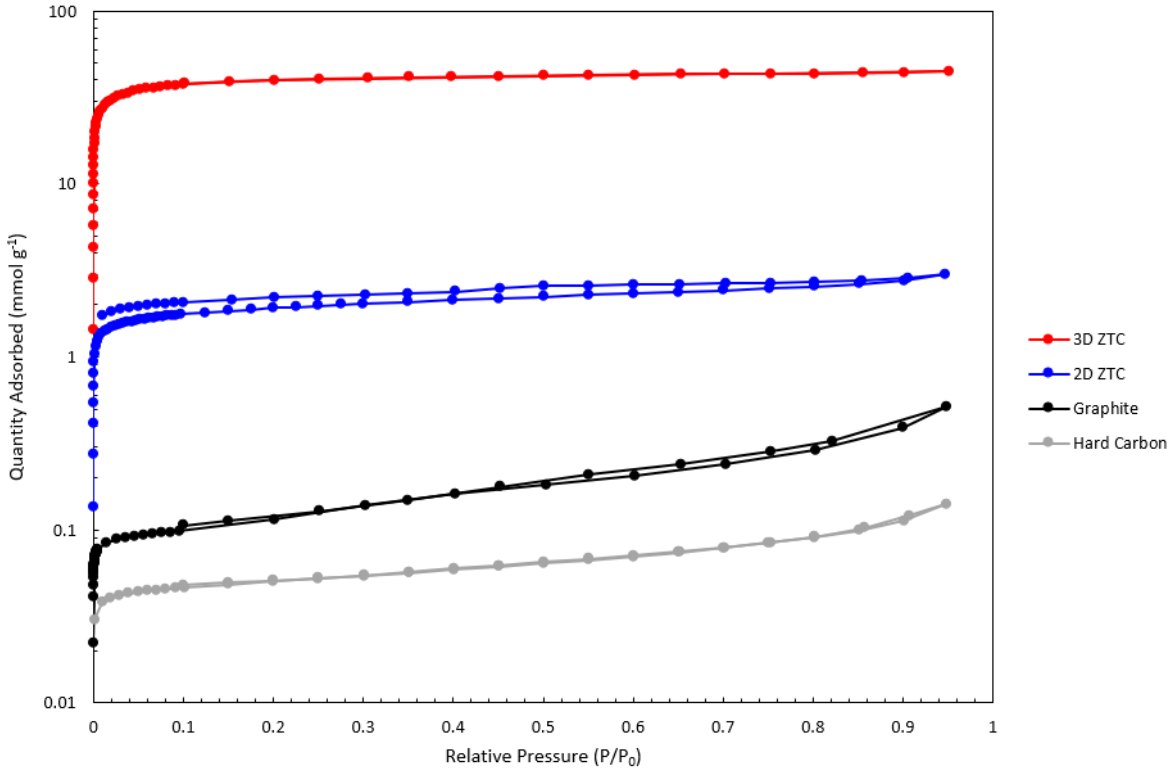

Figure S2. Equilibrium adsorption/desorption isotherms of N2 on 2D and 3D ZTCs at ~77 K (the boiling point of N_2 in Bozeman, Montana is 75.9 K).

Table S2. Initial coulombic efficiencies (ICE) of ZTCs and standard materials.

	LIB (%)	**NIB (%)**	**KIB (%)**
3D ZTC	16	10	5
2D ZTC	23	15	10
Graphite	72	-	46
Hard Carbon	-	57	-

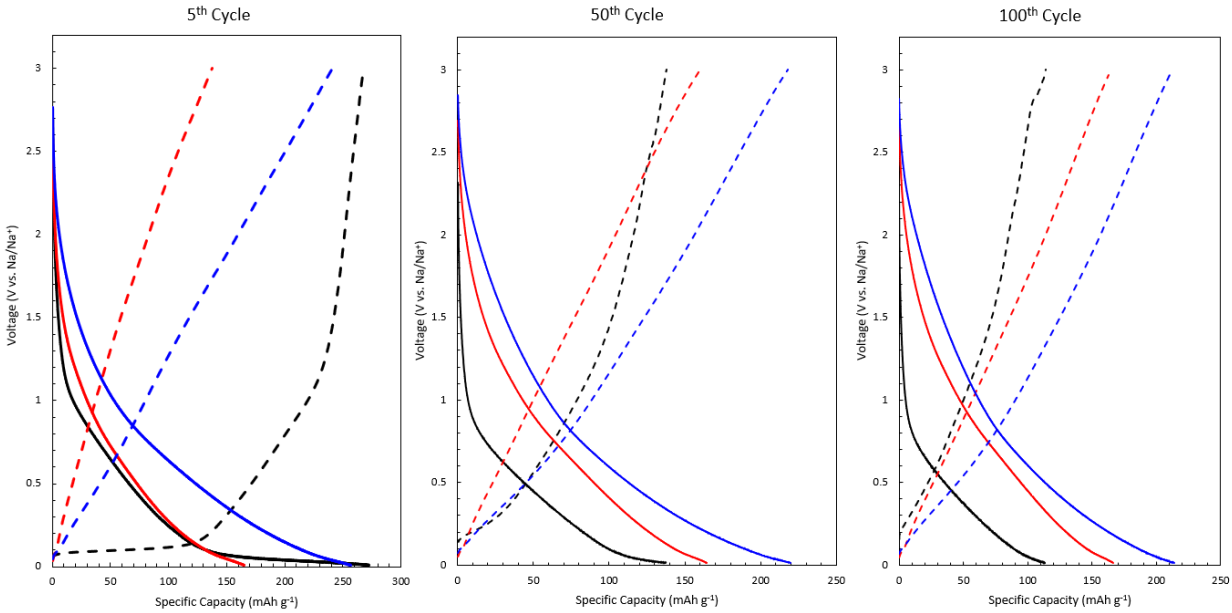

Figure S3. Voltage profiles of 2D ZTC, 3D ZTC, and Hard Carbon. Na^+ storage at the 5th, 50th, and 100th cycles. 100 mA g^{-1} from 0.01-3.0 V vs. Na/Na^+.

References

(1) Nishihara, H.; Kyotani, T. Zeolite-Templated Carbons - Three-Dimensional Microporous Graphene Frameworks. *Chem Commun (Camb)* **2018**, *54* (45), 5648-5673

(2) Lee, H.; Kim, K.; Kang, S. H.; Kwon, Y.; Kim, J. H.; Kwon, Y. K.; Ryoo, R.; Park, J. Y. Extremely High Electrical Conductance of Microporous 3d Graphene-Like Zeolite-Templated Carbon Framework. *Sci Rep* **2017**, *7* (1), 11460

(3) Itoi, H.; Nishihara, H.; Kogure, T.; Kyotani, T. Three-Dimensionally Arrayed and Mutually Connected 1.2-Nm Nanopores for High-Performance Electric Double Layer Capacitor. *J Am Chem Soc* **2011**, *133* (5), 1165-1167

(4) Curtis J. Meyers, S. D. S., Sejal C. Patel, Rita M. Sneeringer, Carol A. Bessel, Norman R. Dollahon, Randolph A. Leising, and Esther S. Takeuchi. Templated Synthesis of Carbon Materials from Zeolites (Y, Beta, and Zsm-5) and a Montmorillonite Clay (K10): Physical and Electrochemical Characterization. *Journal of Physical Chemistry B* **2001**, *105*, 2143-2152

(5) Stadie, N. P.; Wang, S.; Kravchyk, K. V.; Kovalenko, M. V. Zeolite-Templated Carbon as an Ordered Microporous Electrode for Aluminum Batteries. *ACS Nano* **2017**, *11* (2), 1911-1919

(6) Dubey, R. J.; Colijn, T.; Aebli, M.; Hanson, E. E.; Widmer, R.; Kravchyk, K. V.; Kovalenko, M. V.; Stadie, N. P. Zeolite-Templated Carbon as a Stable, High Power Magnesium-Ion Cathode Material. *ACS Appl Mater Interfaces* **2019**, *11* (43), 39902-39909

(7) Dubey, R. J.; Nussli, J.; Piveteau, L.; Kravchyk, K. V.; Rossell, M. D.; Campanini, M.; Erni, R.; Kovalenko, M. V.; Stadie, N. P. Zeolite-Templated Carbon as the Cathode for a High Energy Density Dual-Ion Battery. *ACS Appl Mater Interfaces* **2019**, *11* (19), 17686-17696

(8) McGlamery, D.; McDaniel, C.; Xu, W.; Stadie, N. P. Hydrogen-Type Binding Sites in Carbonaceous Electrodes for Rapid Lithium Insertion. *ACS Appl Mater Interfaces* **2023**, *15* (33), 39211-39217

(9) Ch. Baerlocher, L. B. M., D.H. Olson. *Atlas of Zeolite Frameworks*; Elsevier, 2007.

(10) Takashi Kyotani, T. N., Sanjuro Inoue, and Akira Tomita. Formation of New Type of Porous Carbon by Carbonization in Zeolite Nanochannels. *Chemistry of Materials* **1997**, *9* (2)

(11) Douglas L. Dorset, G. J. K., Karl G. Strohmaier, Maria J. Diaz-Cabanas, Fernando Rey, and Avelino Coma. P-Derived Organic Cations as Structure-Directing Agents: Synthesis of a High-Silica Zeolite (Itq-27) with a Two-Dimensional 12-Ring Channel System. *Journal of the American Chemical Society* **2006**, *128* (27), 8702-8987

(12) Chaehoon Kim, D.-Y. K., Yongjin Lee, Jihoon Choi, Hae Sung Cho, Minkee Choi. Bottom-up Synthesis of Two-Dimensional Carbon with Vertically Aligned Ordered Micropores for Ultrafast Nanofiltration. *Science Advances* **2023**

(13) Conway, B. E. Transition from "Supercapacitor" to "Battery" Behavior in Electrochemical Energy Storage. *Journey of The Electrochemical Society* **1991**, *138* (6)

(14) Khanin Nueangnoraj, H. N., Takafumi Ishii, Norihisa Yamamoto, Hiroyuki Itoi, Raul Berenguer, Ramiro Ruiz-Rosas, Diego Cazorla-Amoros, Emilia Morallon, Masashi Ito, Takashi Kyotani. Pseudocapacitance of Zeolite-Templated Carbon in Organic Electrolytes. *Energy Storage Materials* **2015**, *1*, 35-41

(15) Hirotomo Nishihara, Q.-H. Y., Peng-Xiang Hou, Masashi Unno, Seigo Yamauchi, Riichiro Saito, Juan I. Paredes, Amelia Martinez-Alonso, Juan M.D. Tascon, Yohei Sato, Masami Terauchi, Takashi Kyotani. A Possible Buckybowl-Like Structure of Zeolite Templated Carbon. *Carbon* **2009**, *47*, 1220-1230

(16) Gogotsi, Y.; Penner, R. M. Energy Storage in Nanomaterials - Capacitive, Pseudocapacitive, or Battery-Like? *ACS Nano* **2018**, *12* (3), 2081-2083

(17) Fleischmann, S.; Zhang, Y.; Wang, X.; Cummings, P. T.; Wu, J.; Simon, P.; Gogotsi, Y.; Presser, V.; Augustyn, V. Continuous Transition from Double-Layer to Faradaic Charge Storage in Confined Electrolytes. *Nature Energy* **2022**, *7* (3), 222-228

(18) Zhixin Ma, T. K., Akira Tomita. Synthesis Methods for Preparing Microporous Carbons with a Structural Regularity of Zeolite Y. *Carbon* **2002**, *40* (13), 2367-2374

(19) Koichi Matsuoka, Y. Y., Toshiaki Yamazaki, Norihiko Setoyama, Akira Tomita, Takashi Kyotani. Extremely High Microporosity and Sharp Pore Size Distribution of a Large Surface Area Carbon Prepared in the Nanochannels of Zeolite Y. *Carbon* **2005**, *43* (4)

(20) Welty, C.; Taylor, E. E.; Posey, S.; Vailati, P.; Kravchyk, K. V.; Kovalenko, M. V.; Stadie, N. P. Methodological Studies of the Mechanism of Anion Insertion in Nanometer-Sized Carbon Micropores. *ChemSusChem* **2023**, *16* (4), e202201847

(21) Sun, L.; Park, S. S.; Sheberla, D.; Dinca, M. Measuring and Reporting Electrical Conductivity in Metal-Organic Frameworks: Cd(2)(Ttftb) as a Case Study. *J Am Chem Soc* **2016**, *138* (44), 14772-14782

(22) Xu, W.; Welty, C.; Peterson, M. R.; Read, J. A.; Stadie, N. P. Exploring the Limits of the Rapid-Charging Performance of Graphite as the Anode in Lithium-Ion Batteries. *Journal of The Electrochemical Society* **2022**, *169* (1)

(23) Moriwake, H.; Kuwabara, A.; Fisher, C. A. J.; Ikuhara, Y. Why Is Sodium-Intercalated Graphite Unstable? *RSC Advances* **2017**, *7* (58), 36550-36554

(24) Hirotomo Nishihara, H. F., Hiroyuki Itoi, Keita Nomura, Hideki Tanaka, Minoru T. Miyahara, Patrick A. Bonnaud, Ryuji Miura, Ai Suzuki, Naoto Miyamoto, Nozomu Hatakeyama, Akira Miyamoto, Kazutaka Ikeda, Toshiya Otomo, Takashi Kyotani. Graphene-Based Ordered Framework with a Diverse Range of Carbon Polygons Formed in Zeolite Nanochannels. *Carbon* **2018**, *129*, 854-862

(25) Taylor, E. E.; Garman, K.; Stadie, N. P. Atomistic Structures of Zeolite-Templated Carbon. *Chemistry of Materials* **2020**, *32* (7), 2742-2752

(26) Nishihara, H.; Kyotani, T. Templated Nanocarbons for Energy Storage. *Adv Mater* **2012**, *24* (33), 4473-4498

(27) Tan, S.; Jean, J.; Pralong, V.; Moldovan, S.; Guo, H.; Mintova, S. Effect of Particle Size on the Sodium Ions Utilization Efficiency of Zeolite-Templated Carbon as the Anode in a Sodium Ion Battery. *Crystal Growth & Design* **2023**, *23* (6), 4065-4073

(28) Bacon, G. E. The Interlayer Spacing of Graphite. *Acta Cryst.* **1951**, *4*, 558

(29) Ong, M. T.; Verners, O.; Draeger, E. W.; van Duin, A. C.; Lordi, V.; Pask, J. E. Lithium Ion Solvation and Diffusion in Bulk Organic Electrolytes from First-Principles and Classical Reactive Molecular Dynamics. *J Phys Chem B* **2015**, *119* (4), 1535-1545

(30) Pham, T. A.; Kweon, K. E.; Samanta, A.; Lordi, V.; Pask, J. E. Solvation and Dynamics of Sodium and Potassium in Ethylene Carbonate from Ab Initio Molecular Dynamics Simulations. *The Journal of Physical Chemistry C* **2017**, *121* (40), 21913-21920

(31) Chen, D.; Zhang, W.; Luo, K.; Song, Y.; Zhong, Y.; Liu, Y.; Wang, G.; Zhong, B.; Wu, Z.; Guo, X. Hard Carbon for Sodium Storage: Mechanism and Optimization Strategies toward Commercialization. *Energy & Environmental Science* **2021**, *14* (4), 2244-2262

CHAPTER SIX

CONCLUSION

Summary of Results

The motivation of this research is twofold: to gain insight into the electrical and ionic pathways that lead to charge storage in porous frameworks and to inform materials for next generation electrodes. Electrochemical energy storage systems designed from channeled, layered, and three-dimensionally porous structures can enhance energy density, charging kinetics, and cycle life. Extrinsic benefits are also affected such as low emissions in materials production, avoidance of toxic transition metals, and green recycling. The transfer of chemical energy to electrical energy requires two distinct mechanisms to happen simultaneously, the diffusion of electrons through a solid framework and the diffusion of ions through a liquid. The convergence of these two mechanisms concludes in a certain degree of charge transfer that is dependent on the chemical nature of the solid and the liquid. A combination of electrochemical and materials characterization were used to clarify the character and relationship of these mechanisms. This work has two specific focuses, to understand the electrochemical properties of ZTCs with respect to both anion and cation storage, and to elucidate the conductivity mechanisms in yttrium-based MOFs. In the first study we explored the properties of various anions and how they interact with the pores of ZTC. In the last two studies we compared a layered structure with its cubic analog to understand how ionic and electronic behavior depends on dimensionality. To study the ionic behavior, 2D and 3D ZTCs were fabricated into cathodes and electrochemically tested with 3 different cations (Li^+, Na^+, and K^+). To study the electrical

conductivity, 2D and 3D lanthanide-based MOFs were synthesized and characterized experimentally and computationally.

This dissertation addresses the three objectives outlined in chapter one, each of which has progressed the fundamental understanding of electrochemical mechanisms.

Objective 1

With a methodological approach, we have thoroughly characterized the variables relevant to anion storage in ZTC. Historically, the focus of DIB chemistry has been on the anode and very little attention has been given to the cathode other than employing activated carbon. Through the exploration of 21 unique electrolyte combinations and various voltage windows, current rates, and electrolyte concentrations we have provided a fundamental template to guide future research. We elucidated trends between electrolyte properties and electrochemical protocols. This study showed that the electrochemical signature depended more on the composition of the anion and solvent than the size and shape. Anions with tightly bound fluorine groups such as BF_4^- boasted a highly localized electron cloud. These anions benefitted more from a high dielectric constant solvent such as PC that reduced ion pairing with Li^+ and enhanced diffusion. $TFSI^-$ dissociates more readily from its counterion and therefore does not require a polar solvent, it showed better rate capability in a low viscosity solvent such as DMC. In binary solvents (EC/DMC) where viscosity and polarity are balanced by each solvent, we could make more definitive conclusions about anion properties. In agreeance with intuition, as the diffusivity of the anion increased, the capacity increased, and this was more pronounced at high current rates. There are a plethora of correlations and conclusions that can be made from the data we collected on anion storage in ZTC in this study.

Objective 2

Through the novel synthesis of two structurally unique but compositionally different MOFs we have demonstrated the dependence of electrical conductivity on dimensionality. It is well known that "through-space" and "through-bond" conductivity pathways are affected by the electron density of the metal center. How the topology of identical metal-organic moieties effects conductivity pathways is less known. We presented two MOFs based on the lanthanide class of metals, yttrium. The valence electrons of yttrium lie in shielded 4*f* orbitals which allow the metal to crystallize in both hexagonal and cubic structures by tuning the temperature and equivalence. The conductivity pathways of both MOFs are categorized as "through-space" but arose from different mechanisms. The hexagonal layer YHOTP MOF transferred electrons via π- π stacking of the triphenylene linker. This was made possible by the Y atom pulling the layers close enough for the π orbitals to overlap and partake in band-like charge transfer. The cubic Y_6HOTP_2 MOF posessed large band gaps due to the distance between the linkers in the secondary building unit. The surprisingly high conductivity arose from a high charge carrier concentration on the linkers that were in a highly reduced state due to an air-free synthesis. The difference in linker geometries greatly effected the charge transport mechanisms which were confirmed by experimental conductivity measurements.

Objective 3

With extensive electrochemical characterization in different electrolytes (Li^+, Na^+, K^+) we were able to reveal trends between ion size and charge storage mechanisms in two different ZTC topologies. Materials that can accommodate larger ions than Li^+ and do so at high current rates are sought after for next generation energy storage. Both 2D and 3D ZTC are able to diffuse

cations rapidly into their pores during charging and surpass the capabilities of commercial hard carbon at modest current densities. The variation in cation size in this study elucidated the charge storage mechanisms of each material. As the ion increased in size from Li^+ to Na^+ to K^+ the layered 2D ZTC outperformed the cubic 3D ZTC up to higher and higher current rates. 2D ZTC benefitted from more faradaic charge transfer in between its graphitic layers whereas 3D ZTC simply lost active surface area with the larger ions. Larger ions desolvated faster which influenced the rate capability of the layered structures. The cubic structure experienced very little desolvation due to its large pores and therefore was hindered by the bulky solvation structures of Na^+ and K^+. Both ZTC materials showed pseudocapacitive behavior with deformed box-like CVs and sloped GCD profiles which suggests that oxygen functional groups played an important role on their rate capability.

Future Work

There are countless questions to be answered regarding the interaction of molecules at the surface of porous frameworks and this work inspired many more. The ordered pores of ZTC provide a model material that can be used to understand how the solvation shells of ions interact with charge transfer.

Cointercalating solvent molecules with the active cation will benefit rate capability but hinder energy density, finding a system that balances these two factors is interesting. Loss of capacitance is observed in carbon pores that are smaller than the Debye length of the electrolyte.[1] Graphite intercalates Li^+ ions at low potentials because the ions are forced to desolvate in order to fit in between the narrow graphene layers.[2] If an ion can remain solvated into the pores of a material but still induce a faradaic charge transfer then the energy density can be retained and the

rate capability will not suffer from the desolvation step. 2D ZTC provided an interested material for this purpose, its layers were 0.25 Å larger than graphite which allowed Li^+ ions to enter solvated, but the average voltage was still too high to compete with the energy density of graphite. Na^+ showed a lower average voltage due to a more faradaic charge transfer which was caused by a higher degree of confinement. The rate capability of this system suggested that some desolvation was required and if there was a way for solvent molecules to deform they could fit into the layers with the Na^+ ion. Recent studies have shown that ether, ester, and diglyme based solvents can perform this exact mechanism.[3, 4] However, the absolute capacities of these systems are low because of the low inra-porous surface areas of the materials. The wide interlayer spacing and 12 Å inter-sheet pores of 2D ZTC would make it an ideal candidate for this system.

Another way to test this hypothesis would be the use of ionic liquids which require no solvent for diffusion. If the ion size matches the pore size of the host framework, enhanced charge transfer can occur. Typically, multiple ions fit into a pore and electrical double layer capacitance occurs because of the resistance of like charges which scales with surface area. But if there is only one charge interacting with the pore then the ion can interact more intimately with the surface, inducing intense orbital overlap.[5] This hypothesis has never been tested on a high surface area, ordered, microporous carbon framework such as ZTC and likely produce interesting results.

References

1) Biesheuvel, P. M.; Porada, S.; Levi, M.; Bazant, M. Z. Attractive Forces in Microporous Carbon Electrodes for Capacitive Deionization. Journal of Solid State Electrochemistry 2014, 18 (5), 1365-1376.

(2) Pham, T. A.; Kweon, K. E.; Samanta, A.; Ong, M. T.; Lordi, V.; Pask, J. E. Intercalation of Lithium into Graphite: Insights from First-Principles Simulations. The Journal of Physical Chemistry C 2020, 124 (40), 21985-21992.

(3) Han, P.; Han, X.; Yao, J.; Zhang, L.; Cao, X.; Huang, C.; Cui, G. High Energy Density Sodium-Ion Capacitors through Co-Intercalation Mechanism in Diglyme-Based Electrolyte System. Journal of Power Sources 2015, 297, 457-463.

(4) Jache, B.; Adelhelm, P. Use of Graphite as a Highly Reversible Electrode with Superior Cycle Life for Sodium-Ion Batteries by Making Use of Co-Intercalation Phenomena. Angew Chem Int Ed Engl 2014, 53 (38), 10169-10173.

(5) Kondrat, S.; Georgi, N.; Fedorov, M. V.; Kornyshev, A. A. A Superionic State in Nano-Porous Double-Layer Capacitors: Insights from Monte Carlo Simulations. Phys Chem Chem Phys 2011, 13 (23), 11359-11366.

CUMULATIVE REFERENCES

Ahmad, T.; Zhang, D. A Critical Review of Comparative Global Historical Energy Consumption and Future Demand: The Story Told So Far. Energy Reports 2020, 6, 1973-1991.

An, S. J.; Li, J.; Daniel, C.; Mohanty, D.; Nagpure, S.; Wood, D. L. The State of Understanding of the Lithium-Ion-Battery Graphite Solid Electrolyte Interphase (Sei) and Its Relationship to Formation Cycling. Carbon 2016, 105, 52-76.

Apostol, P.; Gali, S. M.; Su, A.; Tie, D.; Zhang, Y.; Pal, S.; Lin, X.; Bakuru, V. R.; Rambabu, D.; Beljonne, D.; Dincă, M.; Vlad, A. Controlling Charge Transport in 2D Conductive MOFs─The Role of Nitrogen-Rich Ligands and Chemical Functionality. J. Am. Chem. Soc. 2023 145 (45), 24669-24677

Asenbauer, J.; Eisenmann, T.; Kuenzel, M.; Kazzazi, A.; Chen, Z.; Bresser, D. The Success Story of Graphite as a Lithium-Ion Anode Material – Fundamentals, Remaining Challenges, and Recent Developments Including Silicon (Oxide) Composites. Sustainable Energy & Fuels 2020, 4 (11), 5387-5416.

Bacon, G. E. The Interlayer Spacing of Graphite. Acta Cryst. 1951, 4, 558

Ballantyne, A. D.; Hallett, J. P.; Riley, D. J.; Shah, N.; Payne, D. J. Lead Acid Battery Recycling for the Twenty-First Century. R Soc Open Sci 2018, 5 (5), 171368.

Banda, H.; Dou, J. H.; Chen, T.; Libretto, N. J.; Chaudhary, M.; Bernard, G. M.; Miller, J. T.; Michaelis, V. K.; Dinca, M. High-Capacitance Pseudocapacitors from Li(+) Ion Intercalation in Nonporous, Electrically Conductive 2d Coordination Polymers. J Am Chem Soc 2021, 143 (5), 2285-2292.

Biesheuvel, P. M.; Porada, S.; Levi, M.; Bazant, M. Z. Attractive Forces in Microporous Carbon Electrodes for Capacitive Deionization. Journal of Solid State Electrochemistry 2014, 18 (5), 1365-1376.

Borodin, O.; Behl, W.; Jow, T. R. Oxidative Stability and Initial Decomposition Reactions of Carbonate, Sulfone, and Alkyl Phosphate-Based Electrolytes. The Journal of Physical Chemistry C 2013, 117 (17), 8661-8682.

Boyden, A.; Soo, V. K.; Doolan, M. The Environmental Impacts of Recycling Portable Lithium-Ion Batteries. Procedia CIRP 2016, 48, 188-193.

Bruce Dunn, H. K., Jean-Marie Tarascon. Electrical Energy Storage for the Grid: A Battery of Choices. Science 2011, 334 (6058), 928-935.

Carl-Friedrich Schön, S. v. B., Christian Mattes, Aakash Yadav, Martin Grohe, Leif Kobbelt, Matthias Wuttig. Classification of Properties and Their Relation to Chemical Bonding: Essential Steps toward the Inverse Design of Functional Materials. Science Advances 2022, 8.

Ch. Baerlocher, L. B. M., D.H. Olson. Atlas of Zeolite Frameworks; Elsevier, 2007.

Chaehoon Kim, D.-Y. K., Yongjin Lee, Jihoon Choi, Hae Sung Cho, Minkee Choi. Bottom-up Synthesis of Two-Dimensional Carbon with Vertically Aligned Ordered Micropores for Ultrafast Nanofiltration. Science Advances 2023, 9.

Chen, D.; Zhang, W.; Luo, K.; Song, Y.; Zhong, Y.; Liu, Y.; Wang, G.; Zhong, B.; Wu, Z.; Guo, X. Hard Carbon for Sodium Storage: Mechanism and Optimization Strategies toward Commercialization. Energy & Environmental Science 2021, 14 (4), 2244-2262

Cheng, H.; Ma, Z.; Kumar, P.; Liang, H.; Cao, Z.; Xie, H.; Cavallo, L.; Kim, H.; Li, Q.; Sun, Y. K.; et al. High Voltage Electrolyte Design Mediated by Advanced Solvation Chemistry toward High Energy Density and Fast Charging Lithium-Ion Batteries. Advanced Energy Materials 2024, 14 (18).

Clough, A. J.; Skelton, J. M.; Downes, C. A.; de la Rosa, A. A.; Yoo, J. W.; Walsh, A.; Melot, B. C.; Marinescu, S. C. Metallic Conductivity in a Two-Dimensional Cobalt Dithiolene Metal-Organic Framework. J. Am. Chem. Soc. 2017, 139 (31), 10863-10867

Conway, B. E. Transition from "Supercapacitor" to "Battery" Behavior in Electrochemical Energy Storage. Journey of The Electrochemical Society 1991, 138 (6)

Curtis J. Meyers, S. D. S., Sejal C. Patel, Rita M. Sneeringer, Carol A. Bessel, Norman R. Dollahon, Randolph A. Leising, and Esther S. Takeuchi. Templated Synthesis of Carbon Materials from Zeolites (Y, Beta, and Zsm-5) and a Montmorillonite Clay (K10): Physical and Electrochemical Characterization. Journal of Physical Chemistry B 2001, 105, 2143-2152

Dahn, J. A. S. a. J. R. Electrochemical Intercalation of Pf6 into Graphite. Journal of the Electrochemical Society 2000, 147.

Davidsson Kurland, S. Energy Use for Gwh-Scale Lithium-Ion Battery Production. Environmental Research Communications 2019, 2 (1).

Day, R. W.; Bediako, D. K.; Rezaee, M.; Parent, L. R.; Skorupskii, G.; Arguilla, M. Q.; Hendon, C. H.; Stassen, I.; Gianneschi, N. C.; Kim, P.; et al. Single Crystals of Electrically Conductive Two-Dimensional Metal-Organic Frameworks: Structural and Electrical Transport Properties. ACS Cent. Sci. 2019, 5 (12), 1959-1964

Debela, T. T.; Yang, M. C.; Hendon, C. H. Ligand-Mediated Hydrogenic Defects in Two-Dimensional Electrically Conductive Metal-Organic Frameworks. J. Am. Chem. Soc. 2023, 145 (20), 11387-11391

Degen, F.; Winter, M.; Bendig, D.; Tübke, J. Energy Consumption of Current and Future Production of Lithium-Ion and Post Lithium-Ion Battery Cells. Nature Energy 2023, 8 (11), 1284-1295.

Demuth, M. C.; Hendon, C. H. Linker Aromaticity Reduces Band Dispersion in 2D Conductive Metal–Organic Frameworks. ACS Mater. Lett. 2023, 5 (5), 1476-1480

Deng, J.; Luo, W. B.; Chou, S. L.; Liu, H. K.; Dou, S. X. Sodium-Ion Batteries: From Academic Research to Practical Commercialization. Advanced Energy Materials 2017, 8 (4).

Diamond, B. G.; Payne, L. I.; Hendon, C. H. Ligand Field Tuning of D-Orbital Energies in Metal-Organic Framework Clusters. Commun. Chem. 2023, 6 (1), 67-73

Division, E. S. Cradle-to-Grave Lifecycle Analysis of U.S. Light-Duty Vehicle-Fuel Pathways: A Greenhouse Gas Emissions and Economic Assessment of Current (2020) and Future (2030-2035) Technologies; Argonne National Lab, 2020.

Domi, Y.; Usui, H.; Ando, A.; Nishikawa, K.; Sakaguchi, H. Analysis of the Li Distribution in Si-Based Negative Electrodes for Lithium-Ion Batteries by Soft X-Ray Emission Spectroscopy. ACS Applied Energy Materials 2020, 3 (9), 8619-8626.

Douglas L. Dorset, G. J. K., Karl G. Strohmaier, Maria J. Diaz-Cabanas, Fernando Rey, and Avelino Coma. P-Derived Organic Cations as Structure-Directing Agents: Synthesis of a High-Silica Zeolite (Itq-27) with a Two-Dimensional 12-Ring Channel System. Journal of the American Chemical Society 2006, 128 (27), 8702-8987

Dubey, R. J.; Colijn, T.; Aebli, M.; Hanson, E. E.; Widmer, R.; Kravchyk, K. V.; Kovalenko, M. V.; Stadie, N. P. Zeolite-Templated Carbon as a Stable, High Power Magnesium-Ion Cathode Material. ACS Appl Mater Interfaces 2019, 11 (43), 39902-39909.

Dubey, R. J.; Nussli, J.; Piveteau, L.; Kravchyk, K. V.; Rossell, M. D.; Campanini, M.; Erni, R.; Kovalenko, M. V.; Stadie, N. P. Zeolite-Templated Carbon as the Cathode for a High Energy Density Dual-Ion Battery. ACS Appl Mater Interfaces 2019, 11 (19), 17686-17696

Dunn, J. B.; Gaines, L.; Kelly, J. C.; James, C.; Gallagher, K. G. The Significance of Li-Ion Batteries in Electric Vehicle Life-Cycle Energy and Emissions and Recycling's Role in Its Reduction. Energy & Environmental Science 2015, 8 (1), 158-168.

Electrochemical Energy Storage Electrochemical Science and Technology 1991, 138.
Erik Emilsson, L. D. Lithium Ion Vehicle Production; Swedish Environmental Research Institute, 2019.

Fan, W.; Zhang, H.; Wang, H.; Zhao, X.; Sun, S.; Shi, J.; Huang, M.; Liu, W.; Zheng, Y.; Li, P. Dual-Doped Hierarchical Porous Carbon Derived from Biomass for Advanced Supercapacitors and Lithium Ion Batteries. RSC Adv 2019, 9 (56), 32382-32394.

Fleischmann, S.; Mitchell, J. B.; Wang, R.; Zhan, C.; Jiang, D. E.; Presser, V.; Augustyn, V. Pseudocapacitance: From Fundamental Understanding to High Power Energy Storage Materials. Chem Rev 2020, 120 (14), 6738-6782.

Fleischmann, S.; Zhang, Y.; Wang, X.; Cummings, P. T.; Wu, J.; Simon, P.; Gogotsi, Y.; Presser, V.; Augustyn, V. Continuous Transition from Double-Layer to Faradaic Charge Storage in Confined Electrolytes. Nature Energy 2022, 7 (3), 222-228.

Frances P. McCullough, C. A. L., Roy V. Snelgrove. Secondary Battery. 1989.

G. Kresse, J. F. Efficiency of Ab-Initio Total Energy Calculations for Metals and Semiconductors Using a Plane-Wave Basis Set. Comput. Mater. Sci. 1996, 6 (1), 15-50

Ganguli, K. S. K. a. N. Large Anisotropy of the Electrical Conductivity of Graphite. Nature Energy 1939, 144.

Gaussian 09, Revision A.02; 2016.

Gogotsi, P. S. a. Y. Materials for Electrochemical Capacitors. Nature Materials 2008.

Gogotsi, Y.; Penner, R. M. Energy Storage in Nanomaterials - Capacitive, Pseudocapacitive, or Battery-Like? ACS Nano 2018, 12 (3), 2081-2083

Goodenough, J. B.; Park, K. S. The Li-Ion Rechargeable Battery: A Perspective. J Am Chem Soc 2013, 135 (4), 1167-1176.

Gregg, S. J.; Sing, K. S. W. A. Adsorption, Surface Area and Porosity; Academic Press, 1982.

Han, P.; Han, X.; Yao, J.; Zhang, L.; Cao, X.; Huang, C.; Cui, G. High Energy Density Sodium-Ion Capacitors through Co-Intercalation Mechanism in Diglyme-Based Electrolyte System. Journal of Power Sources 2015, 297, 457-463.

Han, S. Structure and Dynamics in the Lithium Solvation Shell of Nonaqueous Electrolytes. Sci Rep 2019, 9 (1), 5555.

Haskins, J. B.; Bennett, W. R.; Wu, J. J.; Hernandez, D. M.; Borodin, O.; Monk, J. D.; Bauschlicher, C. W., Jr.; Lawson, J. W. Computational and Experimental Investigation of Li-Doped Ionic Liquid Electrolytes: [Pyr14][Tfsi], [Pyr13][Fsi], and [Emim][Bf4]. J Phys Chem B 2014, 118 (38), 11295-11309.

Hendon, C. H.; Rieth, A. J.; Korzynski, M. D.; Dincă, M. Grand Challenges and Future Opportunities for Metal-Organic Frameworks. ACS Cent. Sci. 2017, 3 (6), 554-563

Hirotomo Nishihara, H. F., Hiroyuki Itoi, Keita Nomura, Hideki Tanaka, Minoru T. Miyahara, Patrick A. Bonnaud, Ryuji Miura, Ai Suzuki, Naoto Miyamoto, Nozomu Hatakeyama, Akira Miyamoto, Kazutaka Ikeda, Toshiya Otomo, Takashi Kyotani. Graphene-Based Ordered Framework with a Diverse Range of Carbon Polygons Formed in Zeolite Nanochannels. Carbon 2018, 129, 854-862

Hirotomo Nishihara, Q.-H. Y., Peng-Xiang Hou, Masashi Unno, Seigo Yamauchi, Riichiro Saito, Juan I. Paredes, Amelia Martinez-Alonso, Juan M.D. Tascon, Yohei Sato, Masami Terauchi, Takashi Kyotani. A Possible Buckybowl-Like Structure of Zeolite Templated Carbon. Carbon 2009, 47, 1220-1230

Hmadeh, M.; Lu, Z.; Liu, Z.; Gándara, F.; Furukawa, H.; Wan, S.; Augustyn, V.; Chang, R.; Liao, L.; Zhou, F.; et al. New Porous Crystals of Extended Metal-Catecholates. Chem. Mater. 2012, 24 (18), 3511-3513

Hsu, C.-P. The Electronic Couplings in Electron Transferand Excitation Energy Transfer. Acc. Chem. Res. 2009, 489-573

Hu, Z.; Liu, Q.; Zhang, K.; Zhou, L.; Li, L.; Chen, M.; Tao, Z.; Kang, Y. M.; Mai, L.; Chou, S. L.; et al. All Carbon Dual Ion Batteries. ACS Appl Mater Interfaces 2018, 10 (42), 35978-35983.

Hua, C.; Doheny, P. W.; Ding, B.; Chan, B.; Yu, M.; Kepert, C. J.; D'Alessandro, D. M. Through-Space Intervalence Charge Transfer as a Mechanism for Charge Delocalization in Metal-Organic Frameworks. J. Am. Chem. Soc. 2018, 140 (21), 6622-6630

IRENA. World Energy Transitions Outlook 2023; International Renewable Energy Agency, 2023.

Ishihara, T.; Koga, M.; Matsumoto, H.; Yoshio, M. Electrochemical Intercalation of Hexafluorophosphate Anion into Various Carbons for Cathode of Dual-Carbon Rechargeable Battery. Electrochemical and Solid-State Letters 2007, 10 (3).

Itoi, H.; Nishihara, H.; Kogure, T.; Kyotani, T. Three-Dimensionally Arrayed and Mutually Connected 1.2-Nm Nanopores for High-Performance Electric Double Layer Capacitor. J Am Chem Soc 2011, 133 (5), 1165-1167

J.-L. Bredas, D. Beljonne, V. Coropceanu, J. Cornil. Charge-Transfer and Energy-Transfer Processes in π-Conjugated Oligomersand Polymers: A Molecular Picture. Chem. Rev. 2004, 104 (11), 4887-5782

J.R. Dahn, J. A. S. Energy and Capacity Projections for Practical Dual-Graphite Cells. Journal of the Electrochemical Society 2000, 147.

Jache, B.; Adelhelm, P. Use of Graphite as a Highly Reversible Electrode with Superior Cycle Life for Sodium-Ion Batteries by Making Use of Co-Intercalation Phenomena. Angew Chem Int Ed Engl 2014, 53 (38), 10169-10173.

Jin, S. How to Effectively Utilize MOFs for Electrocatalysis. ACS Energy Lett. 2019, 4 (6), 1443-1445

Jonsson, E.; Johansson, P. Electrochemical Oxidation Stability of Anions for Modern Battery Electrolytes: A Cbs and Dft Study. Phys Chem Chem Phys 2015, 17 (5), 3697-3703.

Joyce McLaren, J. M.; Eric O'Shaughnessy, E. W., and Evan Shapiro. Emissions Associated with Electric Vehicle Charging: Impact of Electricity Generation Mix, Charging Infrastructure Availability, and Vehicle Type; National Renewable Energy Laboratory, 2016.

K. Mizushima, P. C. J., P. J. Wiseman and J. B. Goodenough. Lixcoo2 (0<X~L): A New Cathode Material for Materials of High Energy Density. Materials Research Bulletin 1980.

Khanin Nueangnoraj, H. N., Takafumi Ishii, Norihisa Yamamoto, Hiroyuki Itoi, Raul Berenguer, Ramiro Ruiz-Rosas, Diego Cazorla-Amoros, Emilia Morallon, Masashi Ito, Takashi Kyotani. Pseudocapacitance of Zeolite-Templated Carbon in Organic Electrolytes. Energy Storage Materials 2015, 1, 35-41

Kirkpatrick, J. An Approximate Method for Calculating Transfer Integrals Based on the Zindo Hamiltonian. Int. J. Quantum Chem. 2007, 108 (1), 51-56

Koichi Matsuoka, Y. Y., Toshiaki Yamazaki, Norihiko Setoyama, Akira Tomita, Takashi Kyotani. Extremely High Microporosity and Sharp Pore Size Distribution of a Large Surface Area Carbon Prepared in the Nanochannels of Zeolite Y. Carbon 2005, 43 (4),

Kondrat, S.; Georgi, N.; Fedorov, M. V.; Kornyshev, A. A. A Superionic State in Nano-Porous Double-Layer Capacitors: Insights from Monte Carlo Simulations. Phys Chem Chem Phys 2011, 13 (23), 11359-11366.

Layton, B. E. A Comparison of Energy Densities of Prevalent Energy Sources in Units of Joules Per Cubic Meter. International Journal of Green Energy 2008, 5 (6), 438-455.

Lee, H.; Kim, K.; Kang, S. H.; Kwon, Y.; Kim, J. H.; Kwon, Y. K.; Ryoo, R.; Park, J. Y. Extremely High Electrical Conductance of Microporous 3d Graphene-Like Zeolite-Templated Carbon Framework. Sci Rep 2017, 7 (1), 11460.

Li, C.; Zhang, L.; Chen, J.; Li, X.; Sun, J.; Zhu, J.; Wang, X.; Fu, Y. Recent Development and Applications of Electrical Conductive MOFs. Nanoscale 2021, 13 (2), 485-509

Li, J.; Kumar, A.; Ott, S. Diffusional Electron Transport Coupled to Thermodynamically Driven Electron Transfers in Redox-Conductive Multivariate Metal-Organic Frameworks. J Am Chem Soc 2024, 146 (17), 12000-12010.

Li, W. H.; Wu, X. L. Advanced Cathode Materials in Dual-Ion Batteries: Progress and Prospect. Electrochemical Science Advances 2021.

Liang, Y.; Dong, H.; Aurbach, D.; Yao, Y. Current Status and Future Directions of Multivalent Metal-Ion Batteries. Nature Energy 2020, 5 (9), 646-656.

Liu, J.; Zhu, D.; Guo, C.; Vasileff, A.; Qiao, S. Z. Design Strategies toward Advanced MOF-Derived Electrocatalysts for Energy-Conversion Reactions. Adv. Energy Mater. 2017, 7 (23), 1-26

Liu, M.; Wang, Y.; Wu, F.; Bai, Y.; Li, Y.; Gong, Y.; Feng, X.; Li, Y.; Wang, X.; Wu, C. Advances in Carbon Materials for Sodium and Potassium Storage. Advanced Functional Materials 2022, 32 (31).

Liu, Q.; Li, S.; Wang, S.; Zhang, X.; Zhou, S.; Bai, Y.; Zheng, J.; Lu, X. Kinetically Determined Phase Transition from Stage Ii (Lic(12)) to Stage I (Lic(6)) in a Graphite Anode for Li-Ion Batteries. J Phys Chem Lett 2018, 9 (18), 5567-5573.

Lu, Y.; Zhang, Y.; Yang, C. Y.; Revuelta, S.; Qi, H.; Huang, C.; Jin, W.; Li, Z.; Vega-Mayoral, V.; Liu, Y.; Huang, X.; Pohl, D.; Položij, M.; Zhou, S.; Cánovas, E.; Heine, T.; Fabiano, S.; Feng, X.; Dong, R.; Precise tuning of interlayer electronic coupling in layered conductive metal-organic frameworks. Nat. Commun. 2022, 13, 7240

Ma, Z.; Kyotani, T.; Tomita, A. Synthesis Methods for Preparing Microporous Carbons with Astructural Regularity of Zeolite Y. Carbon 2002, 40.

Maiti, S., Pramanik, A., Dhawa, T., Sreemany, M., & Mahanty, S. Bi-Metal Organic Framework Derived Nickel Manganese Oxide Spinel for Lithium-Ion Battery Anode. Mater. Sci. & Eng. B. 2018, 229, 27–36

Manthiram, A. An Outlook on Lithium Ion Battery Technology. ACS Cent Sci 2017, 3 (10), 1063-1069.

Mardirossian, N.; Head-Gordon, M. How Accurate Are the Minnesota Density Functionals for Noncovalent Interactions, Isomerization Energies, Thermochemistry, and Barrier Heights Involving Molecules Composed of Main-Group Elements? J Chem Theory Comput 2016, 12 (9), 4303-4325.

Matsuoka, K.; Yamagishi, Y.; Yamazaki, T.; Setoyama, N.; Tomita, A.; Kyotani, T. Extremely High Microporosity and Sharp Pore Size Distribution of a Large Surface Area Carbon Prepared in the Nanochannels of Zeolite Y. Carbon 2005, 43 (4), 876-879.

May 2024 Monthly Energy Review; U.S. Emergy Information Administration, 2024.

McGlamery, D.; McDaniel, C.; Xu, W.; Stadie, N. P. Hydrogen-Type Binding Sites in Carbonaceous Electrodes for Rapid Lithium Insertion. ACS Appl Mater Interfaces 2023, 15 (33), 39211-39217

Mehek, R.; Iqbal, N.; Noor, T.; Amjad, M. Z. B.; Ali, G.; Vignarooban, K.; Khan, M. A. Metal-Organic Framework Based Electrode Materials for Lithium-Ion Batteries: A Review. RSC Adv 2021, 11 (47), 29247-29266.

Moriwake, H.; Kuwabara, A.; Fisher, C. A. J.; Ikuhara, Y. Why Is Sodium-Intercalated Graphite Unstable? RSC Advances 2017, 7 (58), 36550-36554.

Nam, K. W.; Park, S. S.; Dos Reis, R.; Dravid, V. P.; Kim, H.; Mirkin, C. A.; Stoddart, J. F. Conductive 2D Metal-Organic Framework for High-Performance Cathodes in Aqueous Rechargeable Zinc Batteries. Nat. Commun. 2019, 10 (1), 4948

Nasalevich, M. A.; van der Veen, M.; Kapteijn, F.; Gascon, J. Metal–Organic Frameworks as Heterogeneous Photocatalysts: Advantages and Challenges. CrystEngComm 2014, 16 (23), 4919-4926.

Nath, A.; Kumar, V.; Shukla, A.; Ghosh, H. N.; Mandal, S. Influence of Molecular Separation on through-Space Intervalence Transient Charge Transfer in Metal-Organic Frameworks with Cofacially Arranged Redox Pairs. Angew. Chem. Int. Ed. 2023, 62 (31), e202308034

Nishihara, H.; Fujimoto, H.; Itoi, H.; Nomura, K.; Tanaka, H.; Miyahara, M. T.; Bonnaud, P. A.; Miura, R.; Suzuki, A.; Miyamoto, N.; et al. Graphene-Based Ordered Framework with a Diverse Range of Carbon Polygons Formed in Zeolite Nanochannels. Carbon 2018, 129, 854-862.

Nishihara, H.; Kyotani, T. Templated Nanocarbons for Energy Storage. Adv Mater 2012, 24 (33), 4473-4498

Nishihara, H.; Kyotani, T. Zeolite-Templated Carbons - Three-Dimensional Microporous Graphene Frameworks. Chem Commun (Camb) 2018, 54 (45), 5648-5673

Ong, M. T.; Verners, O.; Draeger, E. W.; van Duin, A. C.; Lordi, V.; Pask, J. E. Lithium Ion Solvation and Diffusion in Bulk Organic Electrolytes from First-Principles and Classical Reactive Molecular Dynamics. J Phys Chem B 2015, 119 (4), 1535-1545

Panja, T.; Ajuria, J.; Diez, N.; Bhattacharjya, D.; Goikolea, E.; Carriazo, D. Fabrication of High-Performance Dual Carbon Li-Ion Hybrid Capacitor: Mass Balancing Approach to Improve the Energy-Power Density and Cycle Life. Sci Rep 2020, 10 (1), 10842.

Park, G.; Demuth, M. C.; Hendon, C. H.; Park S. S. Acid-Dependent Charge Transport in a Solution-Processed 2D Conductive Metal-Organic Framework. J. Am. Chem. Soc. 2024, 146 (16), 11493-11499

Park, J. G.; Aubrey, M. L.; Oktawiec, J.; Chakarawet, K.; Darago, L. E.; Grandjean, F.; Long, G. J.; Long, J. R. Charge Delocalization and Bulk Electronic Conductivity in the Mixed-Valence Metal-Organic Framework Fe(1,2,3-Triazolate)2(BF4)x. J. Am. Chem. Soc. 2018, 140 (27), 8526-8534

Per Soderlind, O. E., Borje Johansson, J. M. Wilist, A. M. Boring A Unified Picture of the Crystal Structures of Metals. Letters to Nature 1996, 374.

Pham, T. A.; Kweon, K. E.; Samanta, A.; Lordi, V.; Pask, J. E. Solvation and Dynamics of Sodium and Potassium in Ethylene Carbonate from Ab Initio Molecular Dynamics Simulations. The Journal of Physical Chemistry C 2017, 121 (40), 21913-21920.

Pham, T. A.; Kweon, K. E.; Samanta, A.; Ong, M. T.; Lordi, V.; Pask, J. E. Intercalation of Lithium into Graphite: Insights from First-Principles Simulations. The Journal of Physical Chemistry C 2020, 124 (40), 21985-21992.

Placke, T., Bieker, Peter, Lux, Simon Franz, Fromm, Olga, Meyer, Hinrich-Wilhelm, Passerini, Stefano and Winter, Martin. Dual-Ion Cells Based on Anion Intercalation into Graphite from Ionic Liquid-Based Electrolytes. Zeitschrift für Physikalische Chemie 2012, 226, 391-407.

Placke, T.; Fromm, O.; Lux, S. F.; Bieker, P.; Rothermel, S.; Meyer, H.-W.; Passerini, S.; Winter, M. Reversible Intercalation of Bis(Trifluoromethanesulfonyl)Imide Anions from an Ionic Liquid Electrolyte into Graphite for High Performance Dual-Ion Cells. Journal of The Electrochemical Society 2012, 159 (11), A1755-A1765.

Placke, T.; Kloepsch, R.; Dühnen, S.; Winter, M. Lithium Ion, Lithium Metal, and Alternative Rechargeable Battery Technologies: The Odyssey for High Energy Density. Journal of Solid State Electrochemistry 2017, 21 (7), 1939-1964.

Read, J. A. In-Situ Studies on the Electrochemical Intercalation of Hexafluorophosphate Anion in Graphite with Selective Cointercalation of Solvent. The Journal of Physical Chemistry C 2015, 119 (16), 8438-8446.

Read, J. A.; Cresce, A. V.; Ervin, M. H.; Xu, K. Dual-Graphite Chemistry Enabled by a High Voltage Electrolyte. Energy Environ. Sci. 2014, 7 (2), 617-620.

Rodríguez-Pérez, I. A.; Ji, X. Anion Hosting Cathodes in Dual-Ion Batteries. ACS Energy Letters 2017, 2 (8), 1762-1770.

Rosamaria Fong, U. v. S., and J. R. Dahn. Studies of Lithium Intercalation into Carbons Using Nonaqueous Electrochemical Cells. Journal of the Electrochical Society 1990.

Rowsey, R.; Taylor, E. E.; Irle, S.; Stadie, N. P.; Szilagyi, R. K. Methane Adsorption on Heteroatom-Modified Maquettes of Porous Carbon Surfaces. J Phys Chem A 2021, 125 (28), 6042-6058.

Saha, R.; Gupta, K.; Gomez Garcia, C. J. Strategies to Improve Electrical Conductivity in Metal-Organic Frameworks: A Comparative Study. Cryst Growth Des 2024, 24 (5), 2235-2265.

Schimka, L.; Harl, J.; Kresse, G. Improved Hybrid Functional for Solids: The HSEsol Functional. J. Chem. Phys. 2011, 134 (2), 024116

Seo, D. M.; Reininger, S.; Kutcher, M.; Redmond, K.; Euler, W. B.; Lucht, B. L. Role of Mixed Solvation and Ion Pairing in the Solution Structure of Lithium Ion Battery Electrolytes. The Journal of Physical Chemistry C 2015, 119 (25), 14038-14046.

Sergio Trasatti, a. G. B. Ruthenium Dioxide: A New Interesting Electrode Material.

Sheberla, D.; Bachman, J. C.; Elias, J. S.; Sun, C. J.; Shao-Horn, Y.; Dincă, M. Conductive MOF Electrodes for Stable Supercapacitors with High Areal Capacitance. Nat. Mater. 2017, 16 (2), 220-224

Sheberla, D.; Sun, L.; Blood-Forsythe, M. A.; Er, S.; Wade, C. R.; Brozek, C. K.; Aspuru-Guzik, A.; Dincă, M. High Electrical Conductivity in Ni3(2,3,6,7,10,11-Hexaiminotriphenylene)2, a Semiconducting Metal-Organic Graphene Analogue. J. Am. Chem. Soc 2014, 136 (25), 8859-8862

Skorupskii, G.; Dincă, M. Electrical Conductivity in a Porous, Cubic Rare-Earth Catecholate. J. Am. Chem. Soc. 2020, 142 (15), 6920-6924

Skorupskii, G.; Trump, B. A.; Kasel, T. W.; Brown, C. M.; Hendon, C. H.; Dinca, M. Efficient and Tunable One-Dimensional Charge Transport in Layered Lanthanide Metal-Organic Frameworks. Nat Chem 2020, 12 (2), 131-136.

Song, W.; Teng, X.; Liu, Y.; Wang, J.; Niu, Y.; He, X.; Zhang, C.; Chen, Z. Rational Construction of Self-Supported Triangle-Like MOF-Derived Hollow (Ni,Co)Se(2) Arrays for Electrocatalysis and Supercapacitors. Nanoscale 2019, 11 (13), 6401-6409.

Stadie, N. P.; Wang, S.; Kravchyk, K. V.; Kovalenko, M. V. Zeolite-Templated Carbon as an Ordered Microporous Electrode for Aluminum Batteries. ACS Nano 2017, 11 (2), 1911-1919.

Stallinga, P. Electronic Transport in Organic Materials: Comparison of Band Theory with Percolation/(Variable Range) Hopping Theory. Adv Mater 2011, 23 (30), 3356-3362.

Statistical Review of World Energy; 2023.

Sun, L.; Park, S. S.; Sheberla, D.; Dinca, M. Measuring and Reporting Electrical Conductivity in Metal-Organic Frameworks: Cd(2)(Ttftb) as a Case Study. J Am Chem Soc 2016, 138 (44), 14772-14782

Syzgantseva, M. A.; Stepanov, N. F.; Syzgantseva, O. A. Band Alignment as the Method for Modifying Electronic Structure of Metal-Organic Frameworks. ACS Appl. Mater. Inter. 2020, 12 (15), 17611-17619

Tahir, M. A., Arshad, N., & Akram, M. Recent Advances in Metal Organic Framework (MOF) as Electrode Material for Super Capacitor: A Mini Review. J. of Energy Storage 2022, 47, 103530

Takashi Kyotani, T. N., Sanjuro Inoue, and Akira Tomita. Formation of New Type of Porous Carbon by Carbonization in Zeolite Nanochannels. Chemistry of Materials 1997, 9 (2),

Tan, S.; Jean, J.; Pralong, V.; Moldovan, S.; Guo, H.; Mintova, S. Effect of Particle Size on the Sodium Ions Utilization Efficiency of Zeolite-Templated Carbon as the Anode in a Sodium Ion Battery. Crystal Growth & Design 2023, 23 (6), 4065-4073

Tan, S.; Yang, H.; Zhang, Z.; Xu, X.; Xu, Y.; Zhou, J.; Zhou, X.; Pan, Z.; Rao, X.; Gu, Y.; et al. The Progress of Hard Carbon as an Anode Material in Sodium-Ion Batteries. Molecules 2023, 28 (7).

Tao, L.; Xia, D.; Sittisomwong, P.; Zhang, H.; Lai, J.; Hwang, S.; Li, T.; Ma, B.; Hu, A.; Min, J.; et al. Solvent-Mediated, Reversible Ternary Graphite Intercalation Compounds for Extreme-Condition Li-Ion Batteries. J Am Chem Soc 2024.

Taylor, E. E.; Garman, K.; Stadie, N. P. Atomistic Structures of Zeolite-Templated Carbon. Chemistry of Materials 2020, 32 (7), 2742-2752.

Touzain, R. Y. a. P. A Reversible Graphite-Lithium Negative Electrode for Electrochemical Generators. Jounral of Power Sources 1982, 9, 365-371.

Ue, M.; Takeda, M.; Takehara, M.; Mori, S. Electrochemical Properties of Quaternary Ammonium Salts for Electrochemical Capacitors. Journal of the Electrochemical Society 1997, 133 (8), 2684-2688.

Wang, H. F.; Chen, L.; Pang, H.; Kaskel, S.; Xu, Q. MOF-Derived Electrocatalysts for Oxygen Reduction, Oxygen Evolution and Hydrogen Evolution Reactions. Chem. Soc. Rev. 2020, 49 (5), 1414-1448

Wang, M.; Tang, Y. A Review on the Features and Progress of Dual-Ion Batteries. Advanced Energy Materials 2018, 8 (19).

Wang, S.; Kravchyk, K. V.; Filippin, A. N.; Muller, U.; Tiwari, A. N.; Buecheler, S.; Bodnarchuk, M. I.; Kovalenko, M. V. Aluminum Chloride-Graphite Batteries with Flexible Current Collectors Prepared from Earth-Abundant Elements. Adv Sci (Weinh) 2018, 5 (4), 1700712.

Wang, S.; Kravchyk, K. V.; Filippin, A. N.; Widmer, R.; Tiwari, A. N.; Buecheler, S.; Bodnarchuk, M. I.; Kovalenko, M. V. Overcoming the High-Voltage Limitations of Li-Ion Batteries Using a Titanium Nitride Current Collector. ACS Applied Energy Materials 2019, 2 (2), 974-978.

Wang, Y.; Liu, Y.; Wang, H.; Liu, W.; Li, Y.; Zhang, J.; Hou, H.; Yang, J. Ultrathin Nico-Mof Nanosheets for High-Performance Supercapacitor Electrodes. ACS Applied Energy Materials 2019, 2 (3), 2063-2071.

Welty, C.; Taylor, E. E.; Posey, S.; Vailati, P.; Kravchyk, K. V.; Kovalenko, M. V.; Stadie, N. P. Methodological Studies of the Mechanism of Anion Insertion in Nanometer-Sized Carbon Micropores. ChemSusChem 2023, 16 (4), e202201847

Whittingham, M. S. Electrical Energy Storage and Intercalation Chemistry. Science 1976, 192 (4244), 1126-1127.

Winter, M.; Barnett, B.; Xu, K. Before Li Ion Batteries. Chem Rev 2018, 118 (23), 11433-11456.

Wrogemann, J. M.; Haneke, L.; Ramireddy, T.; Frerichs, J. E.; Sultana, I.; Chen, Y. I.; Brink, F.; Hansen, M. R.; Winter, M.; Glushenkov, A. M.; et al. Advanced Dual-Ion Batteries with High-

Capacity Negative Electrodes Incorporating Black Phosphorus. Adv Sci (Weinh) 2022, 9 (20), e2201116.

Xie, J.; Lu, Y. C. A Retrospective on Lithium-Ion Batteries. Nat Commun 2020, 11 (1), 2499.

Xie, L. S.; Skorupskii, G.; Dincă, M. Electrically Conductive Metal–Organic Frameworks. Chem. Rev. 2020, 120 (16), 8536-8580

Xu, K. Nonaqueous Liquid Electrolytes for Lithium-Based Rechargeable Batteries. Chemical Reviews 2004, 104 (10), 4303-4418.

Xu, W.; Welty, C.; Peterson, M. R.; Read, J. A.; Stadie, N. P. Exploring the Limits of the Rapid-Charging Performance of Graphite as the Anode in Lithium-Ion Batteries. Journal of The Electrochemical Society 2022, 169 (1)

Yazami, P. T. a. R. Lithium-Graphitic Oxide Cells. Journal of Power Sources 1985, 14, 99-104.

Yoshino, A. The Birth of the Lithium-Ion Battery. Angew Chem Int Ed Engl 2012, 51 (24), 5798-5800.

Zhang, H.; Li, Z.; Xu, W.; Chen, Y.; Ji, X.; Lerner, M. M. Pillared Graphite Anodes for Reversible Sodiation. Nanotechnology 2018, 29 (32), 325402.

Zhang, H.; Liu, X.; Wu, Y.; Guan, C.; Cheetham, A. K.; Wang, J. MOF-Derived Nanohybrids for Electrocatalysis and Energy Storage: Current Status and Perspectives. Chem. Commun. 2018, 54 (42), 5268-528

Zhixin Ma, T. K., Akira Tomita. Synthesis Methods for Preparing Microporous Carbons with a Structural Regularity of Zeolite Y. Carbon 2002, 40 (13), 2367-2374

Zhou, X.; Liu, Q.; Jiang, C.; Ji, B.; Ji, X.; Tang, Y.; Cheng, H. M. Strategies Towards Low-Cost Dual-Ion Batteries with High Performance. Angew Chem Int Ed Engl 2020, 59 (10), 3802-3832.

APPENDIX

SOLID ELECTROLYTE INTERPHASE ON ZTC

The redox energy of Li/Li^+ lies outside of the stability window of all known non-aqueous electrolytes. When the electrochemical potential of the anode is outside of the lowest unoccupied molecular orbital (LUMO) of the electrolyte, then decomposition on the surface occurs. This decomposition is called the SEI and is a passivating layer passivates that protects the anode from further electrolyte decomposition. During the first charging cycle of a LIB around 20% of the capacity can be associated with decomposition of electrolyte components forming the SEI. This layer allows the battery to cycle reversibly, without it the electrolyte would decompose until there were no active ions left. However, the SEI layer slows diffusion of Li^+ to the redox sites at the anode which results in poor rate capability and dendritic formation. The SEI comprises both crystalline and amorphous components, for that reason it requires multiple characterization techniques to identify all of its constituents. Determining how each type of molecule interacts with another is increasingly challenging and, in the end, XPS is a necessary technique. It is crucial to optimize the SEI to allow for fast ionic diffusion, but this is a nontrivial task given how difficult the layer is to characterize.

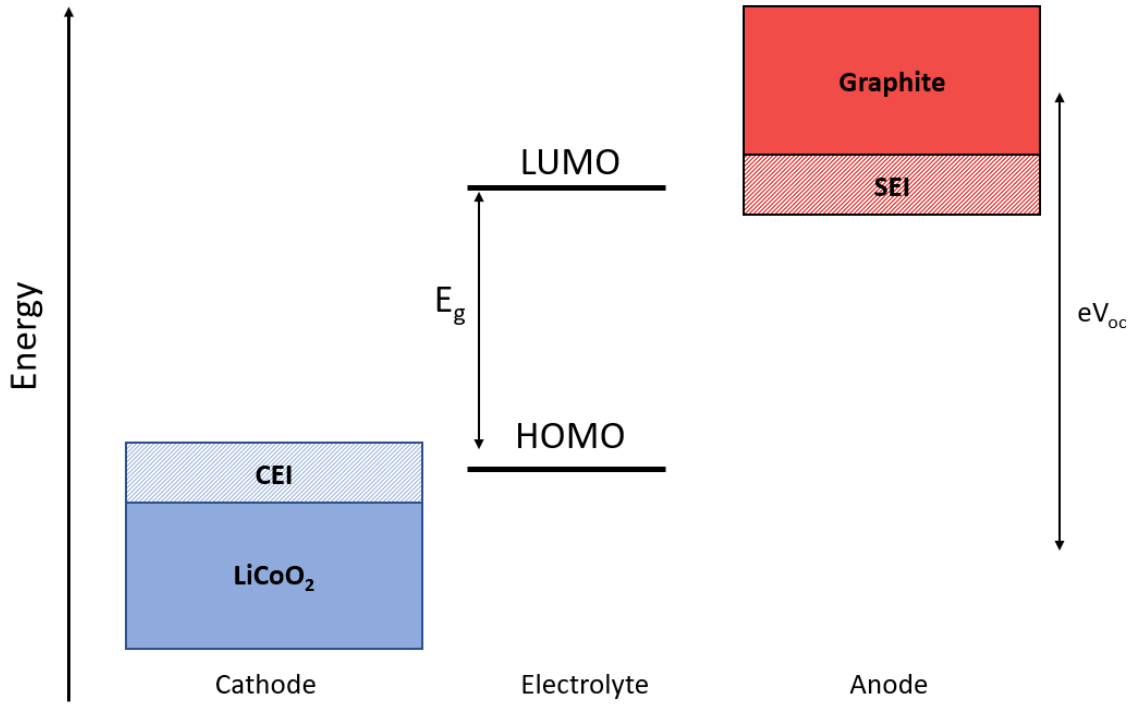

Figure 1. Schematic energy levels of an anode, cathode, and electrolyte in an open circuit. Relative energies of the electrolyte window E_g, and the open circuit voltage $eV_{oc.}$

The amount of SEI formed on graphite particles during electrochemical cycling is quite small. The SEI is typically only 10 to 20 nm thick even after extensive cycling. Hence, there isn't much material to analyze unless multiple cells are harvested, which introduces extraneous variables. ZTC forms a massive amount of SEI because if its large surface area (~3300 m^2 g^{-1}) relative to the amount of active material. The high concentration of SEI provides intense and distinguishable peaks when analyzed via XRD and FTIR. The SEI is thought to contain Li-conducting oligomers or polymers and organometallics. In reality, there are several combinations of Li and carbonates that can conduct ions through the layer and it is nearly impossible to deconvolute all of them XRD can be used to determine the presence of LiF due to its crystalline nature. FTIR can be used to determine the presence of LiOH, $LiCH_3CO_3$, $Li_2(CH_2COCO_2)_2$ and

Li_2CO_3. In this study we examine the effect that solvent composition has on the SEI layer formed with ZTC compared to graphite. 4 different solvents were explored, DMC, PC, EC/DMC 4:1, and EC/DMC 1:1. The salt remained the same throughout this experiment, 1M and 4M LiPF6 and all of the characterization was taken in the delithiated state.

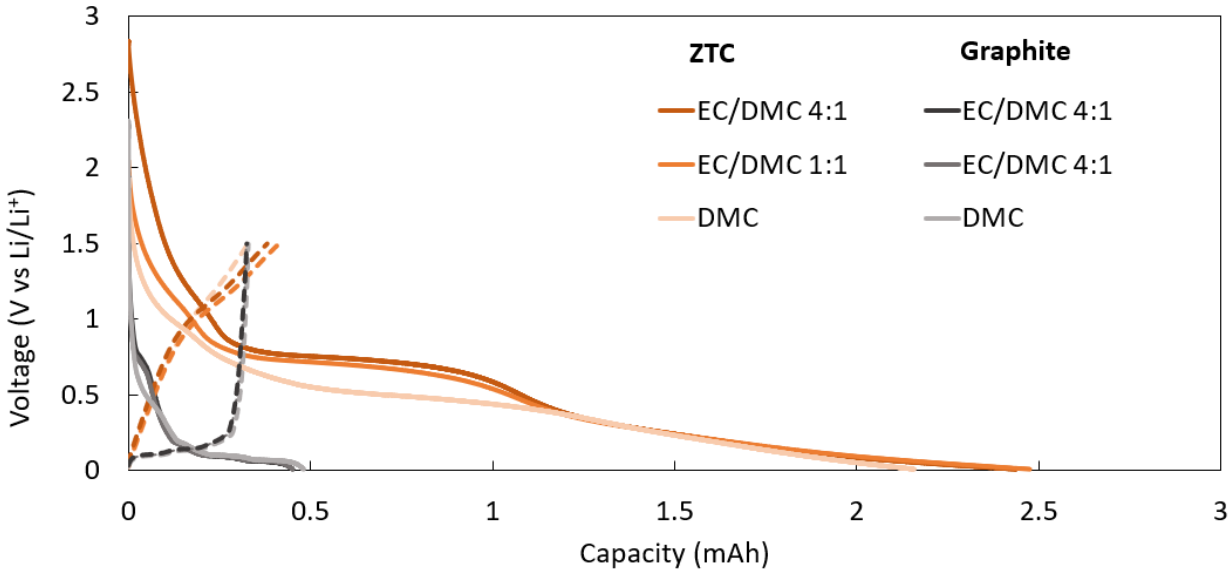

Figure 2. First cycle voltage profiles of ZTC and graphite in 3 different solvents. 4M $LiPF_6$ in DMC, EC/DMC 1:1, EC/DMC 4:1.

ZTC decomposes five times the amount of electrolyte as graphite does. By multiplying the coulombic efficiency by the first cycle lithiation capacity we can determine the amount of capacity attributed to SEI formation. Figure 2 shows that 2.1 mAh of capacity forms the SEI in ZTC whereas graphite requires 0.32 mAh. The voltage profiles of graphite are consistent across all 3 solvent systems. EC containing solvents show a higher decomposition plateau than pure DMC in ZTC which suggests that EC decomposes more readily. The coulombic efficiencies of pure DMC were lower than 4:1 and 1:1 EC/DMC. The difference in ratio of EC/DMC does not seem to make a difference in the first cycle voltage profile. Figure 3 shows a representative ZTC

anode after 1000 cycles in 4M $LiPF_6$ in DMC. Slight delamination from the current collector is observed and was present in all solvent systems.

	DMC	EC/DMC 1:1	EC/DMC 4:1
ZTC ICE (%)	13	15	16
Graphite ICE (%)	67	74	72

Table 1. Initial coulombic efficiencies (ICE) of ZTC and graphite. 4M $LiPF_6$ in DMC, EC/DMC 1:1, EC/DMC 4:1.

Figure 3. Opened coin cell with ZTC anode after extended cycling and SEI formation.

The full scan XRD pattern showed many different combinations of Li and carbonates (Figure 4). The hypothesis that ZTC would show more intense peaks than graphite is shown to hold true. The only identifiable peaks in graphite via XRD were LiOH and LiF. The 002 peak at 26.3° 2θ can be attributed to the ABAB stacking of the graphene layers. DMC and EC/DMC both showed 5 peaks associated with lithium carbonates between 28 and 36° 2θ. PC showed a relatively clean spectra with LiOH responsible for all of its peaks. This could be attributed to the high dielectric constant of PC, staying tightly bound to the Li^+ ions upon charging. Given that

EC has a very high dielectric constant and similar structure to PC, it is possible that DMC was responsible for the majority of the carbonates formed in the EC/DMC mixture (that were detectable by XRD).

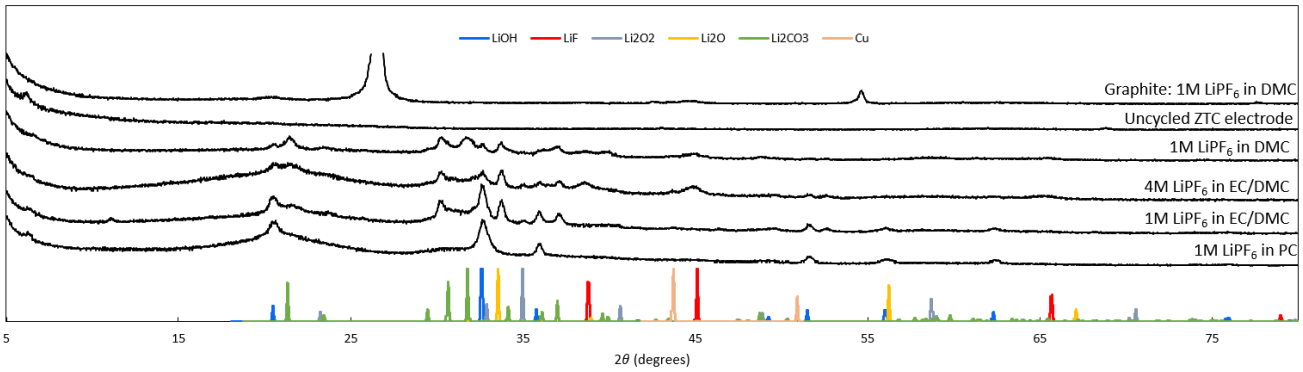

Figure 4. XRD patterns of ZTC and graphite electrodes in 3 different solvents after being cycled 5 times at 100 mA g^{-1} between 0.05–1.5 V vs. Li/Li^+ as well as simulated PXRD patterns of expected SEI components.

FTIR was used to compare the identities of the different electrolyte and not to quantify relative amounts (Figure 5). The main conclusion was that 4:1 EC/DMC lacked intense peaks for Li_2CO_3 where every other solvent showed intensity. Li_2CO_3 was the major contribution to SEI on graphite, in addition to a very low intensity peak present for LiOH at 3450 cm^{-1}. ZTC in DMC also showed more pronounced peaks for Li_2CO_3 and LiOH than other solvents which corroborates the low coulombic efficiency.

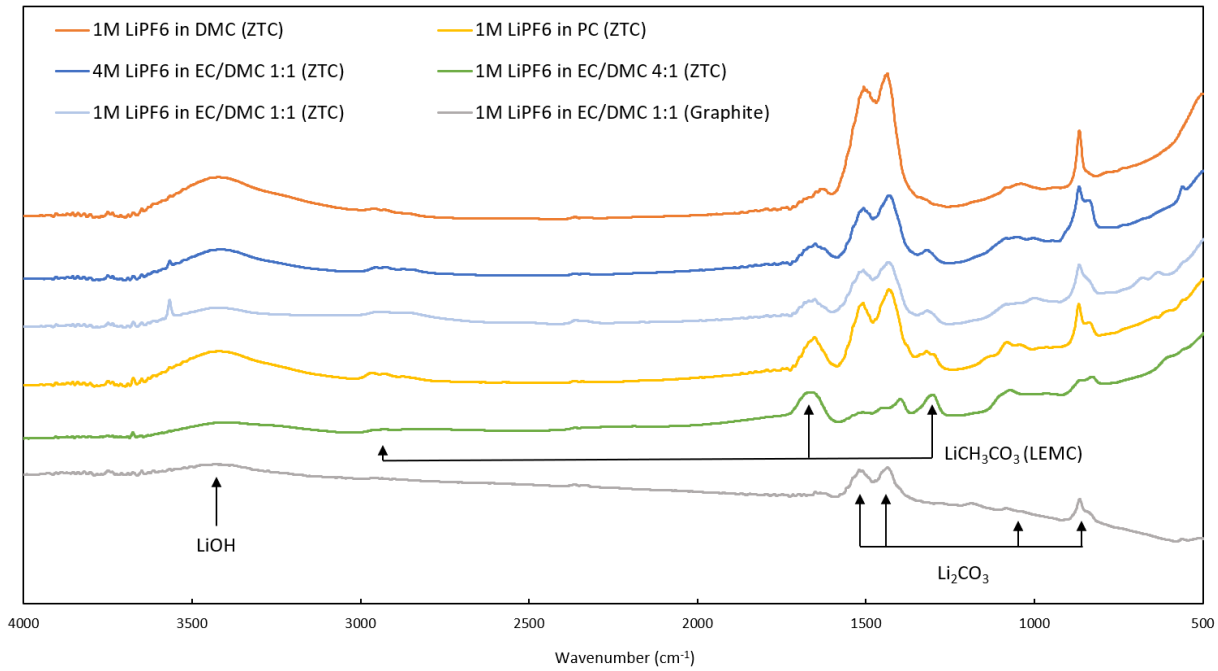

Figure 5. FTIR spectra of ZTC and graphite electrodes in 3 different solvents after being cycled 5 times at 100 mA g^{-1} between 0.05–1.5 V vs. Li/Li^+. KBr was used to subtract the background.

An XRD study of just 4M $LiPF_6$ in DMC, EC/DMC (1:1), and PC on ZTC and graphite was designed to explore the LiF content. Figure 6 showed that as the dielectric constant of the solvent increased, LiF intensity in the SEI decreased and the lithium carbonate intensity increased. Scherrer analysis needs to be done to determine the crystallite size in each solvent. An inverse relationship can be observed between LiOH and LiF. From DMC to EC/DMC to PC the LiOH peak became more intense while the LiF peak diminished. This is evidence that solvent plays an important role on the crystallization of SEI components.

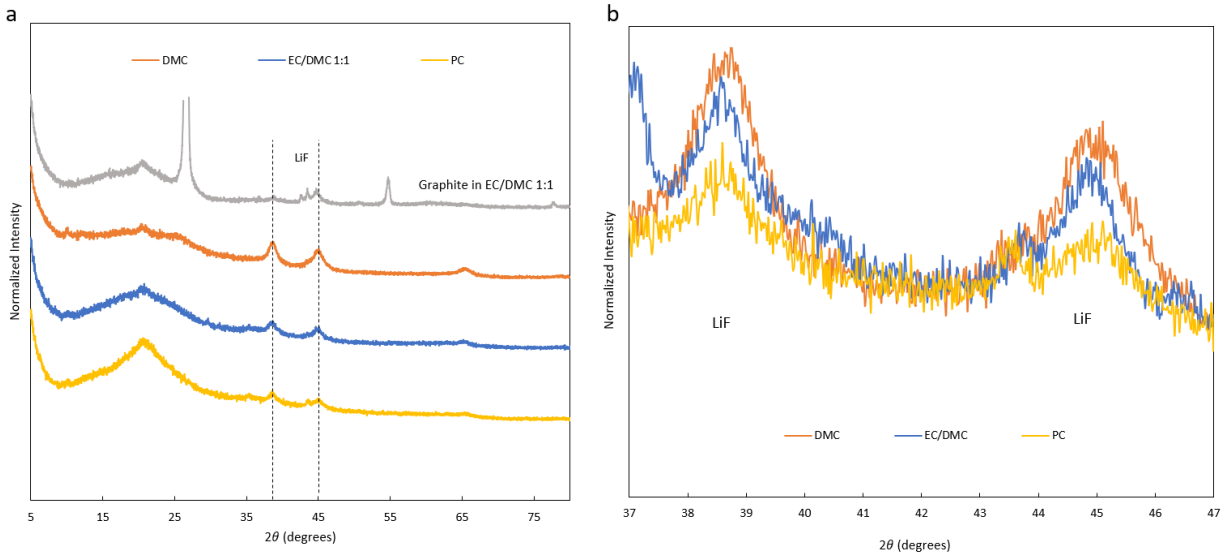

Figure 6. XRD patterns of ZTC and graphite electrodes with 4M $LiPF_6$ in 3 different solvents after being cycled 5 times at 100 mA g^{-1} between 0.05–1.5 V vs. Li/Li^+

Future research in this area should focus on refreshing the electrolyte in a cell after the SEI has formed. Refreshing with the same electrolyte as a control and with highly diffusive solvent would produce interesting results. Lithium polyacrylic acid (LiPAA) is known to induce a stretchable, dynamic SEI. After 5 cycles, or until the coulombic efficiency reaches 95%, LiPAA could be replaced with a low viscosity solvent such as DMC that would enhance the rate capability of the cell. Figures 4 and 5 show that DMC decomposes the most out of all of the solvents tested and consequently is not suitable for SEI formation. Ideally, a thin SEI layer should be formed that protects the surface from further decomposition but allows for fast ion diffusion.